Processing of shipborne magnetometer data and revision of the timing and geometry of the Mesozoic break-up of Gondwana

Auswertung schiffsfester Magnetometerdaten und die Neubestimmung des Zeitpunktes und der Geometrie des Mesozoischen Aufbruchs von Gondwana

---

Matthias König

Matthias König

Alfred Wegener Institute
Institute for Polar and Marine Research
Postfach 12 01 61
27515 Bremerhaven, Germany
http://www.awi-bremerhaven.de
mkoenig@awi-bremerhaven.de

Die vorliegende Arbeit ist die inhaltlich unveränderte Fassung einer Dissertation, die 2005 dem Fachbereich Geowissenschaften der Universität Bremen vorgelegt wurde. Sie ist in elektronischer Form erhältlich unter http://www.awi-bremerhaven.de/Library
.

Contents

Zusammenfassung

Magnetische Meeresbodenanomalien wie sie bei dem Auseinanderdriften von Lithosphärenplatten an mittelozeanischen Rücken entstehen, beherbergen wichtige Informationen über die paleogeographische Konfiguration der Kontinente und die Entwicklung der Ozeanbecken. Zur Vermessung dieser magnetischen Anomalien werden normalerweise Magnetometersysteme verwendet die von Schiffen geschleppt, oder fest auf Flugzeugen montiert sind. Für die Polarregionen sind jedoch Schiffssysteme, die fest mit dem Schiff verbunden sind gegenüber geschleppten Systemen zu bevorzugen.

Im ersten Teil dieser Arbeit wird das schiffsfeste Magnetometersystem auf FS *Polarstern* vorgestellt und eine Methode zur Auswertung dieser Daten entwickelt. Im zweiten Teil wird, basierend auf einer Kompilation magnetischer Meeresbodenanomalien, ein geodynamisches Modell für die Öffnung des Weddell Meeres und den mesozoischen Aufbruch von Gondwana abgeleitet.

Magnetfeldmessungen, wie sie an Bord des deutschen Eisbrechers und Forschungsschiffes *Polarstern* durchgeführt werden, werden durch die magnetischen Eigenschaften des Schiffsrumpfes und der Aufbauten stark gestört. Zur Korrektur dieser Störfelder werden Kompensationskoeffizienten berechnet und auf die Rohdaten angewendet. Mit der in dieser Arbeit vorgestellten Methode zur Kompensation und Filterung der Magnetometerdaten kann bei ruhiger See eine Genauigkeit von 20 nT bei einer horizontalen Auflösung von 154 m erreicht werden. Dies ermöglicht die Auswertung und geowissenschaftliche Interpretation einzelner Profillinien sowie die Bearbeitung flächig vermessener Datensätze bishin zur Kompilation magnetischer Anomaliekarten. Der Vergleich mit anderen hochauflösenden Magnetikdatensätzen unterstreicht die Anwendbarkeit der schiffsfesten Magnetometerdaten zur Bearbeitung geowissenschaftlicher Fragestellungen und verdeutlicht die Möglichkeiten des Systems.

Im zweiten Teil dieser Arbeit wird ein verfeinertes Modell für die Öffnung des Weddell Meeres und den Aufbruch von Gondwana vorgestellt. Aus der Interpretation eines neuen hochauflösenden Magnetikdatensatzes im östlichen Weddell Meer und den daraus abgeleiteten, gut gesicherten Datierungen und Orientierungen der Meeresbodenanomalien wurde ein detailliertes Modell für die Öffnung des Weddell

Meeres bestimmt. Aus der Kombination mit Daten für die Spreizungssysteme zwischen Südamerika - Afrika und Afrika - Antarktis wurde daraus ein neues Modell für den Aufbruch von Gondwana für den Zeitraum zwischen 167 Ma und 83 Ma berechnet.
In diesem Modell kommt es zwischen 167 Ma und 147 Ma zu Extensionsbewegungen im Filchner-Ronne Schelf und dem Falkland Plateau wärend sich zeitgleich Afrika und die Antarktis im Somali- und Mosambikbecken in Nord-Südrichtung voneinander trennen. Im Gegensatz zu Modellen, die eine Öffnung lediglich zwischen Ost- und West-Gondwana diskutieren, entstehen in diesem Modell drei separate Becken, das Somali- und Mosambikbecken und das Weddell Meer, bereits wärend der frühen Phase des Gondwanaaufbruchs. In dem hier vorgestellten Modell beginnt die Trennung zwischen Südamerika und der Antarktis im südlichen Weddell Meer erst bei etwa 147 Ma, das ist 10 bis 20 Millionen Jahre später als bisher angenommen. Die nachfolgende Öffnung erfolgt bei langsamer (∼12-14 mm/a Halbrate), und nach der magnetischen Chron M2 (122.3 Ma) ultra-langsamer (∼8 mm/a) Spreizungsrate. Die NNW gerichtete Spreizungsrichtung ändert sich dabei nur wenig. Weitere Konsequenzen dieses Modells sind die Neudatierung der Entstehung der seewärts gerichteten Reflektorsequenzen entlang der Küste des westlichen Dronning Maud Landes sowie neue Anhaltspunkte zu der möglichen Driftbewegungen des Mosambikrückens zwischen Afrika und der Antarktis und der Entstehung einer Tiefenwasserverbindung zwischen dem indischen und atlantischen Ozean.

Abstract

Seafloor spreading anomalies in the world's ocean basins yield crucial information about the paleogeographic configuration of the continents and the development of ocean basins. Standard methods for measuring these variations are to apply ship towed magnetometer systems or aircrafts. For the polar regions, magnetometer systems fixed to a vessel are more appropriate. A processing sequence for the evaluation of magnetometer data acquired onboard RV *Polarstern* with a sensor system fixed to the ship is described in the first part of this thesis. In the second part, seafloor spreading anomaly data, measured by ship, aircraft and helicopter, in the South Atlantic region, are used to constrain a geodynamic model for the Mesozoic break-up of Gondwana and the development of the Weddell Sea Basin.

Magnetometer data acquired onboard the German ice breaker and research vessel *Polarstern* have to be corrected for the ship's interfering field caused by the hull and other steel parts of the ship. This correction is done by the calculation of appropriate compensation coefficients. With the processing scheme presented in this thesis the ship's magnetometer data are compensated and filtered to an accuracy of about 20 nT at a horizontal resolution of about 154 m in quiet sea conditions. This makes the data suitable for a consistent interpretation of single track data or further processing of a network of profiles. The compilation of a magnetic anomaly map and comparison with other high resolution magnetic anomaly data demonstrate the suitability of the processed data to be used for detailed interpretations of magnetic anomalies in geodynamic problems like those encountered in the South Atlantic region and dealt with in the second part of this thesis.

A refined model for the break-up of Gondwana and the opening of the Weddell Sea is presented in the second part of this thesis. From an interpretation of a newly acquired extensive magnetic anomaly data set in the eastern Weddell Sea, well constrained ages and orientations of seafloor spreading anomalies are used to calculate a new set of model parameters for the opening of the Weddell Sea. These are combined with constraints on the South America - Africa and Africa - Antarctica spreading systems, based on a compilation of magnetic anomaly and fracture zone data, to determine a new model for Gondwana break-up between 167 Ma and 83 Ma. At the same time when north-south oriented separation between Africa and Antarc-

tica is initiated by rifting in the Somali and Mozambique basins, stretching and extension takes place in the Filchner-Ronne Shelf and the Falkland Plateau between 167 Ma and 147 Ma. In contrast to models proposing only rigid East-West Gondwana separation, this model features three separate basins developing simultaneously during early Gondwana break-up. These basins are the Somali, Mozambique, and Weddell Sea basins. In the new model, separation between South America and Antarctica starts in the southern Weddell Sea at around 147 Ma, about 15 to 20 million years later than previously estimated. Subsequent spreading occurs at slow (∼12-14 mm/yr halfrate), and after magnetic chron M2 (122.3 Ma) ultra-slow (∼8 mm/yr) spreading rates, with little change in the NNW spreading direction. Further consequences of this model are a revision of the age of formation of seaward dipping reflector sequences along the continental margin off western Dronning Maud Land and new constraints on possible movements of the Mozambique Ridge between Africa and Antarctica during the break-up of Gondwana and the development of a deep water connection between the Indian and the South Atlantic Ocean.

1 Introduction

The geomagnetic field as we know it today can be approximated as a dipole that is displaced several hundred kilometers from the center of the earth and inclined some 11.5° to the earth's rotational axis. The present theory about the origin of the dipole field is that it is caused by convection currents of conducting material circulating in the liquid outer core and driven by the rotation of the earth. This part of the geomagnetic field is called the main field and is overprinted by the external magnetic field, which appears to be associated with electric currents in the ionized layers of the upper atmosphere. This external part makes only about 1% of the geomagnetic field.
The present orientation of the geomagnetic field is not the same as it was about 140 million years ago. The geomagnetic field has reversed its direction frequently throughout the last 200 million years. The chronology of these reversals is stored in a sequence of normal (parallel to today's geomagnetic field) and reversed magnetized portions of the ocean floor, like the record on a magnetic tape. The formation of parallel bands of alternating magnetic polarity on the seafloor is bound to its continual creation at mid-ocean ridges (MOR). Young and hot material from the mantle ascends to the ocean floor in the presence of the local geomagnetic field. While cooling below a specific temperature (the Curie temperature), the ferromagnetic domains within the igneous rocks of the seafloor align themselves with the geomagnetic field. Thus, the direction of the geomagnetic field at the time of cooling is preserved as part of the thermoremanent magnetization of oceanic crustal rocks.
If the magnetic field is measured along a profile perpendicular to the strike of an old MOR, a sequence of positive and negative anomalies can be recorded. These are called seafloor spreading anomalies. The age of the ancient ocean floor can be calculated through the correlation of these anomalies with paleomagnetic time scales. It is this age information that is a crucial key to the paleogeographic reconstruction of continents and ocean basins.

This thesis deals with the evaluation of magnetic anomaly data measured onboard an uncompensated ship and the interpretation of seafloor spreading anomalies to solve geodynamic problems in the South Atlantic region.

The main objectives are the development of a processing procedure to evaluate measured magnetic field data recorded onboard the German research ice breaker RV *Polarstern*, and to determine a detailed model for the Mesozoic break-up of Gondwana in general, and the Weddell Sea in particular, from the interpretation of magnetic anomaly data.

A highly magnetized body, like a ship made of several hundred tons of steel, is not usually employed as a platform for conducting magnetic measurements. But there are several reasons why a system fixed to a ship may be more practical than a magnetometer system that is towed astern of a ship at a distance of several hundred meters.
A ship-mounted magnetometer can be operated permanently, even under ice breaking conditions or heavy storms, at any time of the day with a minimum of technical maintenance. Such capabilities may not be of importance for dedicated surveys in open water, but are of great importance for ships like RV *Polarstern*. This vessel operates most of its time in the remote seas of the Arctic and off the coast of Antarctica. Data coverage is generally very sparse in these regions and any additional magnetic track data gathered on transit or in areas of special interest are a valuable source of information, especially for the indentification of seafloor spreading anomalies. However, there are limits on the accuracy of ship-mounted magnetic sensor systems. Due to intense interfering fields generated by the hull and other steel parts of the ship, the accuracies achieved with such a sensor system will not reach those of present day ship-towed magnetometer systems, which can be well below 1 nT. Nonetheless, as will be shown here, shipboard magnetometer data can be corrected for the ship's interfering field using a simplified model for the magnetic field generated by the ship. Furthermore, compensated magnetic anomaly data can be used to record complete sequences of seafloor spreading anomalies and to compile regional magnetic anomaly maps from networks of processed track line data.

The determination of a detailed model for the early break-up of Gondwana in the South Atlantic region is the main objective of the second part of this thesis. There is still great uncertainty about the exact timing and geometry of the early opening of the Weddell Sea. Consequently, models describing the early break-up of Gondwana, involving the continents South America, Africa and Antarctica, are characterized by many open questions on the early movements in the southwestern corner of Gondwana (South America, Antarctic Peninsula, East Antarctica).
In this thesis, based on an interpretation of an extensive high-resolution magnetic anomaly data set, knowledge of the ages of the oldest ocean floor in the southern Weddell Sea can be revised to an earlier date, and a refined model for the early open-

ing between South America and Antarctica can be established. The unequivocally dated magnetic anomaly identifications from this spreading system are combined with a great amount of additional magnetic anomaly and fracture zone data from ocean basins along the coasts of South America and Africa in order to determine a refined and well constrained model for the Mesozoic break-up of Gondwana. In this model, movements between southernmost South America, the Antarctic Peninsula, and East Antarctica are described as being active in the Weddell Sea before any seafloor spreading started. Rifting between southernmost South America and the Antarctic Peninsula resulted in the formation of the eastern continental margin of the Antarctic Peninsula. At the same time, extensive stretching of continental crust occured in the Filchner-Ronne Shelf. The opening of the Weddell Sea was initiated by the extrusion of large volumes of basaltic material forming seaward dipping reflector sequences along the coast of western Dronning Maud Land. Based on the new age constraints for the age of the oldest ocean floor in the Weddell Sea, a significantly younger age for the formation of the seaward dipping reflector sequences than previously published by other authors is proposed. The new Gondwana break-up model presented in this thesis also has significant implications on possible positions and movements of the Mozambique Ridge between Africa and Antarctica, acting as a barrier between the Indian and the South Atlanctic Ocean until about mid-Cretaceous times. A discussion on possible configurations and remaining questions will be given at the end of the second part of the thesis.

2 The ship-mounted magnetometer system onboard RV *Polarstern*

Ship-towed magnetometer systems are commonly used in marine geophysics for recording seafloor spreading anomalies over the ocean floor. These systems are normally equipped with one or more total field magnetometers towed at some distance (300 - 400 m) astern a ship. During expeditions into polar regions, however any instrument deployed outboard the ship runs the risk of being lost, or damaged while passing through ice fields. Under these extreme conditions, a ship-mounted system would be more appropriate. Additionally, by the use of such systems, continuous measurements are possible, even during transit, without additional maintenance.

In the case of the German icebreaker and research vessel *Polarstern*, a ship-mounted magnetometer system can significantly contribute to the scientific outcome of marine geophysical expeditions to the polar regions, carried out once a year in the Arctic Ocean and once in the seas off Antarctica. While continuous recordings are made along track in the areas of special interest, data recorded along the transit between survey areas can be a valuable source of additional information. A further example of use of the ship-mounted magnetometer system is the support of helicopter-borne surveys. Helicopters are regularly deployed from RV *Polarstern* for detailed aeromagnetic surveying. Unfortunately, due to bad weather conditions (fog, mist, strong winds), crucial lines often cannot be flown, leaving considerable gaps in the planned flight pattern of a survey area. Using a data acquisition system that is independent of weather conditions, it is possible to close such gaps or add profiles to already existing flight lines. Furthermore, a ship-mounted magnetometer system can serve as a magnetic base station in combination with helicopter-borne surveys. If the ship remains relatively stationary, or is only slowly moving while helicopter flights are performed, the two synchronous recorded data sets can be correlated with each other and daily variations can be detected and eliminated. In this way, the data quality of helicopter-borne surveys can be significantly improved since the inaccuracies due to strong daily variations, especially in polar regions, are often higher than the expected signal.

A three-component fluxgate magnetometer system was installed onboard RV *Polarstern* in 2000 (Kopsch et al., 2000). After initial tests, this system is fully operational since the ANT-XIX/2 expedition in the Weddell Sea, Antarctica (December 2001 - January 2002) (Kopsch and Kroth, 2003). Since then, it has been in use mainly during expeditions to the Arctic in the years 2002 - 2004.

In this thesis a processing procedure for the evaluation of shipborne magnetometer data has been set up and implemented into a newly developed MATLAB (The MathWorks, Inc.) software package which can be used for a complete processing of the raw magnetometer data including, amongst others, the calculation of compensation coefficients, application of the coefficients, data filtering, performing an IGRF correction and daily correction, and calculating power spectra, cross-correlations and coherencies. Estimates on the accuracy achieved with this sensor system and processing scheme are made using data acquired during the ARK-XVIII/2 expedition to northeast Greenland and Svalbard (August - October 2002).

The structure and content of the following chapters can be briefly summarized as follows: Some important studies and developments in the branch of shipborne magnetics using onboard magnetometer systems are introduced in chapter 2.1. A description of the theory of ship magnetism is provided in chapter 2.2. This is followed in chapter 2.3 by a description of the magnetometer and the data acquisition system. Details of the data processing procedure will be given in chapter 2.4. An estimate of the accuracy of the processed data will be provided in chapter 2.5, through the comparison with helicopter-borne data. Finally, in chapter 2.6, a case study for a small scale survey area will demonstrate the ability of the new magnetometer system to be used to compile magnetic anomaly maps from systematic profiling. A comparison with a helicopter-borne data grid and a grid based on a regional magnetic anomaly compilation is made. After summarizing the results, improvements to the magnetometer system are discussed at the end of chapter 2.7.

2.1 Geomagnetic measurements onboard uncompensated ships

Magnetic measurements of the horizontal component of the earth's magnetic field in polar regions were conducted by Bidlingmaier as early as 1901 - 1903 during the first German south polar expedition (Bidlingmaier, 1925). Measurements in the Arctic ocean near Svalbard, using the same double compass system as constructed by Bidlingmaier, were made by Lengning in 1958 onboard the German vessel MS *Meteor* (Lengning, 1961). During further expeditions to the Red Sea and Svalbard, Förster Sondes were developed by Auster and Lengning (1963) and Auster (1964)

to additionally record the three components of the local geomagnetic field onboard an uncompensated ship. These studies were basic investigations on the possibility of carrying out geomagnetic measurements from an uncompensated ship.

Since 1977 Japanese scientists have been developing a *Shipboard Three Component Magnetometer* system, called STCM (Isezaki et al., 1981). The first applications of this system for geomagnetic measurements were presented by Isezaki et al. (1981) and Isezaki (1986). In the following years, further studies on the evaluation and interpretation of marine magnetic vector anomalies measured with the STCM were published (Seama and Isezaki, 1990; Nogi et al., 1990a; Nogi et al., 1990b; Seama et al., 1993; Korenaga, 1995; Nogi et al., 1996; Nogi and Kaminuma, 1999a; Nogi and Kaminuma, 1999b; Nogi and Seama, 2002). The error of the STCM system, as presented by Isezaki (1986) is given as 50 $\pm$25 nT. Horizontal resolution of the STCM data strongly depends on the filters applied and the velocity of the ship. Generally, it is given to be in the order of 3-5 km using a 15-21 min moving average filter (Seama and Isezaki, 1990; Nogi et al., 1990a).

Magnetic measurements onboard uncompensated ships were also studied by Peters (2000). The aim of this study was to develop a magnetic system fixed to the ship and capable of recording magnetic anomaly signals produced by shipwrecks in shallow water conditions (<100 m). The expected amplitudes of such anomalies vary between 50 nT and 100 nT. Thus, a system with an accuracy better than 50 nT was needed. Two proton precession magnetometers were used for data acquisition. Unlike the measurements carried out by the Japanese, the detection of low amplitude short wavelength anomalies prohibits the use of rigorous long wavelength filters. Peters (2000) finally concludes that only magnetic anomalies with an amplitude of more than 50 nT can be detected unequivocally. Thus, magnetic measurements carried out from an uncompensated ship using total magnetic field magnetometers yield not the desired accuracy needed for detecting wrecks or other small anomalous bodies under shallow water conditions.

The magnetometer system installed onboard RV *Polarstern* is primarily not intended to be used for wreck detection or other small-scale surveys with desired accuracies of 10 nT or less, but it should be able to record low amplitude (<50 nT) seafloor spreading anomalies with wavelengths of several hundred meters.

2.2 Theoretical background

2.2.1 Reference systems

Before a model for the magnetic field measured onboard uncompensated ships will be introduced, the reference systems used throughout this work and the corresponding transformations should be explained.

There are two independent coordinate systems which are of interest. The more common one is the geodetic coordinate system, which is fixed to the surface of the earth (see figure 2.2-1 for details). The axes of this coordinate system are defined using the following conventions (Table 2.2-T1):

Table 2.2-T1: Geodetic coordinate system.

X_e	positive to the north,
Y_e	positive to the east and
Z_e	positive down towards the center of the earth.

The vector of the earth's magnetic field, $\vec{B}_e^E$, with its components X_e^E, Y_e^E, and Z_e^E is defined in the geodetic coordinate system as shown in figure 2.2-1.

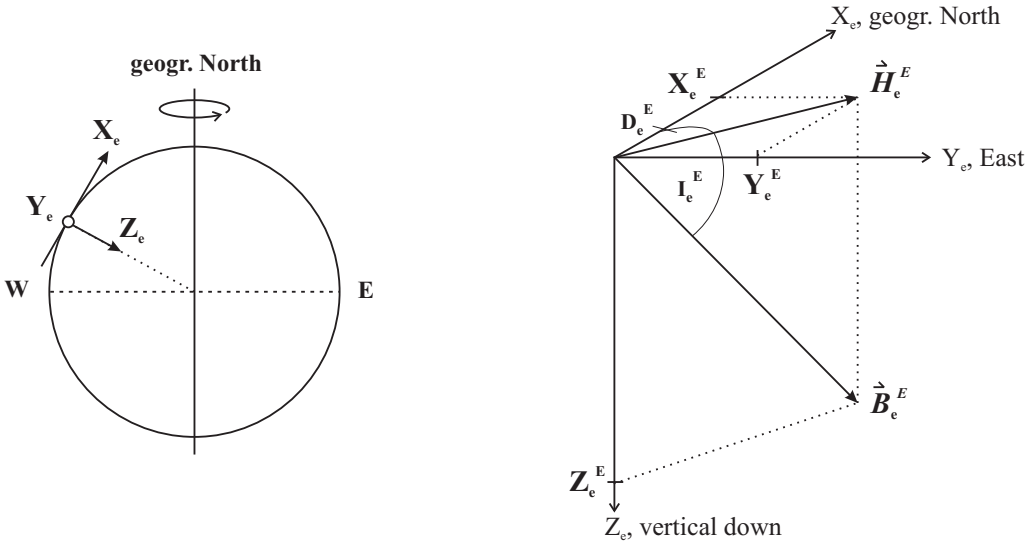

Figure 2.2-1: The vector of the earth's magnetic field $\vec{B}_e^E$ as defined in the geodetic coordinate system, fixed to the surface of the earth. X^E, Y^E, and Z^E are the axes of the geodetic coordinate system. X_e^E, Y_e^E, and Z_e^E are the components of the earth's magnetic field vector and D_e^E, and I_e^E are the declination and inclination angle, respectively. $\vec{H}_e^E$ is the horizontal magnetic field.

The coordinate system used to describe the vector of the magnetic field measured

onboard the ship is defined as shown in table 2.2-T2 and figure 2.2-2.

Table 2.2-T2: Ship's inertial coordinate system.

X_s	positive to bow, alongside component
Y_s	positive to starboard, cross component
Z_s	positive down to the keel, vertical component.

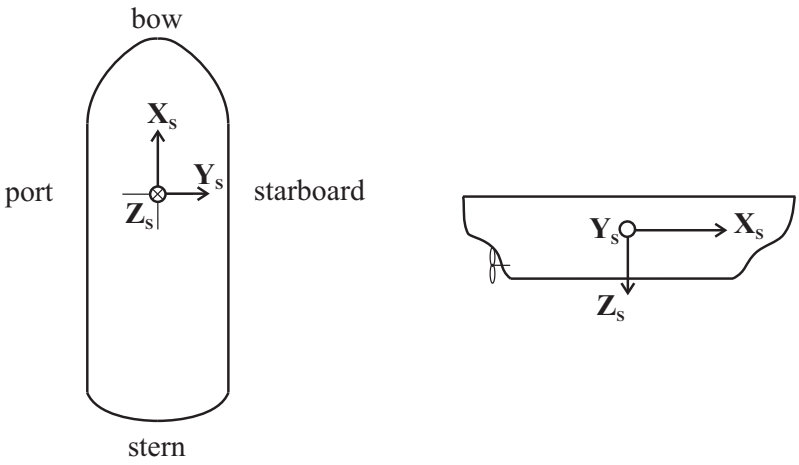

Figure 2.2-2: Local coordinate system onboard the ship.

Note that both coordinate systems are right handed, orthogonal coordinate systems with the vertical axis oriented positive down (Figs. 2.2-1 and 2.2-2). The axes of the magnetic field sensors are aligned with the local ship's inertial coordinate system.

Transformations from one coordinate system to the other can be described by successive rotations about the principal axes of the ship's coordinate system. The angles used for these rotations are the ship's attitude angles and are defined in the following table 2.2-T3 and figure 2.2-3.

Table 2.2-T3: Attitude angles in the ship's coordinate system.

α (heading)	rotation about the vertical axis (Z_s), positive to east,
β (roll)	rotation about the longitudinal axis (X_s), positive starboard down,
γ (pitch)	rotation about the cross axis (Y_s), positive bow up.

The rotations are applied in a specific order for the transformation from the geodetic coordinate system to the ship's reference system.
First, a rotation about the vertical axis of the geodetic coordinate system using the

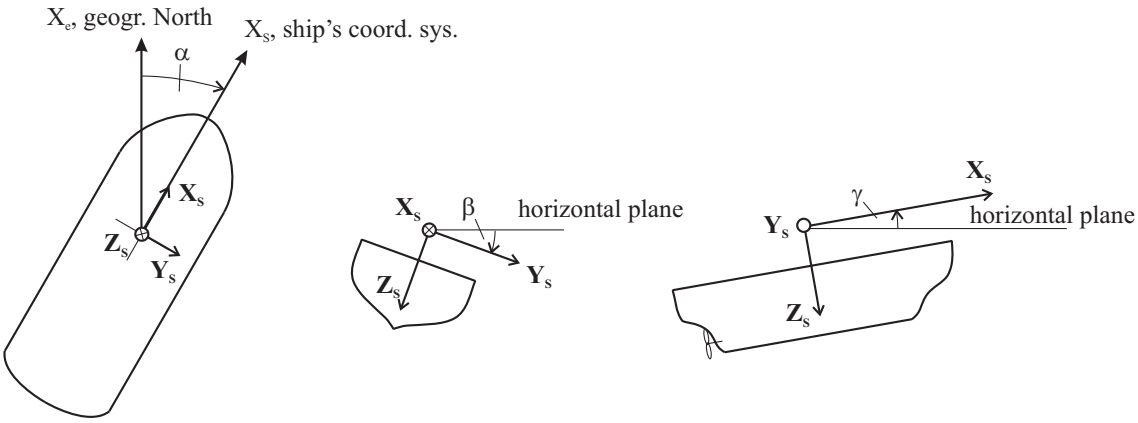

Figure 2.2-3: Definition of the ship's attitude angles.

course angle α is performed, then a rotation by an angle δ (see below) and about the new X-axis follows, and finally a rotation by the pitch angle, γ, about the Y-axis in the ship's coordinate system is applied.

The angle δ depends on β (roll) and γ (pitch) according to the following relationship:

$$\tan(\beta) = \frac{\tan(\delta)}{\cos(\gamma)} \tag{1}$$

For small angles of γ, δ can be approximated by β. Since γ normally does not exceed 3°, the measured angle of β will be used instead of δ from now on.

Combining all these rotations, which are not commutative, the final rotation matrix has the form:

$$\underline{D} = \begin{pmatrix} \cos\alpha\cos\gamma - \sin\alpha\sin\gamma\sin\beta & \sin\alpha\cos\gamma + \cos\alpha\sin\gamma\sin\beta & -\sin\gamma\cos\beta \\ -\sin\alpha\cos\beta & \cos\alpha\cos\beta & \sin\beta \\ \cos\alpha\sin\gamma + \sin\alpha\cos\gamma\sin\beta & \sin\alpha\sin\gamma - \cos\alpha\cos\gamma\sin\beta & \cos\gamma\cos\beta \end{pmatrix} \tag{2}$$

This matrix or its inverse have to be applied, whenever transformations from one coordinate system to the other are performed. A detailed description of the transformations can be found, for example, in Peters (2000).

2.2.2 The magnetic field onboard uncompensated ships

The vector of the measured magnetic field onboard an uncompensated ship, in the ship's coordinate system, $\vec{B}_s^M$, can be described as the sum of the geomagnetic field

vector $\vec{B}_s^E$ and the vector of the ship's interfering field $\vec{B}_s^S$:

$$\vec{B}_s^M = \vec{B}_s^E + \vec{B}_s^S \tag{3}$$

The subscript "s" denotes the ship's coordinate system.

The vector of the magnetic field generated by the ship $\vec{B}_s^S$ can be described as the sum of the effects due to the permanent magnetization of the ship's steel parts, the induced magnetization, and eddy currents. These parts form the interfering field to the measured signal. Equation 4 summarizes these components in order of significance:

$$\vec{B}_s^S = \vec{K}_s + \vec{B}_s^{ind} + \vec{B}_s^{cur} \tag{4}$$

$\vec{K}_s$ is the expression for the permanent magnetic field as measured in each of the directions of the ship's coordinate system. The permanent magnetic field is mainly caused by the remanent magnetization of the hull. (For details see chapter 2.4.5.)
$\vec{B}_s^{ind}$ is the induced magnetic field due to the magnetization of the ship's steel parts under the influence of the ambient geomagnetic field. This can be written for each component of the magnetic field in the ship's coordinate system as shown in formula 5, after Auster (1961):

$$\begin{aligned} \vec{X}_s^{ind} &= a_{11} \cdot X_s^E + a_{12} \cdot Y_s^E + a_{13} \cdot Z_s^E \\ \vec{Y}_s^{ind} &= a_{21} \cdot X_s^E + a_{22} \cdot Y_s^E + a_{23} \cdot Z_s^E \\ \vec{Z}_s^{ind} &= a_{31} \cdot X_s^E + a_{32} \cdot Y_s^E + a_{33} \cdot Z_s^E \end{aligned} \tag{5}$$

The superscript E in X_s^E, Y_s^E and Z_s^E denotes the inducing geomagnetic field, in the ship's coordinate system, and a_{ij} (i,j = 1,2,3) are the coefficients of induction. Details on the meaning of these coefficients are given in chapter 2.4.5.
Equation 5 also can be written in matrix form. This is:

$$\vec{B}_s^{ind} = \underline{A} \cdot \vec{B}_s^E. \tag{6}$$

The least significant interference to the measured signal is caused by eddy currents. Currents are induced by the ship's movement in the geomagnetic field which in turn generate a magnetic field with opposite direction than the originating field (Lorentz Law). This effect has no great importance because the movements of the ship are not very fast. However, it has been incorporated in the model since its influence cannot be completely ruled out due to the large gradients in the ship's magnetic field. Its mathematic description follows the one for the induced magnetic field.

$$\begin{aligned} \vec{X}_s^{cur} &= c_{11} \cdot \frac{\partial}{\partial t}(X_s^E + X_s^S) + c_{12} \cdot \frac{\partial}{\partial t}(Y_s^E + Y_s^S) + c_{13} \cdot \frac{\partial}{\partial t}(Z_s^E + Z_s^S) \\ \vec{X}_s^{cur} &= c_{21} \cdot \frac{\partial}{\partial t}(X_s^E + X_s^S) + c_{22} \cdot \frac{\partial}{\partial t}(Y_s^E + Y_s^S) + c_{23} \cdot \frac{\partial}{\partial t}(Z_s^E + Z_s^S) \\ \vec{X}_s^{cur} &= c_{31} \cdot \frac{\partial}{\partial t}(X_s^E + X_s^S) + c_{32} \cdot \frac{\partial}{\partial t}(Y_s^E + Y_s^S) + c_{33} \cdot \frac{\partial}{\partial t}(Z_s^E + Z_s^S) \end{aligned} \tag{7}$$

According to equation 7, the ship's field due to eddy currents depends on the variation of the ambient geomagnetic field and the ship's field itself. Using equation 3 this is equivalent to the rate of change of the measured magnetic field.
In matrix form this can be written as:

$$\vec{B}_s^{cur} = \underline{C} \cdot \frac{\partial}{\partial t}(\vec{B}_s^E + \vec{B}_s^S) = \underline{C} \cdot \frac{\partial}{\partial t}\vec{B}_s^M. \tag{8}$$

Combining all the components of the ship's interfering field we can rewrite equation 3 for the measured magnetic field in terms of the magnetic properties of the ship and the ambient geomagnetic field in the ship's coordinate system:

$$\vec{B}_s^M = \underline{A} \cdot \vec{B}_s^E + \underline{C} \cdot \frac{\partial}{\partial t}\vec{B}_s^M + \vec{B}_s^E + \vec{K}_s \tag{9}$$

Since we are interested in the earth's magnetic field vector as defined in the geodetic coordinate system, $\vec{B}_s^E$ should be replaced by:

$$\vec{B}_s^E = \underline{D} \cdot \vec{B}_e^E \tag{10}$$

This describes the rotation of the local geomagnetic field from the geodetic coordinate system to the ship's coordinate system.
Incorporating this into equation 9 results in the following differential equation for the measured magnetic field:

$$\vec{B}_s^M = \underline{A} \cdot \underline{D} \cdot \vec{B}_e^E + \underline{C} \cdot \frac{\partial}{\partial t}\vec{B}_e^M + \underline{D} \cdot \vec{B}_e^E + \vec{K}_s \tag{11}$$

In this, 21 coefficients are used to describe the permanent and induced ship's field and the field due to eddy currents. As will be explained in detail in chapter 2.4, the calculation of these coefficients is done in three steps. In a first step, only the coefficients for the induced and permanent ship's field are calculated. After a forward calculation of the ship's field for induced and permanent magnetism (step 2), this is removed from the measured signal. The residual field is then used in a third step to calculate the coefficients for the induced field due to eddy currents.

Finally, it should be noted that semipermanent magnetism also plays a significant role in ship's magnetism. Unfortunately, at the moment there exists no reliable model to describe the fields generated by this kind of magnetism. Consequently, in this study, the effect of semipermanent magnetism has not been included in the calculations. However, it is known that the influence of semipermanent fields is largest after sudden course changes (e.g. profile turns). Hence, during processing, if several minutes of data are removed after any significant course change, short term effects can be significantly reduced, and are not further discussed in this work.

2.3 The data acquisition system

The recorded magnetometer data have to be combined with simultaneously recorded data of the ship's attitude and position in order to correct the measured magnetic field for the ship's interfering field. The flowchart in figure 2.3-1 gives an overview of the components of the data acquisition system used onboard RV *Polarstern* to record the magnetic field, attitude, and position of the ship.

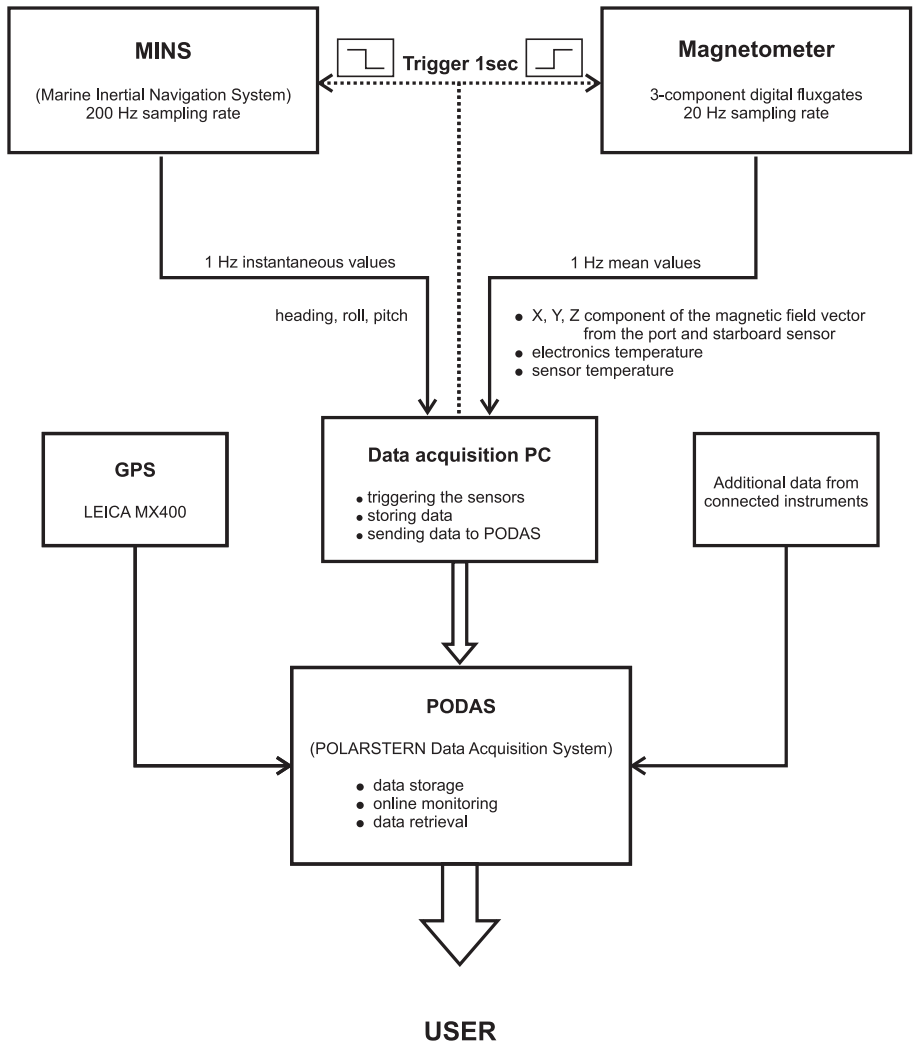

Figure 2.3-1: Flowchart of the data acquisition system used onboard RV *Polarstern* for measuring the variations of the earth's magnetic field.

The most important components are the magnetometer system, the marine inertial navigation system (MINS) and the global positioning system (GPS). Simultaneous recordings of magnetometer and attitude data are crucial for any successful compensation of the magnetometer data. A time shift of 1 sec between attitute and magnetometer data can result in an error of the compensated data of several hun-

dred nanotesla. Simultaneity is achieved by a common trigger signal generated every second by the primary data acquisition computer and sent to both systems. The resulting data stream comprises of 1 Hz instantaneous values for heading, roll and pitch from the MINS, and 1 Hz mean values for the components of the magnetic field vector (X,Y,Z) and additional recordings of the electronics and sensor temperatures from the magnetometer system. This data set is sent every second to the ship wide data acquisition system (called PODAS) and combined with additional information like the actual position of the ship. For data processing and online monitoring, data can be retrieved from PODAS through a local area network onboard the ship.
In the next sections, a short description of the magnetometer sensor system and its installation onboard RV *Polarstern*, and of the attitude sensor system (MINS), will be given.

2.3.1 The magnetometer sensor system

Two three-component digital fluxgate magnetometers are installed onboard RV *Polarstern* (Magson GmbH, Berlin). The concept and realization of a digital fluxgate magnetometer is described in Auster et al. (1995), Auster et al. (1998), and Rustenbach et al. (1998). In contrast to analog systems, in this kinds of magnetometer systems, the sensor signal is converted from analog to digital directly after leaving the preamplifier. The feedback signal for the fluxgate sensors is then calculated by

Figure 2.3-2: Overview of RV *Polarstern*. The magnetometer sensors are mounted astern on the main platform of the crow's nest as indicated.

software and sent back to the fluxgates after back-conversion from digital to analog. The main advantage of this near-sensor digitization comes from the reduced influence of temperature changes that can introduce DC-shifts and change filter characteristics. Since RV *Polarstern* operates mainly in polar regions and crosses the equator twice a year, temperature stability is crucial for continuous measurements in both hemispheres without time consuming calibrations. The resolution of the final sensor signal is better than ±10 pT, and the dynamic range realized through these magnetometers is ±100000 nT (Kopsch and Kroth, 2003). This is of great importance since the range of the vertical component of the measured magnetic field varies between -50000 nT in Antarctica and 62000 nT in the high Arctic. Long term stability of the sensor system is given to be better than 10 nT/year (Kopsch and Kroth, 2003). Normally, expeditions last for two to three months. For this time range, any drift in magnetometer data can be neglected from the above mentioned specification.

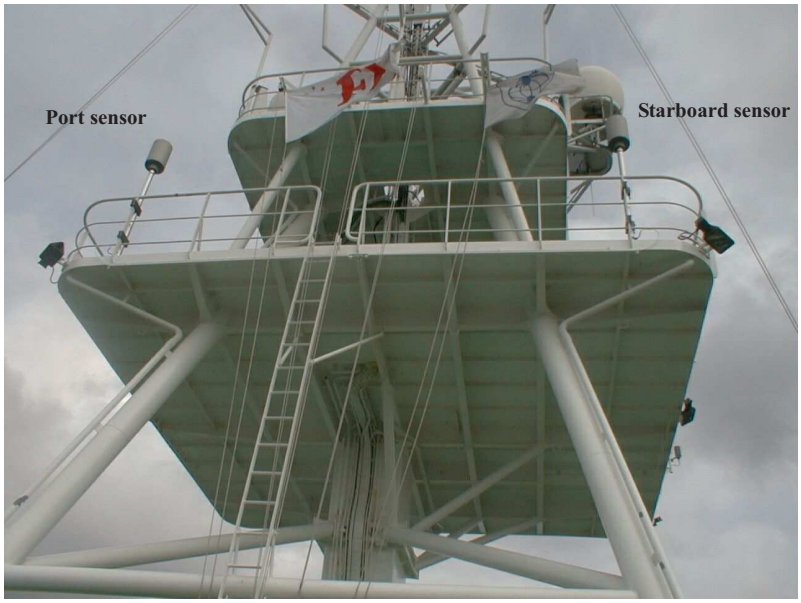

Figure 2.3-3: The upper and lower platform of the crow's nest, from abaft. The aluminium rods of the port and starboard sensor are fixed to the railing carrying the sensors about 2 m above the platform.

The fluxgate sensors are mounted astern on the port and starboard side of the main platform of the crow's nest (Figs. 2.3-2 and 2.3-3). This platform is about 6.6 m above the hull and the sensors are mounted on rods, made of a special aluminium alloy, a further 2.0 m above the platform. Thus, the active part of the sensors is deployed about 8.6 m from the hull. This position has been chosen as a compromise between having the sensor a large distance from the hull and the need to minimize possible errors due to independent vibrations of the sensor's housing with respect

to the hull. Vibrations would result in uncertainties in the attitude of the sensors that lead to uncompensated high frequency noise in the processed data.

2.3.2 The attitude sensor system

Precise knowledge of the ship's attitude is of crucial importance for the compensation of shipborne magnetic data. Initial tests with common acceleration sensors integrated in the housing of the magnetometers did not yield the necessary accuracy for this application (Kopsch et al., 2000). However, RV *Polarstern* is equipped with an Anschuetz Marine Inertial Navigation System (MINS) (Raytheon Marine GmbH, Kiel), a high precision attitude and reference system, which could be used instead. This system is based on a ring laser gyro technology which means that accelerations and velocities are measured through the interference of light rays, and not through moving masses (Anderson, 1986). The mean accuracies of this system are given to better than 0.050° for heading and 0.019° for roll and pitch (Raytheon Marine GmbH, Kiel). When calculating the local magnetic field vector at the magnetometer sensors during the calibration procedure, these uncertainties can result in errors in the calculated field components of up to 20 nT at a local ambient field like that in the Arctic seas ($X_e^E = 7900\ nT; Y_e^E = -1100\ nT; Z_e^E = 53300\ nT$). Although the accuracy of the MINS is much better than those achieved with usual acceleration sensors ($\sim$0.10° for roll and pitch), there is still a considerable effect on the quality of the compensated data.

The ring laser gyros of the MINS are mounted near the center of gravity in the ship's hull, about 25 m below the magnetic sensor system. As mentioned above, this distance may result in additional inaccuracies in determining the true attitude of the sensors, and finally, in high frequency noise in the compensated data. It will be shown in section 2.4, on data processing, that this noise can be significantly reduced through lowpass filtering of the compensated magnetometer data. However, attitude sensors in a close position to the magnetometer sensors would reduce this high frequency noise and result in an improved signal to noise ration. Unfortunately, high precision attitude sensors of considerable size and functionality are only rarely known.

2.4 Data processing

2.4.1 Computational concepts

For processing the shipborne magnetic anomaly data a MATLAB (The MathWorks, Inc.) software package has been developed which provides tools for fast and complete processing of the raw data. This includes the calculation of compensation

coefficients, compensation of track data, frequency analysis, calculation of cross-correlations, filtering, performing an IGRF (International Geomagnetic Reference Field) correction, and applying a daily correction (if base station data are available). In the following section, the concept for the calculation of the compensation coefficients and the compensation procedure itself, as implemented in the MATLAB programs, will be explained.

As mentioned in theory (Chapter 2.2), 21 coefficients are needed to compensate the raw magnetometer data for the ship's interfering field. These coefficients have to be determined regularly before, during and after any ship magnetic survey. Since only three independent equations, one for each principal direction (X,Y,Z) are available to constrain the coefficients, there are more coefficients than equations. This is called an under-determined system of equations. A least squares approach is used to solve this problem, as proposed by Auster (1961). Before these calculations are explained, the sequence of processing steps is introduced as displayed in figure 2.4-1.

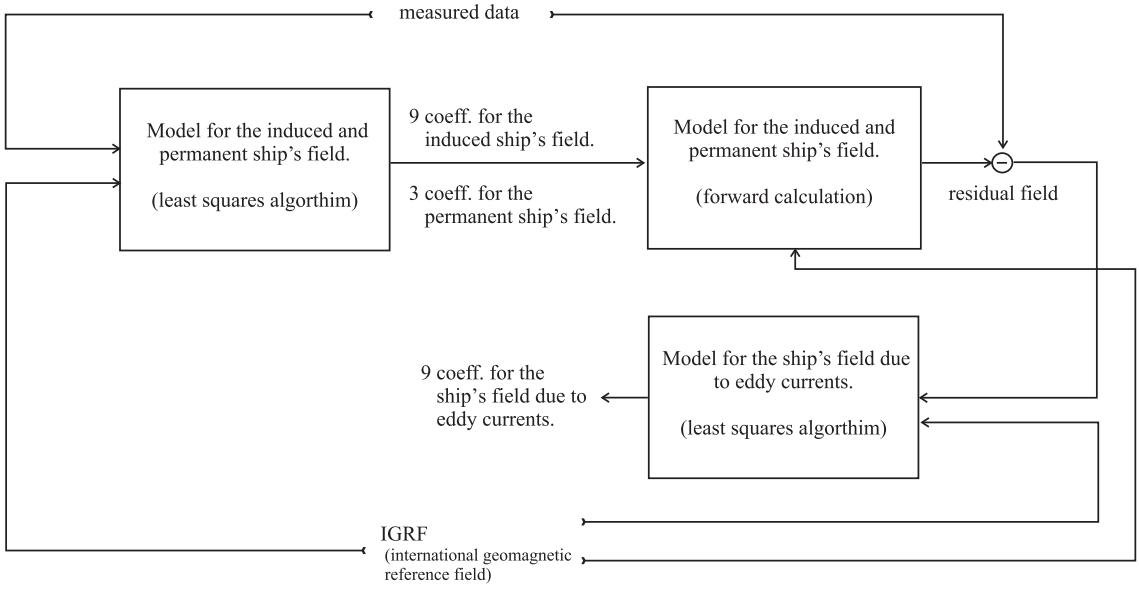

Figure 2.4-1: Flowchart for the calculation of the 21 coefficients of the permanent ship's field, the induced ship's field, and the ship's field due to eddy currents.

The processing is split into three steps. First, the nine coefficients for the induced field and the three coefficients for the permanent magnetization are calculated through a least squares algorithm. Applying these twelve coefficients to the local geomagnetic field at the compensation site, the ship's field is determined through forward calculation (step 2). This field is then removed from the measured signal. The residual field is used in the third step to calculate the nine coefficients for the

field due to eddy currents. This processing scheme for the calculation of the 21 coefficients of the ship's field correspond to a first order iteration.

In the following, the general equations needed to calculate the coefficients for the induced and permanent ship's field are given. The calculation of the coefficients for the field due to eddy currents is performed in a similar way and is not listed here explicitly.
Leaving out the expression for eddy currents, and substituting $\underline{D} \cdot B_e^E$ by B_s^E, equation 11 can be written, for example for the X-component, as shown in equation 12:

$$X_s^M = (a_{11} + 1) \cdot X_s^E + a_{12} \cdot Y_s^E + a_{13} \cdot Z_s^E + K_{1s} \tag{12}$$

K_{1s} is the component of the permanent ship's field parallel to the X_s axis. All other notations are the same as in chapter 2.2. Equation 12 can be rearranged so that:

$$(a_{11} + 1) \cdot X_s^E + a_{12} \cdot Y_s^E + a_{13} \cdot Z_s^E + K_{1s} - X_s^M = 0 \tag{13}$$

According to the least squares method, the partial derivative of the sum over all independent measurements of the squares of the left side of equation 13 has to be zero for all coefficients a_{1j} $(j = 1, 2, 3)$ and K_{1s}. That is to say:

$$\frac{\partial}{\partial(a_{1j}, K_{1s})} \left\{ \sum_{p=1}^{N} \left[(a_{11} + 1) \cdot X_s^E + a_{12} \cdot Y_s^E + a_{13} \cdot Z_s^E + K_{1s} - X_s^M \right]_p^2 \right\} = 0 \tag{14}$$

This results in four equations, each dependent on the three coefficients a_{1j} $(j = 1, 2, 3)$ and K_{1s}. This can be written in matrix form as:

$$\underline{M} \cdot \vec{C} = \vec{S} \tag{15}$$

The elements of $\underline{M}$ are the sums over all measurements of the products of the components of the known geomagnetic field at the position of the sensor:

$$\underline{M} = \begin{pmatrix} \sum X_s^E X_s^E & \sum X_s^E Y_s^E & \sum X_s^E Z_s^E & \sum X_s^E \\ \sum X_s^E Y_s^E & \sum Y_s^E Y_s^E & \sum Y_s^E Z_s^E & \sum Y_s^E \\ \sum X_s^E Z_s^E & \sum Y_s^E Z_s^E & \sum Z_s^E Z_s^E & \sum Z_s^E \\ \sum X_s^E & \sum Y_s^E & \sum Z_s^E & N \end{pmatrix},$$

in which $\sum$ denotes the sum over all N measurements, and $\vec{C}$ and $\vec{S}$ are vectors of the form:

$$\vec{C} = \begin{pmatrix} (a_{11} + 1) \\ a_{12} \\ a_{13} \\ K_{1s} \end{pmatrix}, \qquad \vec{S} = \begin{pmatrix} \sum X_s^E X_s^M \\ \sum Y_s^E X_s^M \\ \sum Z_s^E X_s^M \\ \sum X_s^M \end{pmatrix}.$$

Equation 15 is a nonhomogeneous linear system of equations that can be solved simply by matrix inversion. This is performed by Gaussian elimination. The resulting vector, $\vec{C}$, contains all four coefficients of the first of the three equations in equation 11 (omitting the field due to eddy currents). This calculation is performed for all three components of the measured magnetic field, resulting in twelve coefficients for the permanent and induced ship's field. After forward calculation of the ship's field the coefficients for the eddy current field can be calculated as visualized in figure 2.4-1.

For the compensation of profile data a formula for the local geomagnetic field in the geodetic coordinate system is needed which depends only on the measured signal and the calculated coefficients. Such an expression is provided by equation 11 which has to be solved for $\vec{B}_e^E$.

$$\vec{B}_e^E = ((\underline{A} + \underline{E}) \cdot \underline{D})^{-1} \cdot (\vec{B}_s^M - \underline{C} \cdot \frac{\partial}{\partial t}\vec{B}_s^M - \vec{K}_s) \tag{16}$$

In this, $\vec{K}$, $\underline{A}$, $\underline{C}$ refer to the coefficients for the permanent, induced and eddy current field. $\underline{E}$ refers to the identity matrix and $\underline{D}$ provides the transformation from the geodetic to the ship's coordinate system. This equation is equivalent to the matrix inversion performed to solve equation 15 for the coefficients of the induced ship's field. There, a Gaussian elimination algorithm is used three times to calculate a set of nine coefficients. Here, the matrix inversion has to be done for each record along the profile to calculate the three components of the geomagnetic field in the geodetic coordinate system. The resulting data set can be used for further processing steps like the application of filters and the performance of corrections for the International Geomagnetic Reference Field (IGRF) (IAGA, 1996), and the daily variations.

Even though, through the interpretation of vector magnetic data, more information on the position and strike of magnetic boundaries can be gained than with total-intensity data alone (Blakely et al., 1973; Seama et al., 1993), the total magnetic field, as calculated through the components of the magnetic field vector will be used for validation processes, instead, in the following chapter. Validation of the compensated data is done by a comparison with helicopter-borne data (Chapter 2.5) and a regional compilation of aeromagnetic data (Chapter 2.6). These platforms are commonly equipped with total-intensity sensor systems making any direct validation of the three component shipborne magnetometer data impossible. However, the calculation of the coefficients and compensation of calibration loops is performed for the three components of the vector magnetic data (Chapters 2.4.5 and 2.4.6).

2.4.2 The reference field at calibration sites

The procedure for calculating compensation coefficients requires a known ambient geomagnetic field at the calibration site at the time when the calibration loop is performed. Usually, the International Geomagnetic Reference Field (IGRF) (IAGA, 1996) is used for this purpose. This has to be regarded as a rough approximation to the true geomagnetic field at the desired location. The IGRF often has an error of several 100 nT, especially at sea and in the polar regions, and is considerably smoothed. Further inaccuracies arise through neglecting daily variations during calibration loops. In the polar regions, daily variations can reach peak-to-peak amplitudes of 500 nT within a couple of minutes, even on normally disturbed days. Even in the case where there is a magnetic base station nearby the calibration site (<500 km), correlations between daily variations recorded onshore and offshore must be treated with care. Offshore, the distance to any magnetic source body in the ground is usually about 3 to 5 km, whereas onshore this is often only a couple of meters. Consequently, offshore amplitudes may be reduced in size compared to simultaneous onshore registrations.

2.4.3 Position and shape of calibration loops

As already mentioned at the beginning of chapter 2, the data presented here were recorded onboard RV *Polarstern* during the ARK-XVIII/2 expedition to the Fram Strait between Greenland and Svalbard from the 26^{th} of August, 2002 to the 15^{th} of October, 2002. An overview of the survey area and the position of the calibration sites is given in figure 2.4-2. Table 2.4-T1 summarizes the date and position of each of these calibration sites. Numbers indicating the calibration sites in figure 2.4-2 are repeated in table 2.4-T1 in the first column.

Table 2.4-T1: Date and position of all calibration sites during the ARK-XVIII/2 expedition.

No	Date	Time [UTC]		Lon	Lat
	dd.mm.yyyy	Start	End		
1	28.08.2002	04:52	06:36	13.78°E	67.75°N
2	08.09.2002	18:35	19:42	04.00°E	81.03°N
3	21.09.2002	17:39	19:22	00.92°E	78.47°N
4	30.09.2002	06:57	09:00	00.35°E	77.28°N
5	09.10.2002	16:52	17:44	05.47°E	77.83°N

One or more loops were performed at each calibration site (Fig. 2.4-3). In the case

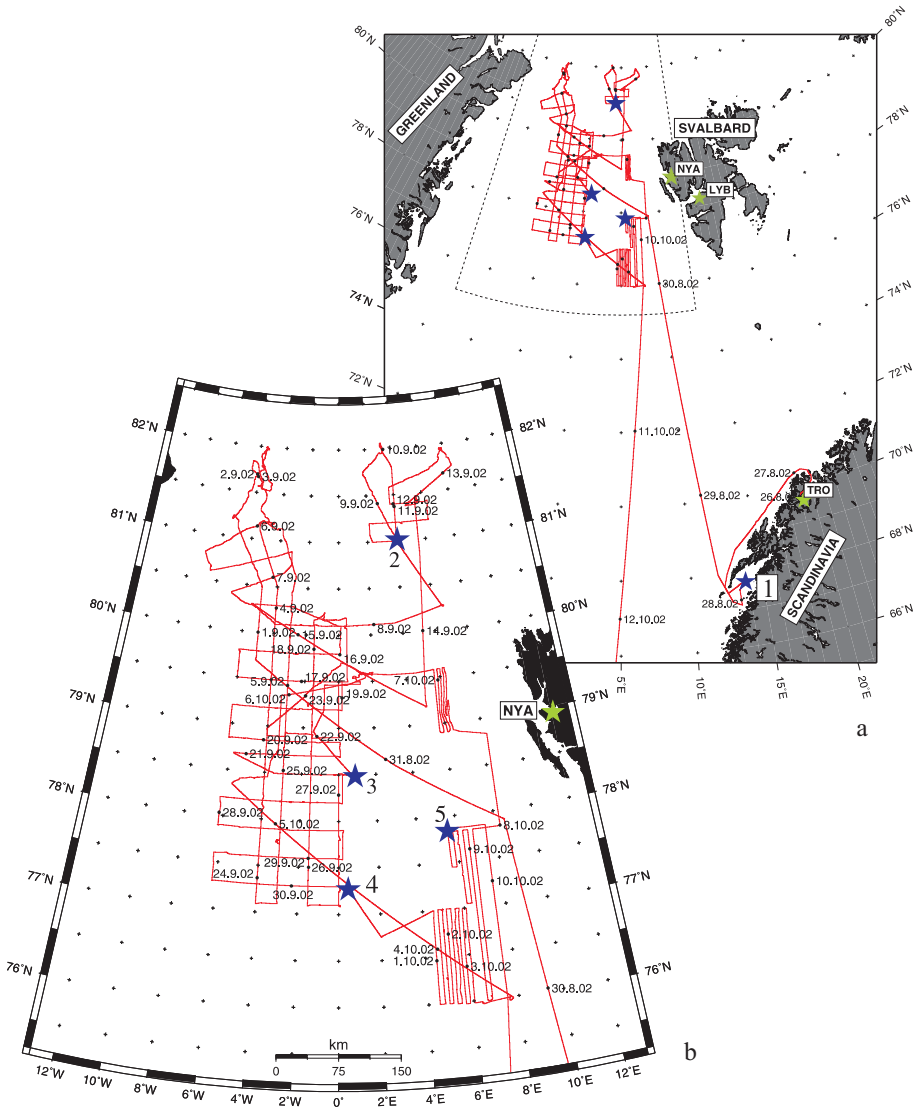

Figure 2.4-2: Track plot for the ARK-XVIII/2 expedition to the Fram Strait between Greenland and Svalbard. Part (a) gives an overview of the complete cruise, starting in Tromsø on the 26^{th} of August, 2002. Part (b) is a more detailed map with the position of the calibration sites marked with blue stars and numbers. The numbers of the calibration sites correspond to the numbering in table 2.4-T1. Additionally, the beginning of each day is indicated by a black dot and a label of the corresponding date.

of the calibration on the 21^{st} of September, 2002, a figure eight was chosen (Fig. 2.4-3a). By performing a figure eight, the effect of semipermanent magnetic fields, which are not included in the model as mentioned in chapter 2.2, should be reduced. Through the evaluation of the existing data, the advantage of a figure eight cannot be confirmed or ruled out. Consequently, the loops of the eight were treated as single loops. The loops shown in figure 2.4-3 have a radius of about 1.8 km (1 nm), and were conducted with a velocity of about 5 - 7 kt. After several tests, this has been chosen as the optimum size and velocity for calibration loops with RV *Polarstern*.

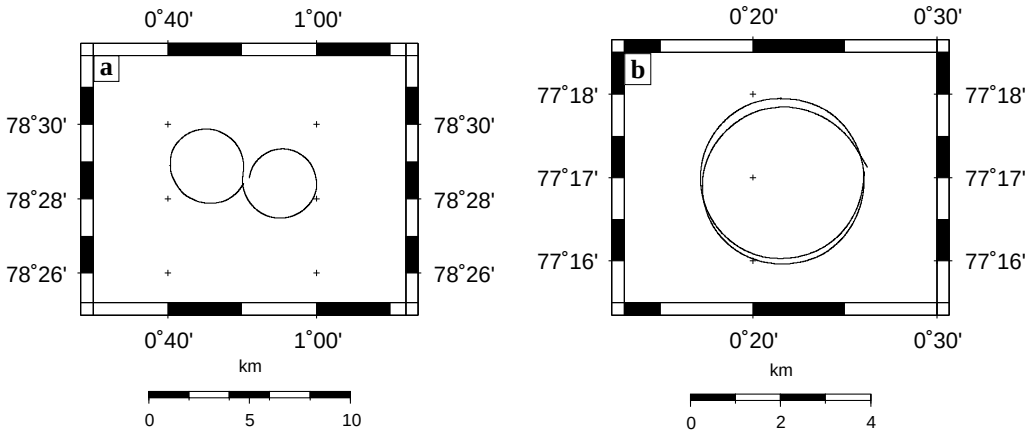

Figure 2.4-3: Track plots of the calibration loops on the 21^{st} of September, 2002 (a) and the 30^{th} of September, 2002 (b).

A significantly reduced radius would result in a systematic heeling error, and loops with a significantly larger radius might encounter spatial gradients due to variations of the local geomagnetic field, and due to the longer duration, the possible influence of daily variations would be enlarged.

2.4.4 Attitude data during calibration loops

The algorithm for the calculation of compensation coefficients (Chapter 2.4.1) assumes uniformly distributed attitude angles. In order to reduce the bias in the calculated coefficients due to nonuniformly distributed heading angles, a histogram plot for each calibration loop is made. Data used for the calculation of the coefficients is selected with respect to the loop's beginning and end in such a way that the distribution of the heading angle is as uniform as possible. Histogram plots are also generated for pitch and roll in order to inspect the distribution of the respective angles, but no special selections are made with respect to these angles.

Figure 2.4-4 shows two examples of selected calibration loop data for the 28^{th} of September, 2002 and the 30^{th} of September, 2002. The difference between quiet (30.09.2002) and rough (28.08.2002) sea state is evident. While roll and pitch angles are sharply centered about their respective mean values for calibration loops in a quiet sea (30.09.2002) there is a broad distribution over a larger range of values for the loop in rough water (28.08.2002).

Although the calibration loop from the 30^{th} of September, 2002 seems to be a perfect circle in figure 2.4-3b, figure 2.4-4 shows that there is a considerable peak in the heading angle at about 90°. This corresponds to the northernmost part of the upper

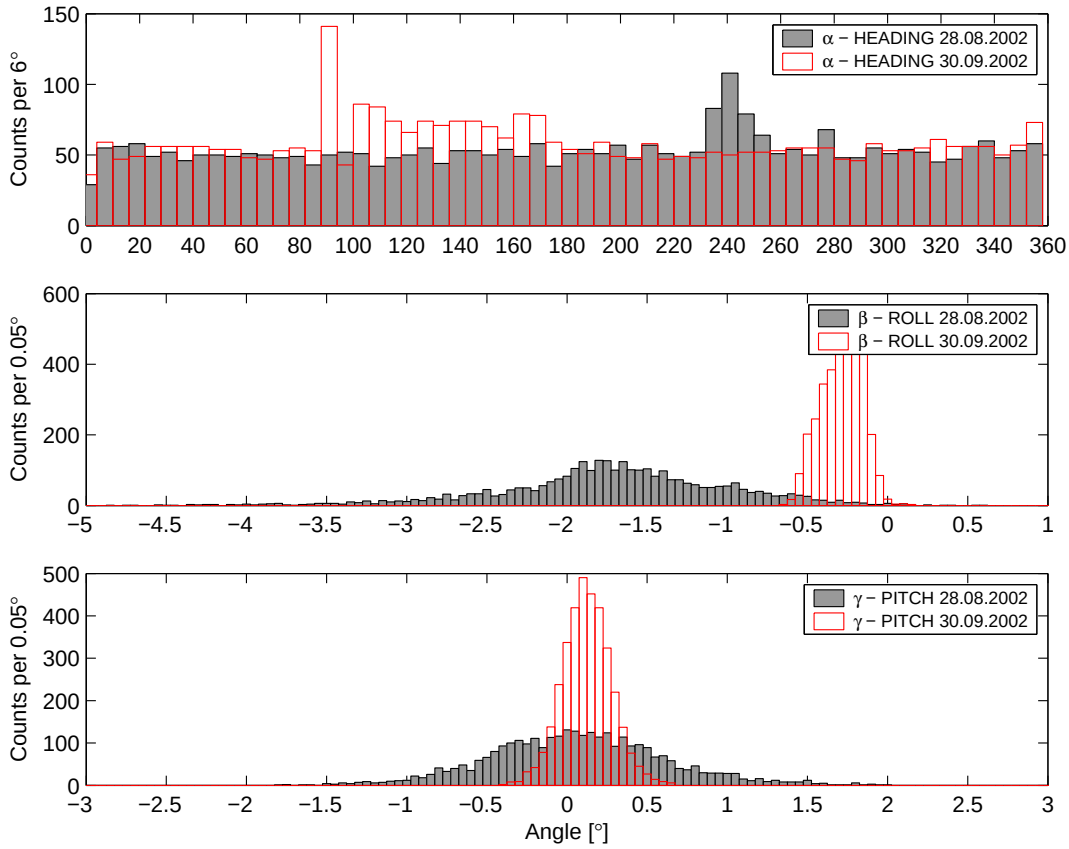

Figure 2.4-4: Histogram distribution of the attitude angles (heading, roll, pitch) for the calibration loops on the 28^{th} of September, 2002 and 30^{th} of September, 2002.

loop in figure 2.4-3b which is slightly flattened. Such peaks resulting from constant heading angles within the loop, cannot be removed since this would significantly disrupt the continuity of the data and lead to large errors in the calculation of the time derivative.

2.4.5 Evaluation of calibration loops

After selecting the appropriate data set from the ship's track and splitting multiple loops into single ones, coefficients are calculated for each calibration loop. Tables with the coefficients for the induced and permanent ship's field for all calibration loops and both magnetometers can be found in Appendix (A) in tables A-1 and A-2 . The mean values and the corresponding standard deviations are also appended to the end of each table.

In the following, only the coefficients for the induced and permanent ship's field are discussed since the coefficients for the eddy currents field are comparatively

small and their meaning with respect to the geometry of the ship is of minor significance.

From tables A-1 and A-2 , a strong variation is apparent in the coefficients for the permanent ship's field and those that are related to the vertical component of the inducing field (a_{13}, a_{23}, a_{33}). There are several possible reasons for these strong variations:

- One possible cause might be any inaccuracy and/or instability of the algorithm used to calculate the coefficients. A test was carried out on the stability of the results by calculating the coefficients for the first calibration loop on the 28^{th} of August, 2002 after 10% of the data points were randomly removed. This calculation was repeated 100 times. The resulting mean variation in the calculated coefficients is below 1%. Consequently the algorithm is unlikely to be the cause of the large variations in the coefficients. The algorithm is stable and the results are well defined for each calibration loop.

- The strong variations in the coefficients depending on the vertical component of the inducing field arise from the comparatively small variations in Z during one calibration loop. An example on this is given in figure 2.4-5, showing the raw data from the first calibration loop, performed on the 30^{th} of September, 2002. While the X- and Y-component vary within a range of about $\pm$10000 nT during one loop, variations of less than $\pm$500 nT characterize the Z-component. This reduced variation in Z causes large uncertainties in the determination of the corresponding coefficients using a least squares fit, and consequently is probably the most important reason for the large variations in these coefficients.

- A third reason for the large variations in the coefficients in all calibration loops may be the influence of semipermanent magnetic field effects. Until now, no correlation between the change in the coefficients and the possible influence of semipermanent field effects has been made. Thus, its influence can neither be confirmed nor rejected.

Despite the large variations of some of the coefficients for the induced and permanent ship's field, some general remarks on the sign and size of the coefficients can be made. A geometrical interpretation of the coefficients is used for this purpose.
The coefficients for the permanent ship's field are correlated with constant field components in the direction of the ship's coordinate system. The different sign of K_2 (cross field component) (Tables A-1 and A-2) for the port and starboard magnetometer represents the different influence of the central mast of the crow's nest

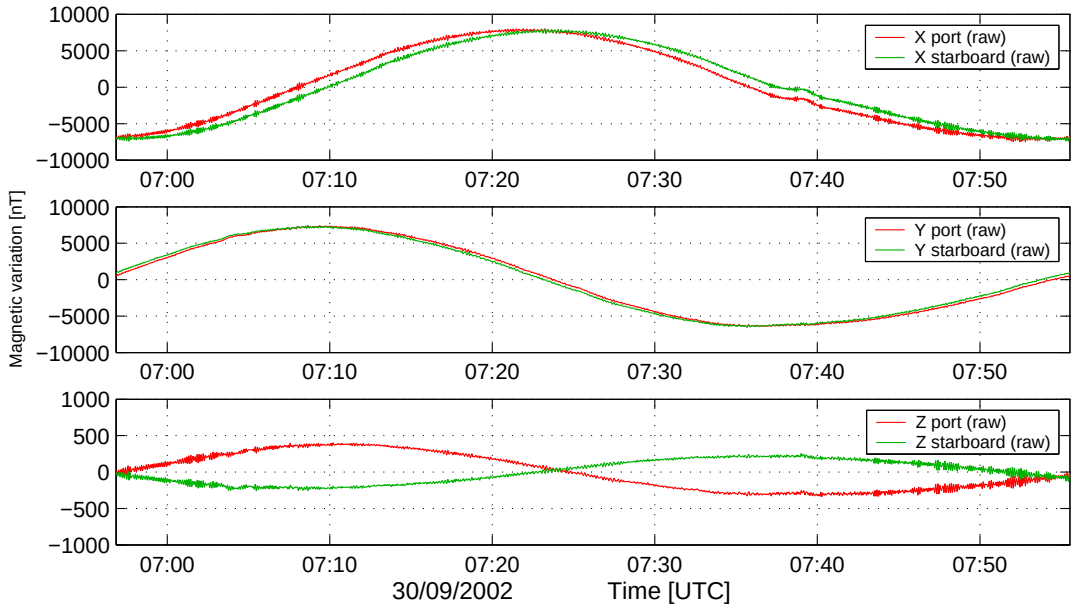

Figure 2.4-5: Raw magnetometer data for the first calibration loop performed on the 30^{th} September, 2002. Note the different scale for Z and the horizontal components. The mean of each component has been removed .

(Fig. 2.4-6). This magnetically prominent feature passes the crow's nest about 0.5 m port of the center line of the platform. The horizontal field generated by the mast is approximated by a dipole centered in the middle of the mast. The different signs of K_2 for the port and starboard sensors are apparent when splitting the horizontal field due to the dipole into its components at the position of the sensors (Fig. 2.4-6). The different size of this permanent field component also can be inferred from figure 2.4-6. Due to the closer position of the port sensor to the axes of the dipole the magnetic field lines at the position of the port sensor are directed more towards the central mast than at the position of the starboard sensor. Consequently, the coefficient for the cross field component of the ship's permanent field is smaller for the port sensor than for the starboard sensor, independent of the strength of the dipole.

According to this interpretation of the coefficients for the permanent ship's field, coefficient K_1 should be positive and larger for the port sensor than for the starboard sensor. Unfortunately, this cannot be confirmed from the values given in tables A-1 and A-2 . The large variations in K_1 for both sensors show that this coefficient is very badly constrained and not suitable for detailed discussion.

The positive sign of the vertical component of the permanent ship's field for both sensors indicates a direction towards the ship's keel. This can be correlated with the permanent magnetization of the central mast of the crow's nest. The keelward

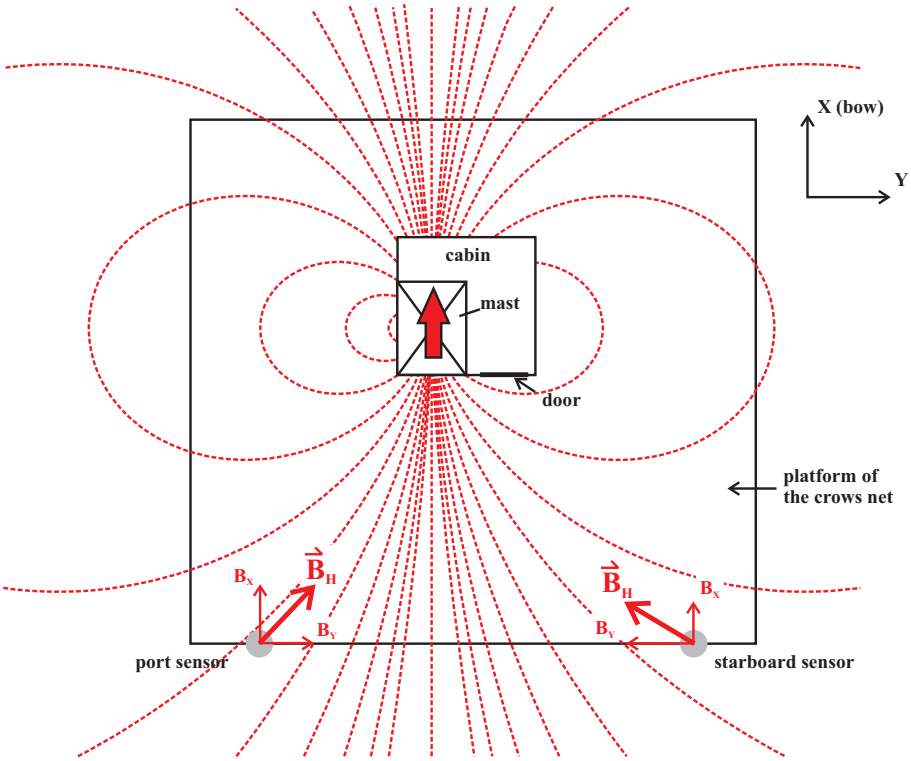

Figure 2.4-6: Sketch of the crow's nest showing the position of the port and starboard magnetometer sensors in relation to the mast. In the upper right corner, the local ship's coordinate system is shown. The assumption of a dipole centered in the middle of the mast of the crows net is made to explain the different sign and size of the horizontal components of the ship's permanent field. Red dashed lines are the magnetic field lines due to the dipole. The red arrows at the sensors' position indicate the direction of the horizontal magnetic field and their components.

direction can be explained by the fact that the ship was built in northern Germany where the inclination of the geomagnetic field is larger than 60°. The ship's steel gets at least partially remagnetized when the different parts of the ship are welded in the shipyard. The different size can be explained by the closer position of the port sensor to the central mast of the crow's nest.

The coefficients of the induced ship's field can be ascribed to a simplified geometrical distribution of bars of induction onboard the ship, as shown in figure 2.4-7. According to this, a positive a_{11} coefficient, which results in an enhancement of the magnetic field component B_X, pointing towards the bow, can be explained by the existence of two bars of induction in front of and behind the location of the magnetometer (Figure 2.4-7 upper left sketch). A single bar of induction crossing the position of the magnetometer (above or below) will result in an induced field opposite to the direction of the inducing field. In this way, the sign of all nine coefficients of induction can be correlated with the geometry of the ship.

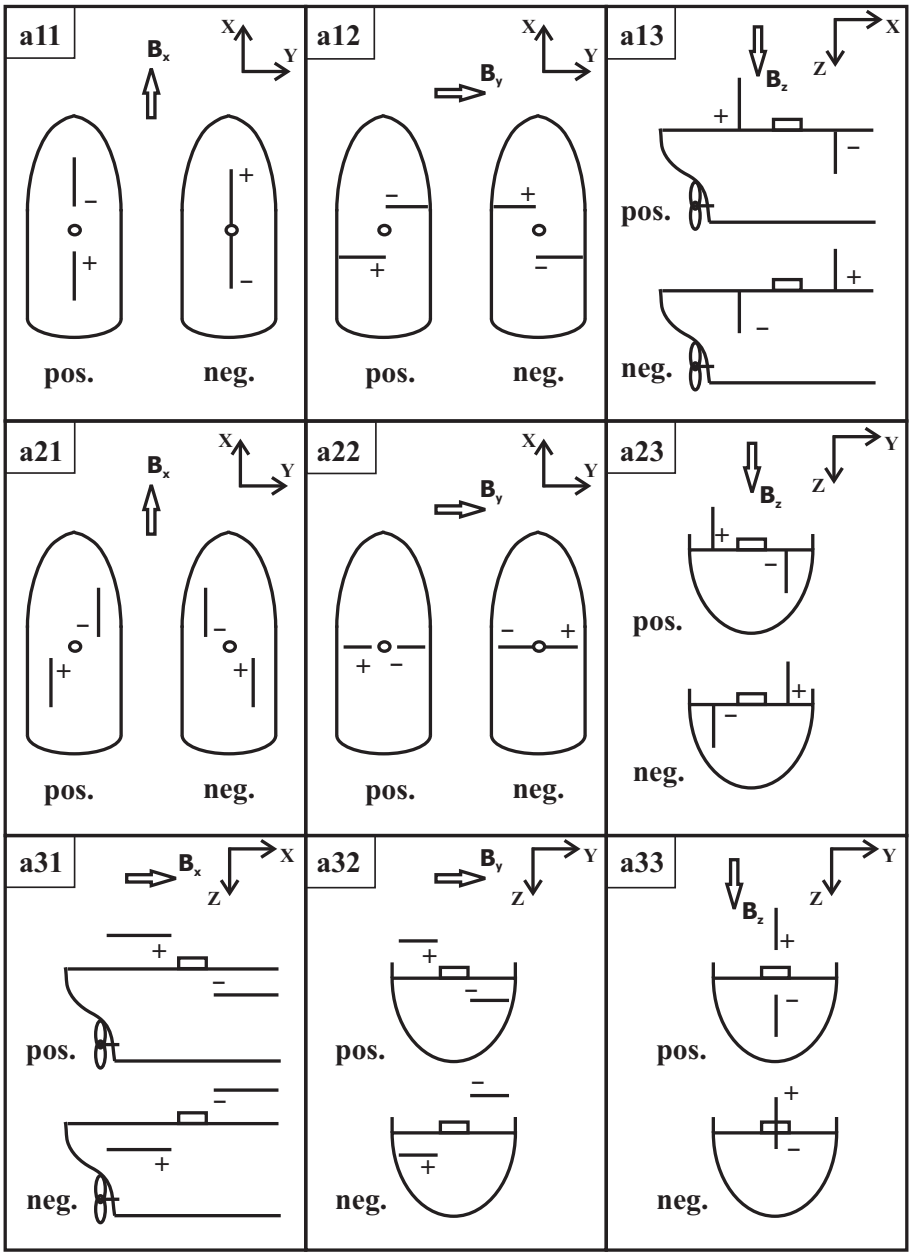

Figure 2.4-7: Bars of induction and their relation to the sign of the coefficients for the induced ship's field, after Müller and Krauß, 1983. A correlation with the calculated coefficients for expedition ARK-XVII/2 is given in the text. $B_{X,Y,Z}$ denotes the component of the inducing field. In the upper right corner of each sketch the orientation of the local coordinate system is given. The plus sign indicates the north end of the bar of induction due to the influence of the inducing field and the minus sign the south end of the bar of induction. The field outside the bar is always oriented from plus (north) to minus (south).

For validation, the sign of the most important coefficients (a_{11}, a_{22}, a_{33}), calculated during the ARK-XVIII/2 expedition onboard RV *Polarstern*, will be correlated with constructive elements of the ship.

In tables A-1 and A-2 , coefficient a_{11} is always negative for the port and starboard sensor, indicating a field of induction opposite to the direction of the inducing field. The corresponding geometrical model can be found in figure 2.4-7 in the right sketch in the upper left corner. According to the sketch, a single bar of induction crossing the position of the sensor is responsible for the negative sign of a_{11}. This clearly can be correlated with the hull. Coefficient a_{22} also has a negative sign for both sensors. According to figure 2.4-7, this again is explained by a single bar of induction through the position of the sensor, this time athwartships. This can be explained by the hull and steel cross members. Additionally, the athwartships part of the crow's nest railing, passing just 1 m below the position of the sensors, can further enhance this effect of a negative a_{22}. The close position of the sensors to the crow's net railing might be the reason why this coefficient is the largest of the three main axes elements (a_{11},a_{22} a_{33}). Coefficient a_{33} has a positive sign for both sensors. In agreement with figure 2.4-7, this is the effect of the upper and lower platform of the crow's nest.

This discussion shows that, although the variance of the calculated coefficients is rather high, their general sign and relative size can be explained by the ship's geometry and thus supports the calculations as performed with the algorithm.

2.4.6 Compensation of calibration loops

After the evaluation of the coefficients for the ship's field, the data acquired during the corresponding calibration loops can be compensated. Two ratios are calculated to verify the quality of the compensation:

- The first ratio is the improvement ratio (IR). This is the ratio of high frequency noise before and after compensation. The high frequency noise is extracted from the data by applying a highpass filter with a cutoff frequency at 0.04 Hz (25 sec). The standard deviation of both signals is used to calculate the ratio.

- The second ratio is the ratio of the standard deviation of the IGRF along the loop to the standard deviation of the lowpass filtered and compensated data (here named quality ratio (QR)). The applied lowpass filter has its cutoff frequency at 0.033 Hz (30 sec). This lowpass filter is the same as the one that is later used for the processing of profile data and will be discussed there in greater detail.

Since the results for the compensated data for the port and starboard sensor are almost the same, only the results from the port sensor will be discussed from now on. A comparison between the two sensors will be given in chapter 2.4.7.
Two examples for the compensation of calibration loop data are given and compared

in order to investigate the quality of the compensated data acquired under different sea states. The first (30^{th} of September, 2002) set of data were acquired during a period of quiet sea state and the second during strong winds and a moderate to rough sea state (9^{th} of October, 2002). Figure 2.4-2 and table 2.4-T1 provide details to the locations of the calibration sites.

Calibration loop from the 30^{th} of September, 2002

The raw data for the first of the two calibration loops on the 30^{th} of September, 2002 already were shown in figure 2.4-5. These data are dominated by variations in the horizontal component of ±10000 nT, and ±1000 nT in the vertical component, of the measured magnetic field. The corresponding attitude data is shown in figure 2.4-8.

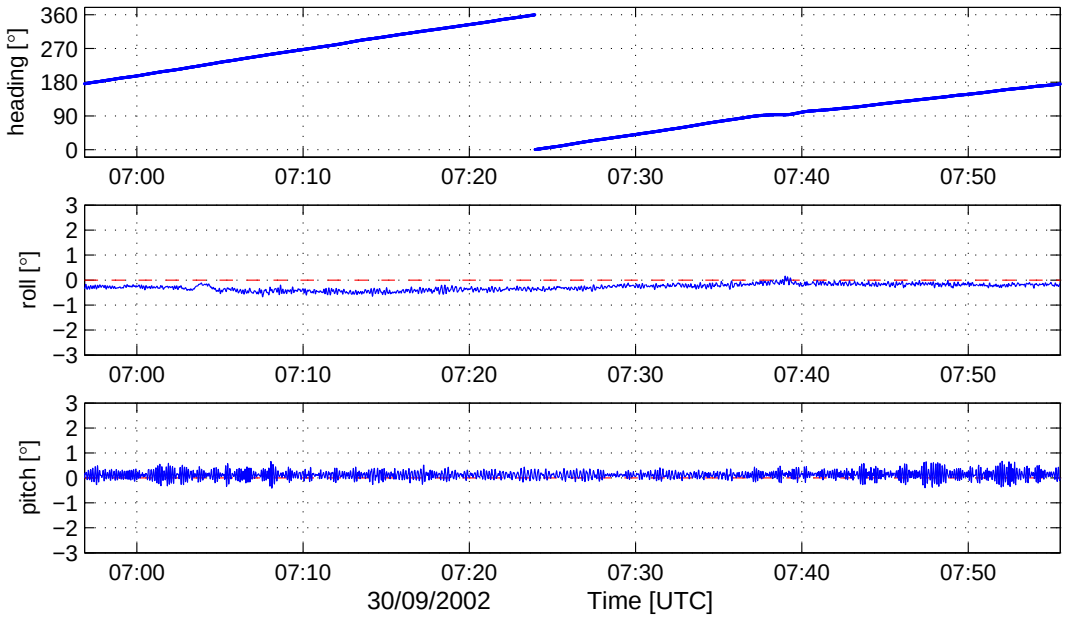

Figure 2.4-8: Attitude data for the calibration loop on the 30^{th} of September, 2002.

The quiet sea state at this calibration site is apparent from the minimal variations in roll and pitch throughout the loop. Variations in these angles are less than ±0.5°. Heading varies through 360°, starting at 180°, which corresponds to a southerly course turning clockwise. The components of the compensated magnetic field are shown in figure 2.4-9. The IR and QR, including all standard deviations used to calculate them are shown in table 2.4-T2.

The long wavelength variations in the X-, and Y-component of the compensated magnetic field are strongly reduced to less than 50 nT maximum amplitude. Comparison of the standard deviations of these components with those calculated from

Table 2.4-T2: Improvement ratio (IR), quality ratio (QR) and the according standard deviations for all components of the magnetic field vector and the total magnetic field, for the port sensor during the calibration loop on the 30^{th} of September, 2002. HP_{raw}: standard deviation of highpass filtered raw data; HP_{comp}: standard deviation of highpass filtered compensated data; IGRF: standard deviation of the IGRF along track; LP_{comp}: standard deviation of lowpass filtered compensated data.

Component	HP_{raw} [nT]	HP_{comp} [nT]	IR	IGRF [nT]	LP_{comp} [nT]	QR
X	149.2	10.3	14.5	4.8	13.7	0.4
Y	55.6	11.0	5.0	5.6	15.0	0.4
Z	17.7	4.6	3.9	2.9	7.8	0.4
F	14.4	5.1	2.8	2.2	6.6	0.3

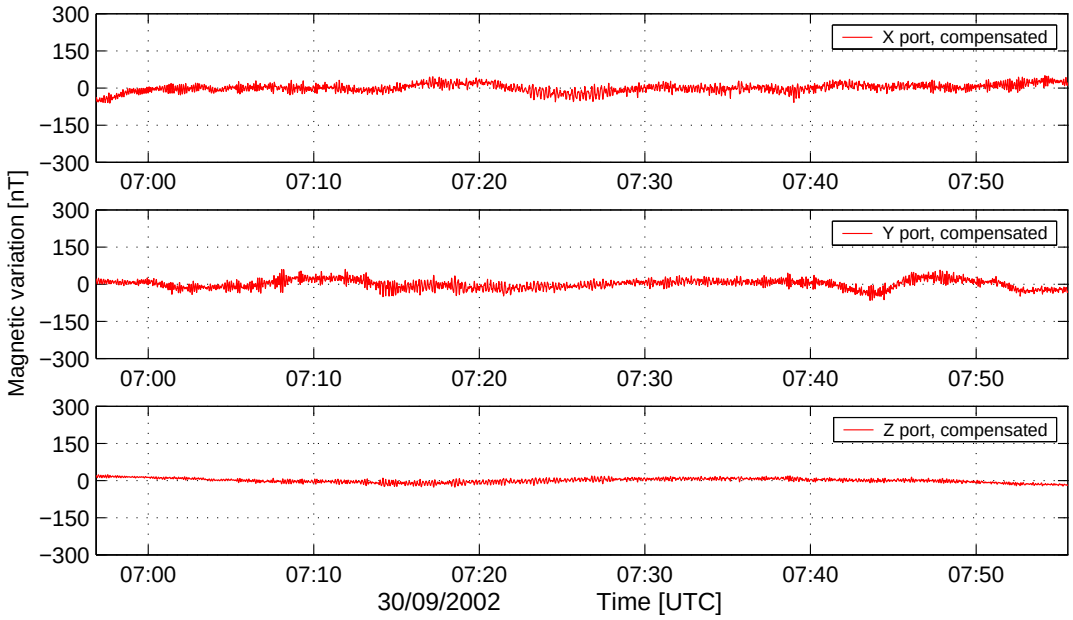

Figure 2.4-9: Compensated magnetic anomaly data for the calibration loop on the 30^{th} of September, 2002. Note that the mean of each component has been removed.

the IGRF results in a quality ratio of 0.4. According to this, the mean error in the calculated horizontal field components is below 15 nT. For the Z-component, the long wavelength variations are below ±20 nT maximum amplitude and the mean error is about 7.8 nT.

In the high frequency domain, a significant reduction of noise correlated with the movements of the ship can be achieved through the compensation of the horizontal

components. Figures 2.4-10 and 2.4-11 show coherence plots for the X-component with respect to pitch before and after compensation, and of the Y-component with respect to roll. In both cases, compensation corresponds to a decorrelation of the respective dependencies. Note that the strong correlation of the X-component with respect to pitch is also expressed in the relative size of coefficient a_{13} with respect to the other two coefficients that are correlated with the field of induction in the X-direction. Hence, this coefficient has the largest influence on the field of induction in the fore and aft directions (see table A-1 in the appendix for a comparison). The resulting noise level after compensation is about 11 nT in the horizontal components. The Z-component does not correlate well with the attitude angles but has already a reduced noise level in the raw data compared to the horizontal components and can be compensated to better than 5 nT in the high frequency domain.

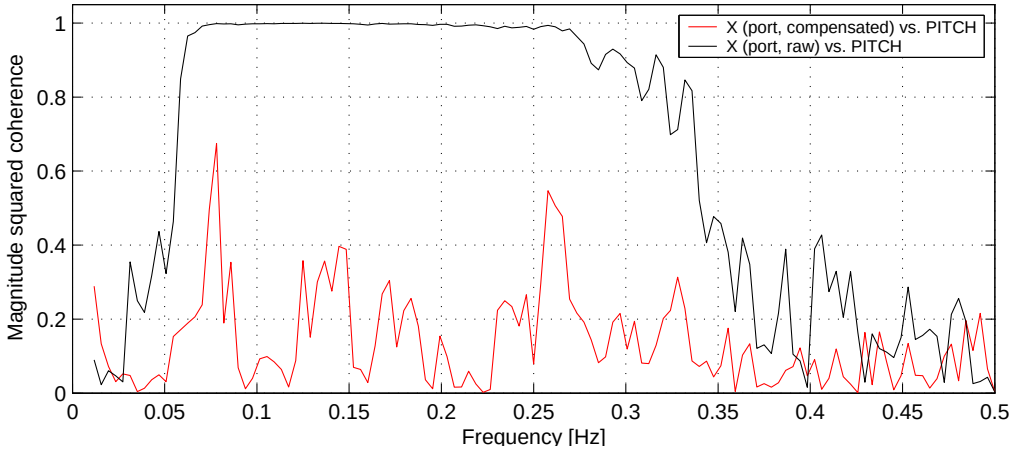

Figure 2.4-10: Coherence plot for the X-component of the measured and compensated magnetic field versus pitch for the calibration loop on the 30^{th} of September, 2002.

The intensity of the total magnetic field is of great importance for geoscientific interpretations. Accordingly, the total field is calculated from the components of the raw and compensated magnetic field, and is also used for quality control in this section. In figure 2.4-12, the final total magnetic field is shown after lowpass filtering of the compensated signal and applying an IGRF correction. The mean variations of the compensated data in the short- and long-wavelength domains are listed in table 2.4-T2. The lowpass filter applied here is the same as for the calculation of the quality ratio and the final processing of profile data, using a cutoff frequency of 0.033 Hz (30 sec). Further discussion of the filter is given in chapter 2.4.8. The filtered and IGRF corrected signal of the total field has a very smooth appearance, with a mean variation of only 6.6 nT and a maximum variation of less than 15 nT. Additionally, simultaneous recordings from the geomagnetic observatory in NyÅlesund, Svalbard

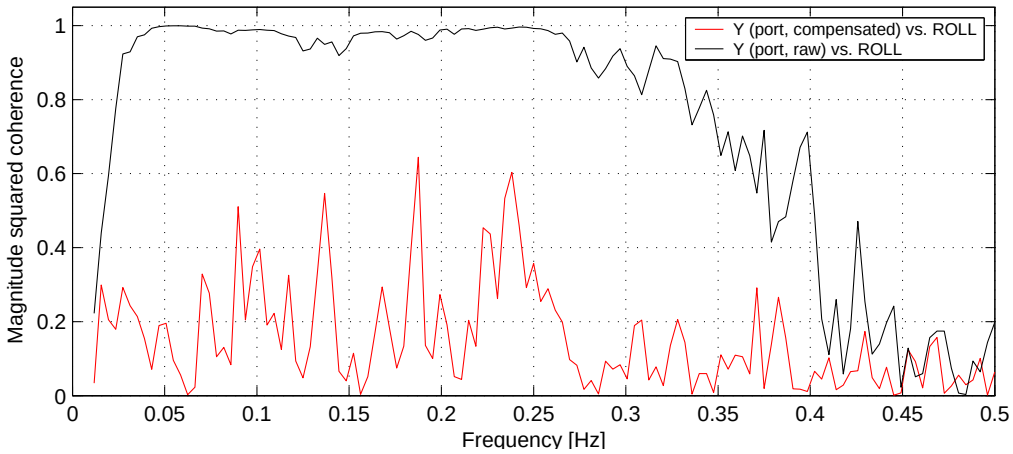

Figure 2.4-11: Coherence plot for the Y-component of the measured and compensated magnetic field versus roll for the calibration loop on the 30^{th} of September, 2002.

(about 300 km distant) and the variation of the IGRF along the calibration loop are shown in figure 2.4-12. The strong magnetic variations in the NyÅlesund base station data are neither visible in the raw nor in the compensated ship data. As already mentioned in chapter 2.4.2, correlations between onshore base station data and offshore recordings should only be applied where good correlations between both sites can be proved. Here, any base station correction would result in huge errors in the compensated signal.

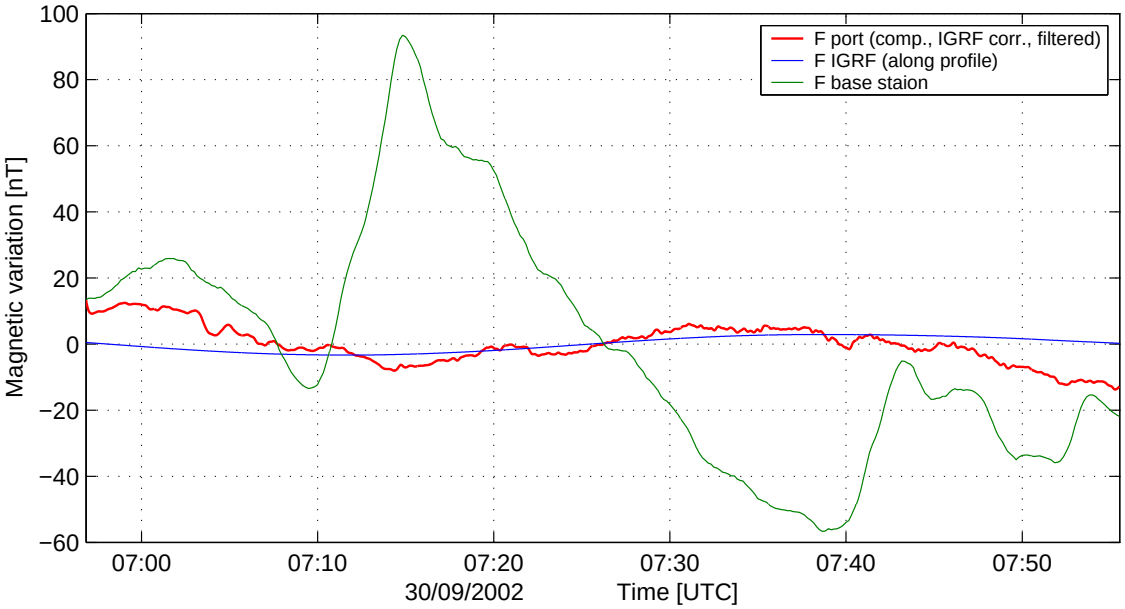

Figure 2.4-12: Compensated, IGRF corrected and filtered total magnetic anomaly data for the port sensor. Also shown are the base station readings from the nearest base station in NyÅlesund, Svalbard, and the variations of the IGRF calculated along the track.

The results for the compensated ship magnetic data show that, under quiet sea conditions, the total magnetic field can be compensated and filtered to a maximum error of better than 15 nT and a mean accuracy of better than 10 nT. Horizontal resolution strongly depends on the filters used. Estimates will be evaluated in chapters 2.4.8 and 2.5.

Calibration loop from the 9^{th} of October, 2002

The raw data for the calibration loop on the 09^{th} of October, 2002 are presented in figure 2.4-13. This loop was performed during moderate to rough sea state. Similarly to the raw data for the calibration loop on the 30^{th} of September, 2002, the horizontal components vary with amplitudes of about 10000 nT and the vertical component varies with amplitudes less than 500 nT. Even upon visual inspection, the higher noise level in the raw data can be appreciated, compared to the calibration loop on the 30^{th} of September, 2002.

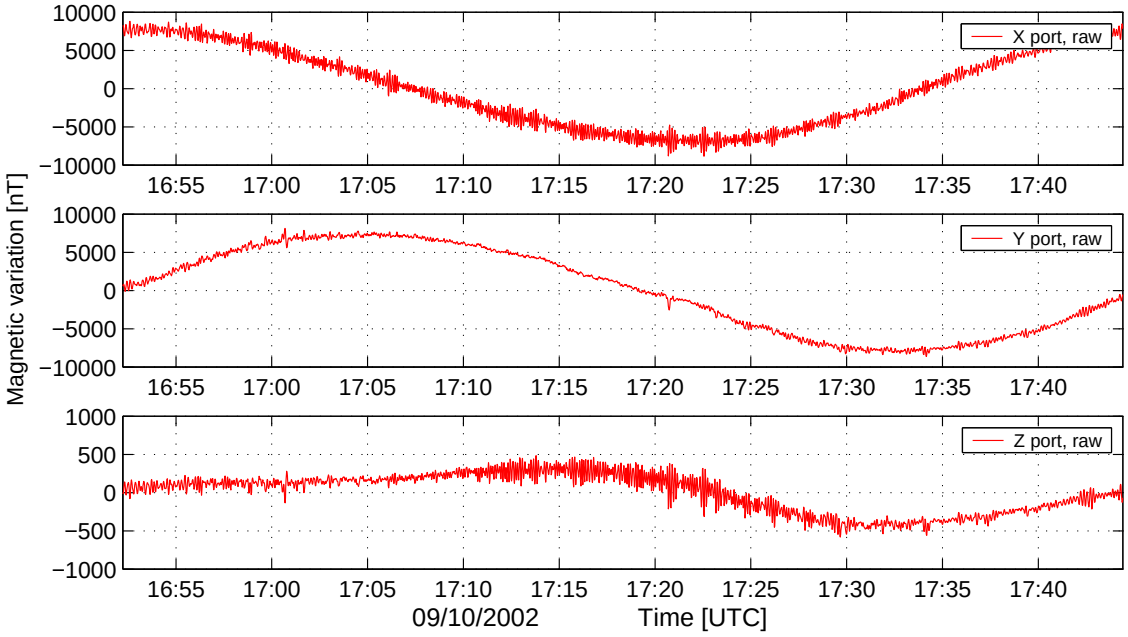

Figure 2.4-13: Raw magnetometer data for the first calibration loop performed on the 9^{th} of October, 2002. Note that the mean of each component has been removed.

The attitude data for the calibration loop show variations in roll and pitch of $\pm 2°$ (Fig. 2.4-14). The roll angle has a long wavelength component which corresponds to wind and swell coming from the southwest. The pitch angle has its maximum variation at a wavelength of about 8 sec, with peak to peak amplitudes of up to 4°. This causes high frequency noise of several 100 nT in the raw magnetic data (Fig. 2.4-13 and table 2.4-T3).

Table 2.4-T3: Improvement ratio (IR), quality ratio (QR) and the according standard deviations for all components of the magnetic field vector and the total magnetic field, for the port sensor during the calibration loop on the 9^{th} of October, 2002. Abbreviation are the same as explained in table 2.4-T2.

Component	HP_{raw} [nT]	HP_{comp} [nT]	IR	IGRF [nT]	LP_{comp} [nT]	QR
X	530.9	46.7	11.4	5.4	42.3	0.1
Y	193.9	48.3	4.0	5.8	47.9	0.1
Z	61.7	22.8	2.7	3.4	15.6	0.2
F	51.5	26.8	1.9	2.7	16.3	0.2

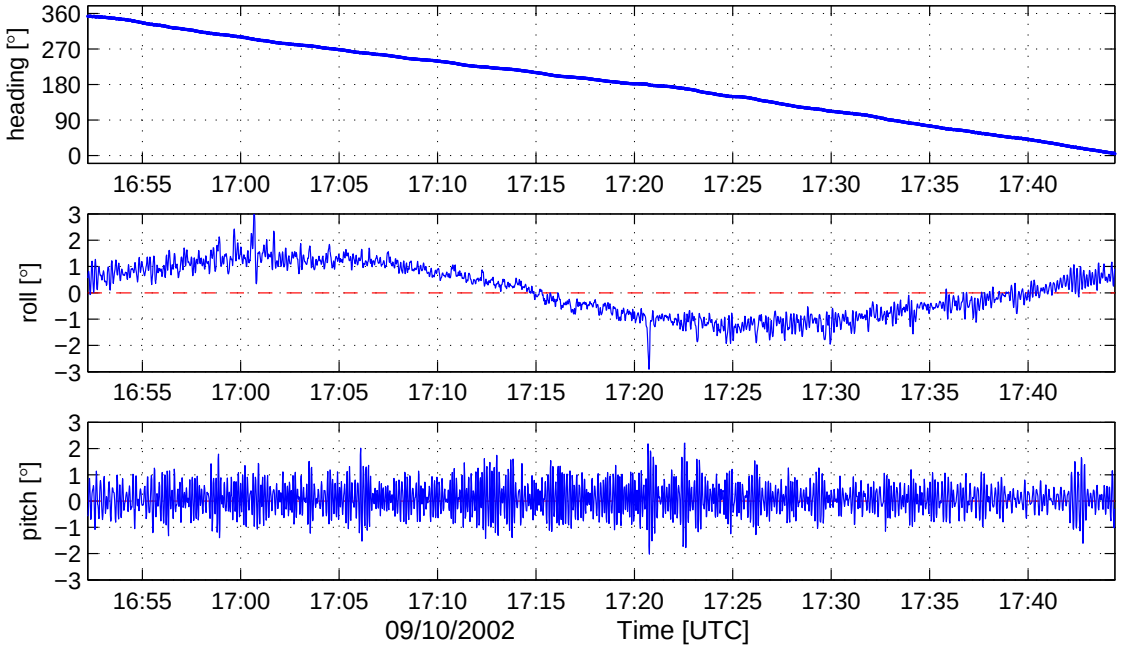

Figure 2.4-14: Attitude data for the calibration loop on the 9^{th} of October, 2002.

After compensation, this can be reduced in the high-frequency domain to less than 50 nT for the horizontal components and less than 25 nT for the vertical component (Fig. 2.4-15 and Table 2.4-T3). In the long wavelength domain, there are residual fields of more than 40 nT in the horizontal component and about 15 nT in the vertical component.

In the filtered total magnetic field data (Fig. 2.4-16), there is a long wavelength component with a maximum amplitude of about 30 nT and a mean variation of less than 20 nT persistent. Without taking into account any daily variations, this

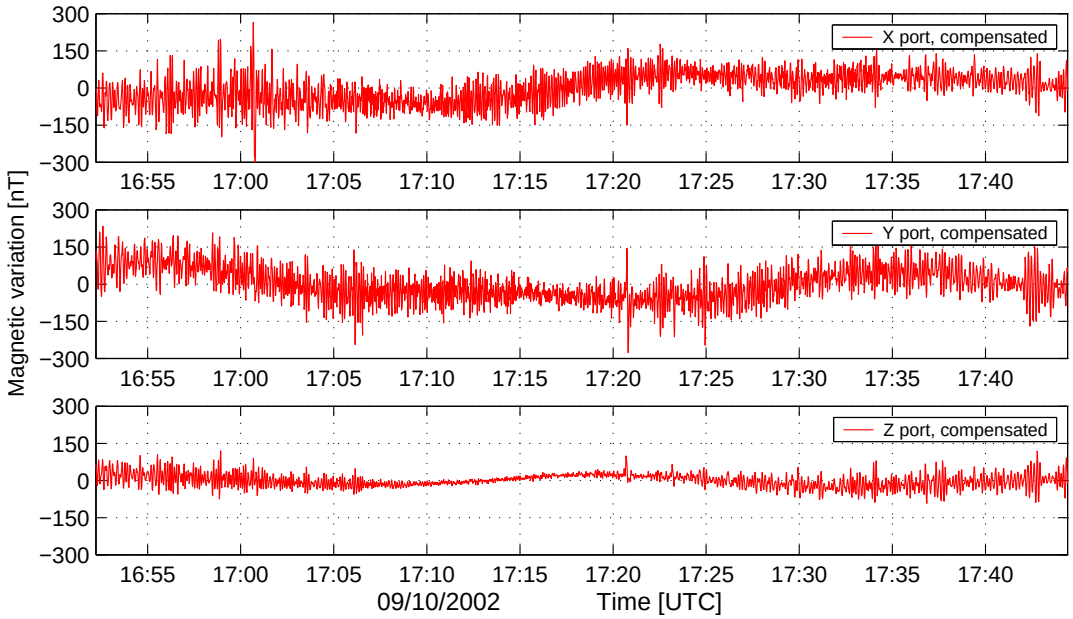

Figure 2.4-15: Compensated magnetic anomaly data for the calibration loop on the 9^{th} of October, 2002. Note that the mean of each component has been removed.

results in a maximum error of 30 nT and a mean accuracy for the compensated total magnetic anomaly field, in moderate seas, of better than 20 nT.

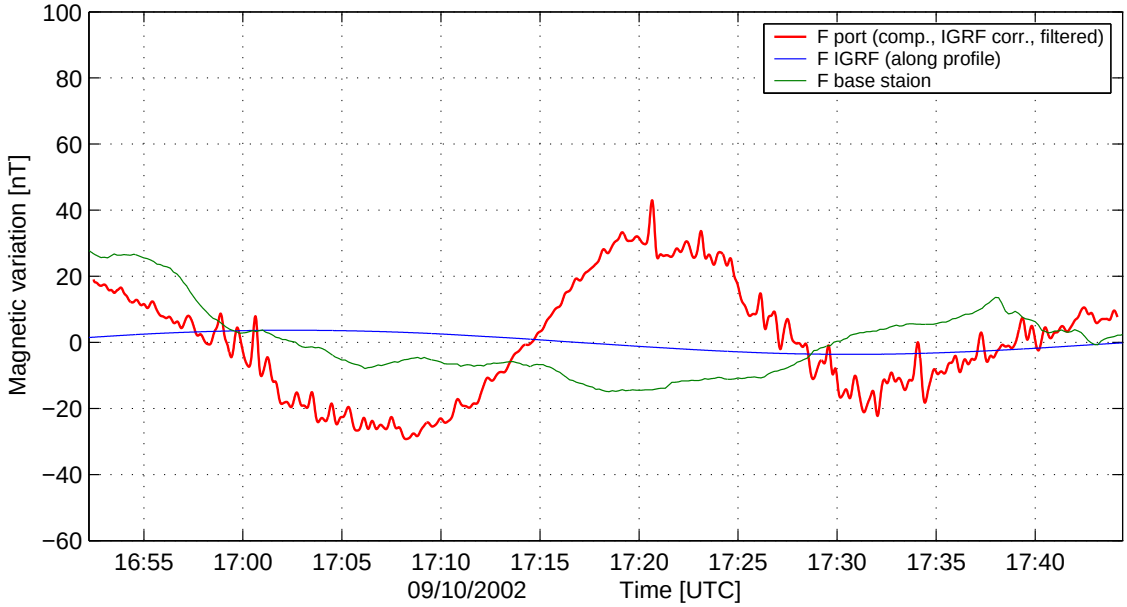

Figure 2.4-16: Compensated, IGRF corrected, and filtered total magnetic anomaly data for the port sensor. Also shown are the base station readings from the nearest base station in NyÅlesund, Svalbard, and the variations of the IGRF calculated along the track.

2.4.7 Comparison of portside and starboard sensor data

The differences between the coefficients for the permanent and induced ship's field, as seen by the port and starboard sensors, were discussed in chapter 2.4.2. The influence of the central mast of the crow's nest on the permanent ship's field at the position of both sensors was explained in detail. Thus, there is a difference in the raw magnetometer data of more than 10000 nT between the cross component of the permanent ship's field between the port and starboard sensor.
Figures 2.4-17 and 2.4-18 show the differences between both sensors for the components of the magnetic field after compensation and for the total-intensity after compensation and filtering. Data from the calibration loops on the 30^{th} of September, 2002, and 9^{th} of October, 2002 are shown as examples for quiet and moderate to rough sea conditions. A detailed description of the two calibration sites was given in the previous chapter (2.4.6). Any constant offset between the data from the two

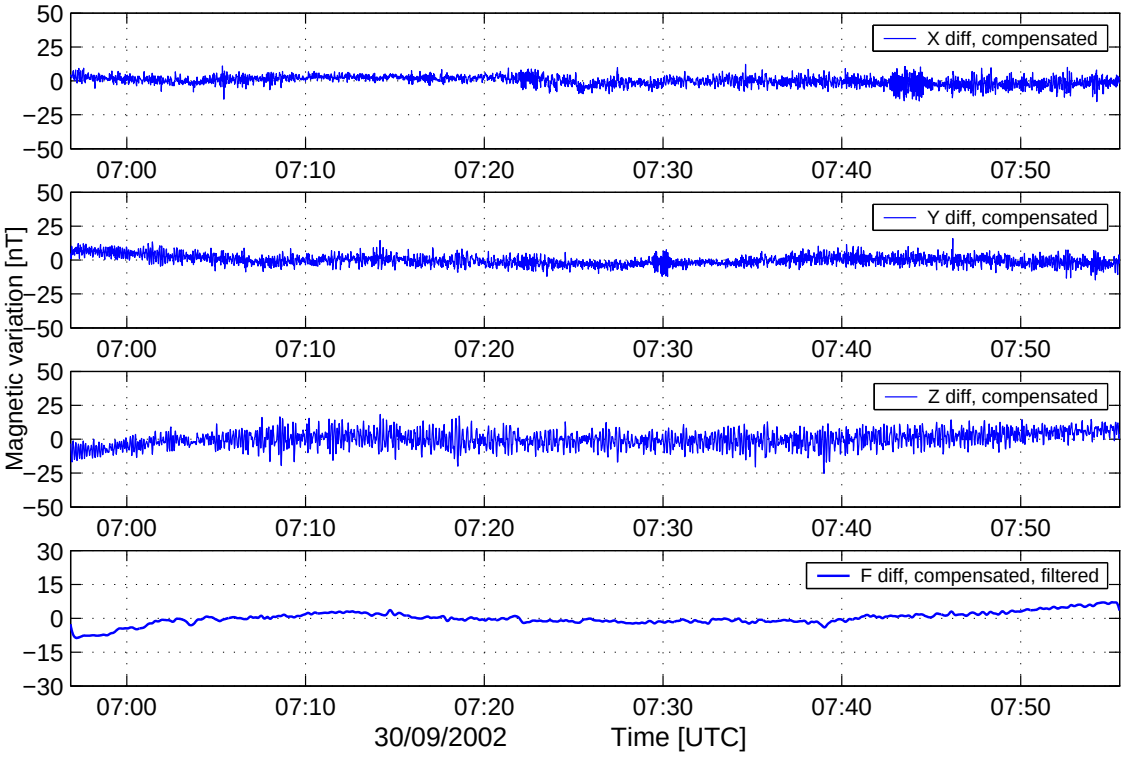

Figure 2.4-17: Differences between the portside and starboard sensors for the calibration loop on the 30^{th} of September, 2002. Note the different scale for the vertical axis of the graph for the filtered total-intensity F.

sensors is below 1 nT in all components of the magnetic field vector and in the total magnetic field. In the high frequency domain, the maximum difference between the two sensors is below 20 nT and the mean variation is below 5 nT, under quiet sea states (Fig. 2.4-17). In moderate sea conditions, the maximum difference reaches

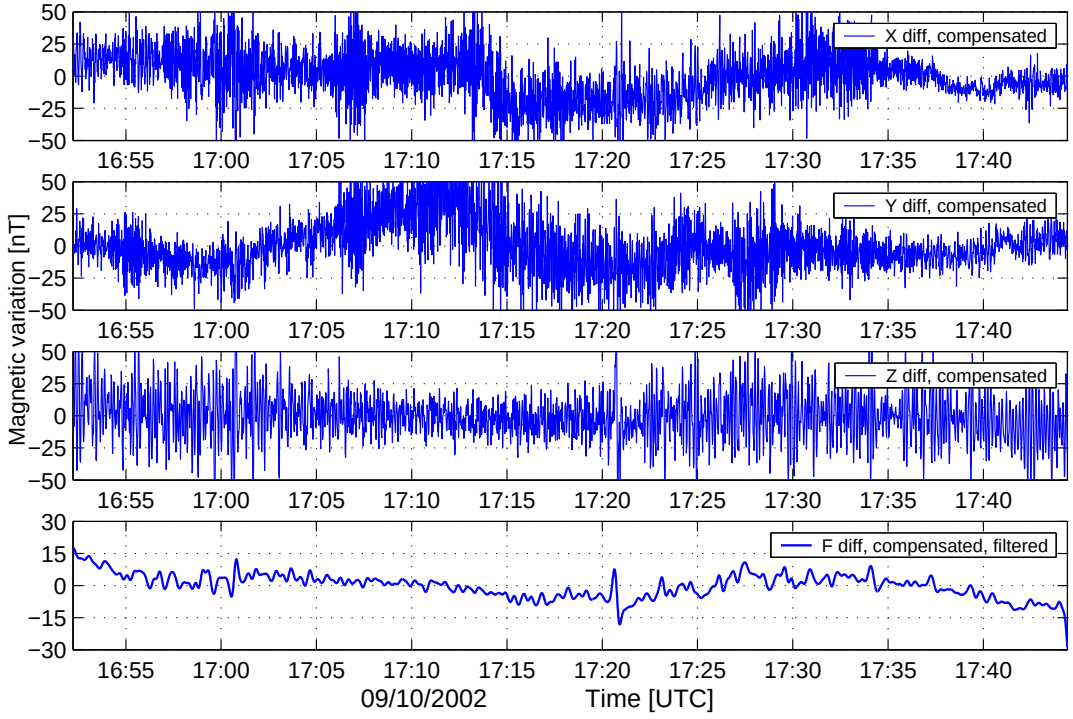

Figure 2.4-18: Differences between the portside and starboard sensors for the calibration loop on the 9^{th} of October, 2002. Note the different scale for the vertical axis of the graph for the filtered total-intensity F.

values of about 50 nT with a mean variation of about 20 nT (Fig. 2.4-18). The difference in the lowpass filtered total magnetic field data has a mean variation of less than 3 nT for quiet conditions and 5.5 nT for moderate conditions.
The accuracy of the sensor system, as estimated in the previous chapter (2.4.6), can be confirmed from these calculated differences between the sensors at different sea states. Thereafter, accuracy of the compensated and filtered total magnetic field signal is better than 15 nT for quiet and better than 30 nT for moderate sea states.

2.4.8 Processing of profile data

Generally, the processing of profile data is the same as for the compensation of calibration loops. The individual steps are listed below:

- In a first step, an appropriate set of coefficients has to be chosen from one of the calibration loops. This is either the loop performed closest in time to the profile data, or any other calibration loop which could produce reasonable compensation results. The greater the time gap between calibration loop and the profile, the larger the possible errors due to changes in the magnetization of the ship, that can result in constant offset shifts.

- The selected coefficients are then applied to the raw data.
- An IGRF correction should be performed to reduce the data to their anomaly value.
- Finally, a lowpass filter is applied to the data to remove high frequency noise. The filter should be adapted to the quality of the data and the speed of the ship.

For the purpose of comparability, in this work, always the same lowpass filter is used. This is a zero-phase, forward-backward, FIR filter (finite impulse response) of order 30 and a cutoff frequency at 0.033 Hz (∼30 sec). The stopband starts at about 0.09 Hz (∼11 sec). By the use of a forward-backward filter, a phase lag of zero is realized since the data are processed in both the forward and reverse directions. This filter is used in order to keep any correlations between filtered magnetometer and raw attitude data. This is of interest, for example if correlations before and after compensation are calculated. Assuming a maximum velocity of 10 kt along the profile, a cutoff frequency of 0.033 Hz (∼30 sec) and a stopband at 0.09 Hz (∼11 sec) corresponds to a filter in the space domain with a cutoff wavelength at ∼154 m and a stop band wavelength of ∼57 m. This means, that at the assumed speed of 10 kt, a horizontal along-track resolution of ∼154 m can be achieved.

Examples of the processing of shipborne magnetic profile data and further estimates of the accuracy and resolution of the magnetometer system are given in chapters 2.5 and 2.6.

2.5 Validation of the magnetometer system using helicopter-borne data

For validation purposes, magnetic anomaly data from helicopter profiles are compared with compensated ship track data which have been conducted in close spatial (and temporal) vicinity to each other. A pair of almost-coincident profiles (max. distance 1.3 km) is the ship track from the 2^{nd} of October, 2002 and a helicopter profile from a different time on the same day (Figures 2.5-1 to 2.5-3). The helicopter magnetic data were acquired with an optically pumped caesium magnetometer towed about 35 m below the helicopter. The flight level was about 100 m above sea level. The ship's track and the helicopter profile are plotted in figure 2.5-1. The attitude data along the ship's track is shown in figure 2.5-2. Moderate to quiet sea conditions were present along the almost perfectly north-south oriented profile. The processed magnetic anomaly data, their difference, and the simultaneous base station readings

from the nearest base station in NyÅlesund, Svalbard (78.92°N, 11.93°W; about 309 km distant) are presented in figure 2.5-3.

For a better correlation, the two profiles have been projected onto a straight line

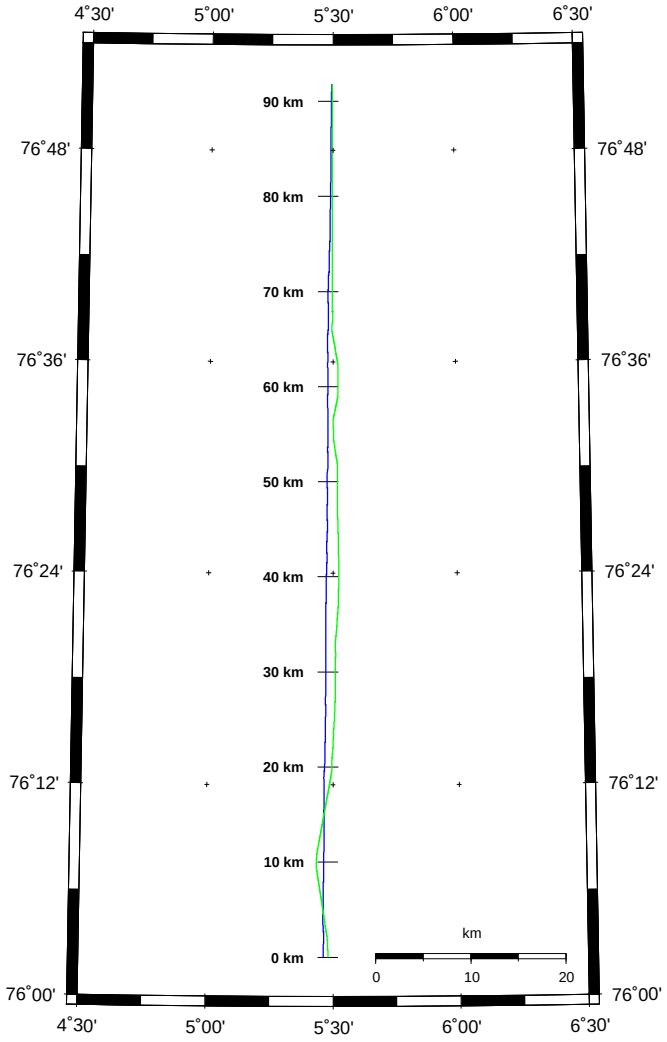

Figure 2.5-1: Helicopter (blue) and RV *Polarstern* (green) track lines on the 2^{nd} of October, 2002. The distance along profile is indicated starting at the southernmost point of the profile.

running between them. This line starts at 5.48°N, 76.04°E and ends at 5.48°N, 76.86°E, having an overall length of about 91.84 km. Both tracks have been sampled every 10 m along this profile using a linear interpolation scheme. At a profile speed of 10 kt, this means a reduction in the ship's data points by about one half, and for the helicopter operating at a speed of about 120 km/h this corresponds to an interpolation from 33 m horizontal spacing between data points to 10 m.

The helicopter-borne data are despiked and have been corrected for the IGRF. The shipborne data were compensated using the coefficients from the first calibration

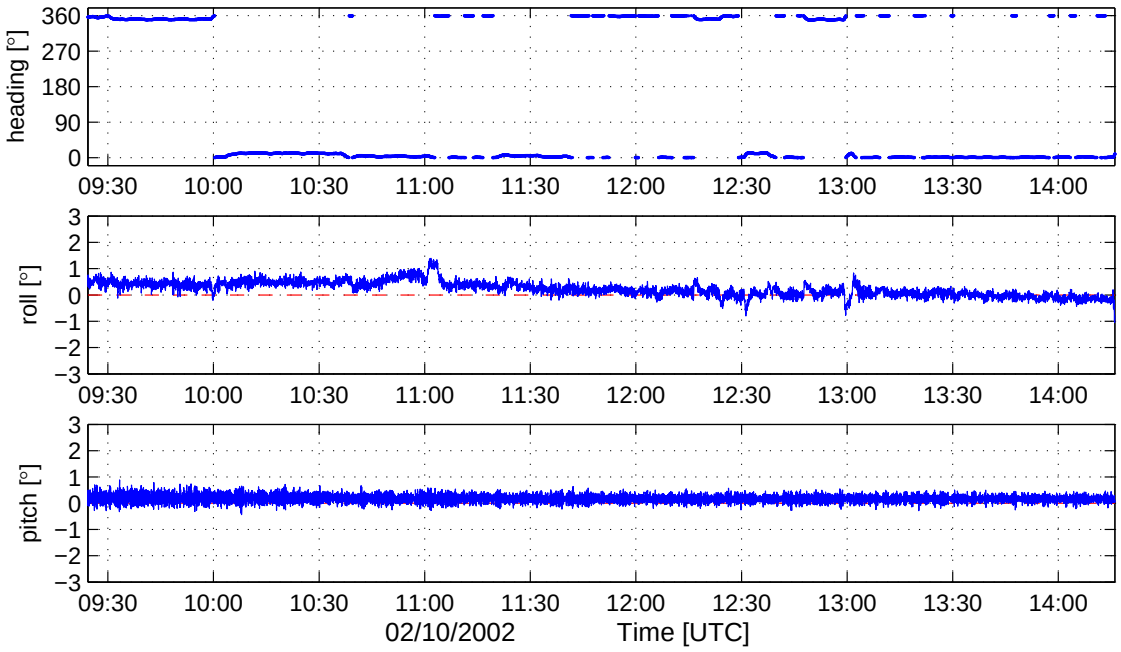

Figure 2.5-2: Attitude data along the selected ship track shown in figure 2.5-1.

loop from the 30^{th} of September, 2002. The IGRF was removed from the compensated data, and the lowpass filter was applied last (Chapter 2.4.8). Finally, the two profiles are corrected for their mean values and any residual linear trend. This kind of correction has been done in spite of any diurnal correction which would considerably influence the final result, as can be seen from the lowermost graph in figure 2.5-3. In this way, for the helicopter profile starting at 08:38 UTC and ending at 09:16 UTC an offset of 48.7 nT and a linear trend of 3.0 nT was removed. For the shipborne data starting at 09:24 UTC and ending at 14:16 UTC an offset of -219.2 nT and a linear trend of -37.1 nT was removed. While the helicopter flight only had a duration of 38 minutes the data along the ship track were acquired during 4 hours and 52 minutes gving rise to the assumption of larger daily variations in the ship data.

Comparison between the two profiles yields a close correlation across their entire length. The maximum difference between the track data is always less than 50 nT having a standard deviation of 21.5 nT. Looking at the diurnal variations recorded at the same base station but at different times, a maximum difference of nearly 200 nT between the recordings during the two profiles can be seen at around 20 km in the lowermost graph in figure 2.5-3. However, a difference of less than 50 nT exists at this position in the profile data (Fig. 2.5-3). From this it is concluded that the diurnal variations recorded at NyÅlesund cannot be applied to the track data since there seems to be no clear correlation between the variations recorded at both

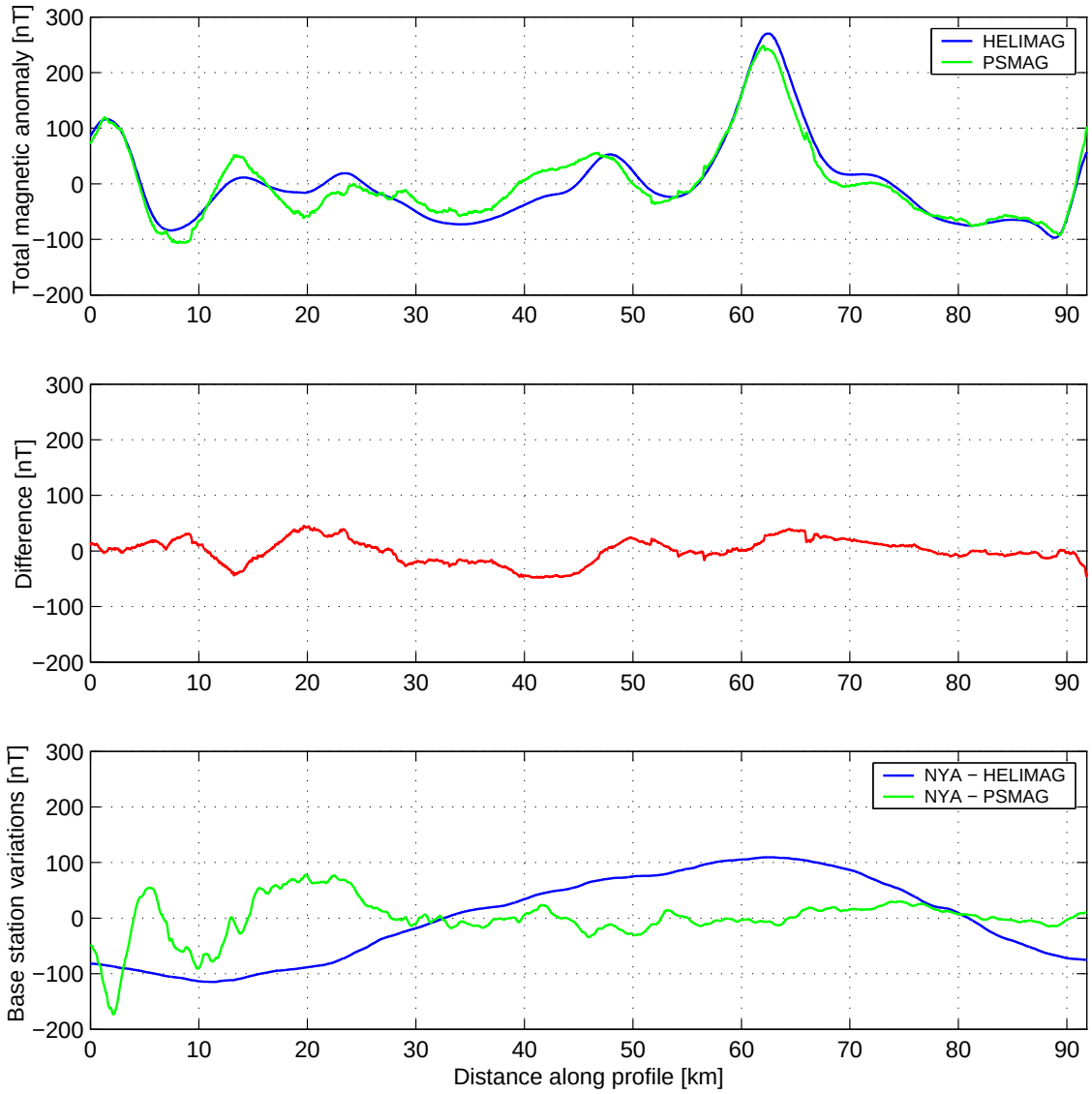

Figure 2.5-3: Comparison between processed total magnetic field data from helicopter-borne and shipborne track lines. The upper figure shows the total magnetic anomaly data. Below, the difference between HELIMAG and PSMAG data is shown and in the lower part of the figure the base station readings from NyÅlesund for the time of both profiles are shown.

sites even during magnetically disturbed days. Probably amplitudes over the sea are strongly reduced compared to the land station due to the greater depth to any magnetic basement or inducing rocks.

Although the data have been projected onto a common line, there still seems to be a spatial offset of about 0.5 - 1 km along the profile between both recordings between 45 km and 75 km, as seen in the uppermost graph in figure 2.5-3. Taking into account this displacement, and possible residual fields due to uncompensated diurnal variations, the mean difference between helicopter-borne and shipborne mag-

netometer data can be estimated to less than 20 nT along this 90 km long profile.

Assuming that the error in the relative amplitudes recorded by the caesium sensor is less than 1 nT (Scintrex Inc.), it can be concluded that amplitudes of anomalies recorded by the ship-mounted magnetometer system are represented with a mean accuracy of better than 20 nT at a horizontal resolution of 150 m at moderate to quiet sea conditions.

2.6 Compilation of a magnetic anomaly map

In this chapter, a case study for compiling a magnetic anomaly map from shipborne magnetometer data is presented for a small survey pattern conducted during the ARK-XVIII/2 expedition southwest of Svalbard (Fig. 2.6-1a). For validation, the compiled magnetic anomaly map is compared with high-resolution helicopter-borne magnetic anomaly data and a regional magnetic anomaly compilation for the Arctic Ocean (Verhoef et al., 1996).

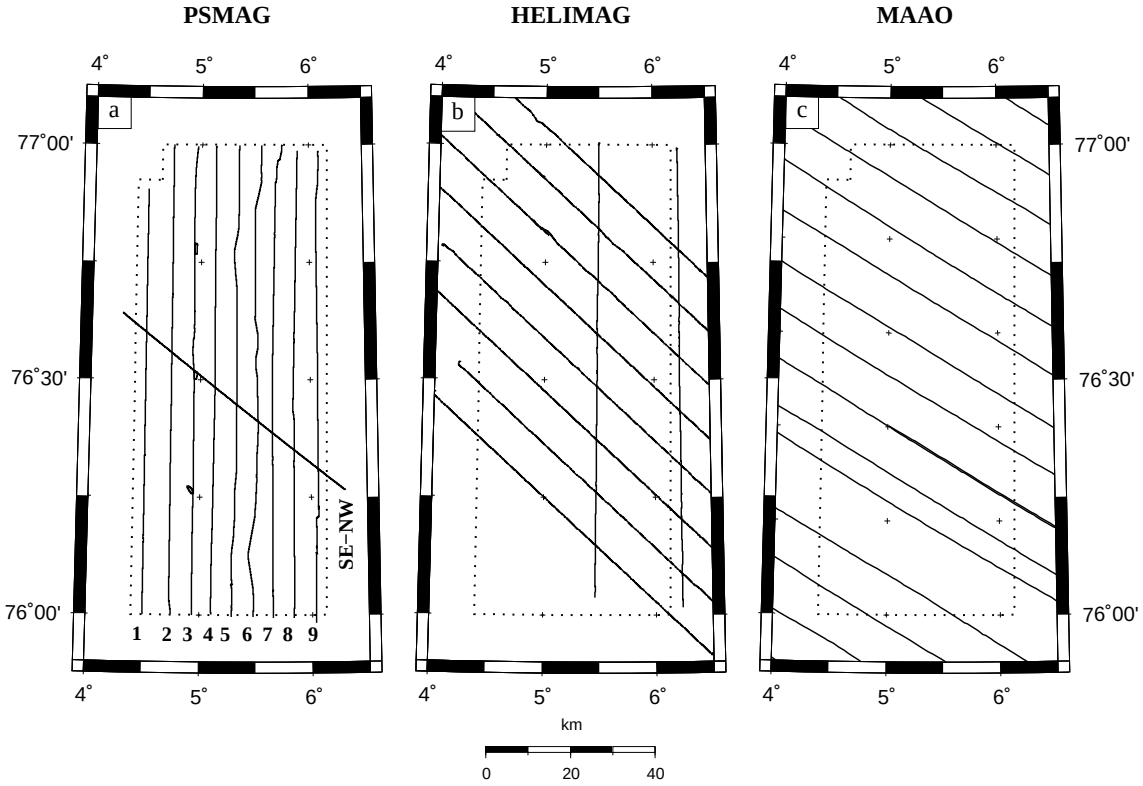

Figure 2.6-1: a) Ship track lines for small scale survey area during ARK-XVIII/2. Numbers indicate arbitrary labels to the lines. b) Helicopter profiles for airborne survey during ARK-XVIII/2. c) Flight lines used for the compilation of the magnetic anomaly map of the Arctic Ocean (Verhoef et al., 1996) .

The track lines of the ship's survey pattern are shown in figure 2.6-1a and can be identified on the overview map in figure 2.4-2. The selected data set starts on the 30^{th} of September, 2002 (20:57:11 UTC) and ends on the 4^{th} of October, 2002 (00:58:05 UTC), covering a time span of about 68 hours with a break of about 10 hours and an overall track length of 1220 km. An area of 5000 km^2 was covered with a line spacing between 4 to 6 km.

The raw magnetometer data were compensated with the coefficients from the calibration loop on the 30^{th} of October, 2002. A correction for the IGRF was applied to the compensated data. In a next step, the data were filtered to remove any remaining high frequency noise using the same filter as presented in chapter 2.4.8. Since this data set was acquired even during local night time, a diurnal correction was applied to the data in order to remove at least the long-wavelength diurnal variation. Recordings from the NyÅlesund Observatory, Svalbard (in about 300 km distance) were used as base station data. This data set was filtered using a forward-backward FIR filter with a cutoff at 2000 sec and a length of 3600 sec, in order to extract only the long-wavelength component of the daily variations. The filtered base station data were then removed from the compensated total-intensity data. Finally, any remaining mean value or trend was removed from the daily corrected data.

The raw and filtered base station data, together with the compensated and filtered total-intensity data of the port sensor, are shown in figures 2.6-2 and 2.6-3. The data of the north-south oriented lines are plotted with respect to their corresponding distance from the southernmost point (about 76°N). The lines are numbered from 1 to 9, starting with 1 in the west. The line labelled SE-NW corresponds to the southeast-northwest directed line crossing all other profiles.

To estimate the consistency of the data set, a crossover analysis is made on the processed ship track data. To do this, 14 cross points between the southeast-northwest directed line and the north-south directed ones are evaluated (Fig. 2.6-1a). The mean absolute cross point error is about 33.1 nT, with a variation of 30.1 nT. Without taking the absolute value, the mean cross point error is about 11.4 nT with a standard deviation of 44.2 nT. Taking into account the problem of remaining uncorrected daily variations, and the fact that some of the lines were acquired also during local night time hours and severe magnetic variations, the survey data display good self-consistency. No adjustment of these cross point errors was made for further processing and compilation of the magnetic anomaly map.

Using these data, a magnetic anomaly grid was calculated on 2×2 km cells using a

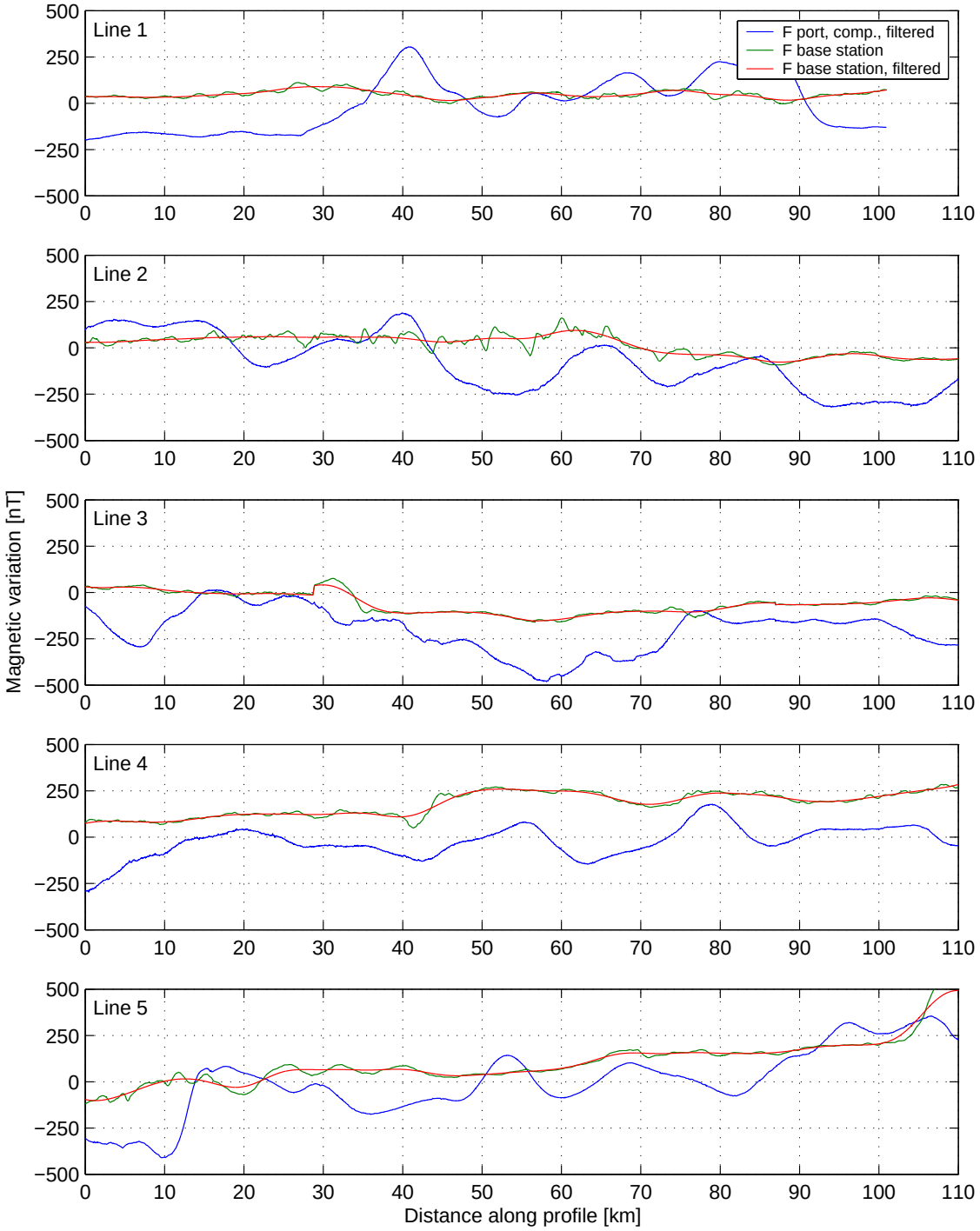

Figure 2.6-2: Compensated and filtered total magnetic intensity as calculated for the port sensor along the profile. The labels refer to the numbers in figure 2.6-1a. Additionally, the base station recordings at the NyÅlesund Observatory, Svalbard are shown before and after lowpass filtering.

minimum curvature algorithm (Smith and Wessel, 1990). This was interpolated to 0.5×0.5 km cell size for a better visual effect (Fig. 2.6-1a).

This magnetic anomaly grid is compared with grids based on helicopter-borne

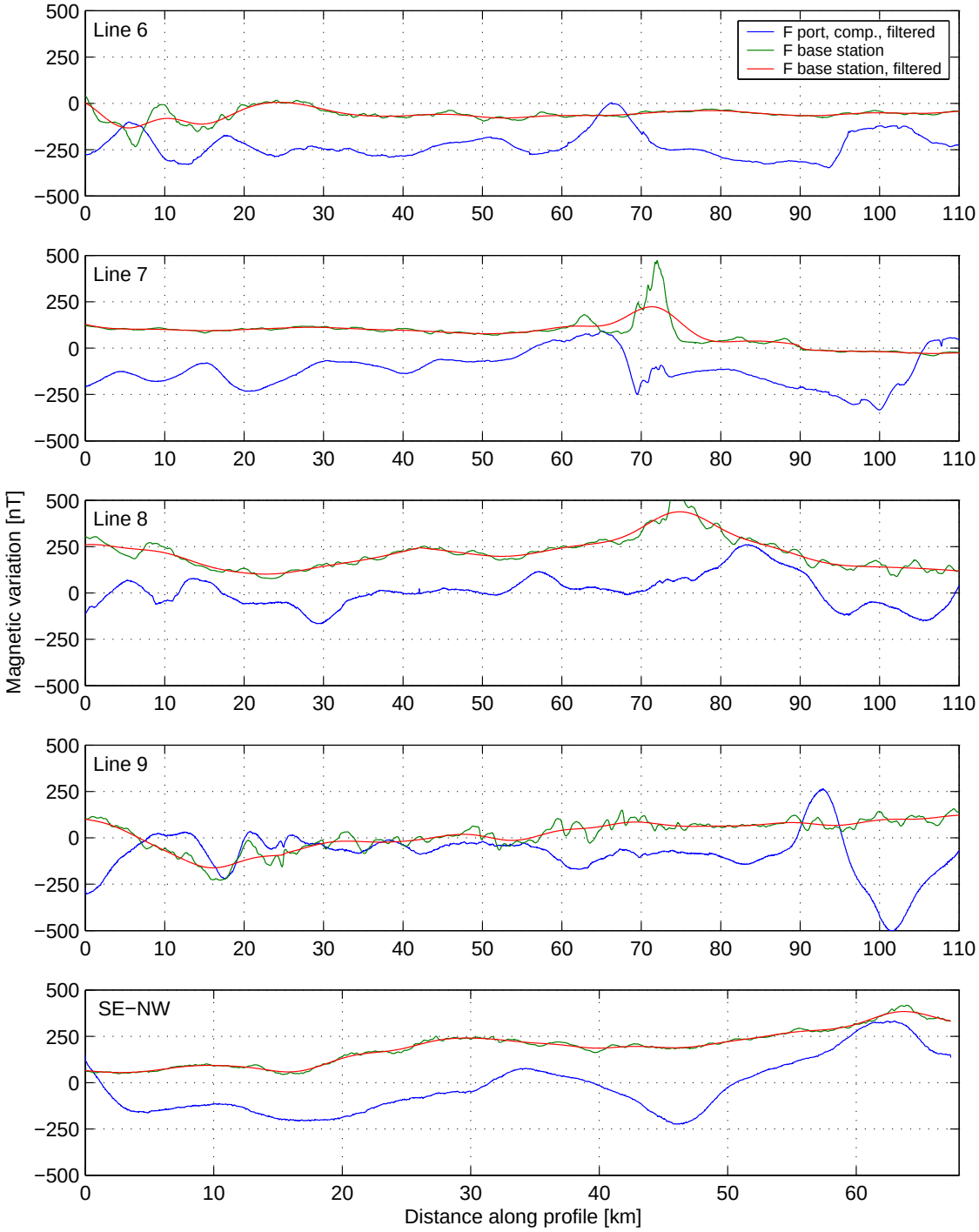

Figure 2.6-3: Compensated and filtered total magnetic intensity as calculated for the port sensor along the profile. The labels refer to the numbers in figure 2.6-1a. Additionally, the base station recordings at the NyÅlesund Observatory, Svalbard are shown before and after lowpass filtering.

data and data from a regional magnetic anomaly compilation for the Arctic Ocean (Verhoef et al., 1996) (here called MAAO - Magnetic Anomaly compilation for the Arctic Ocean).

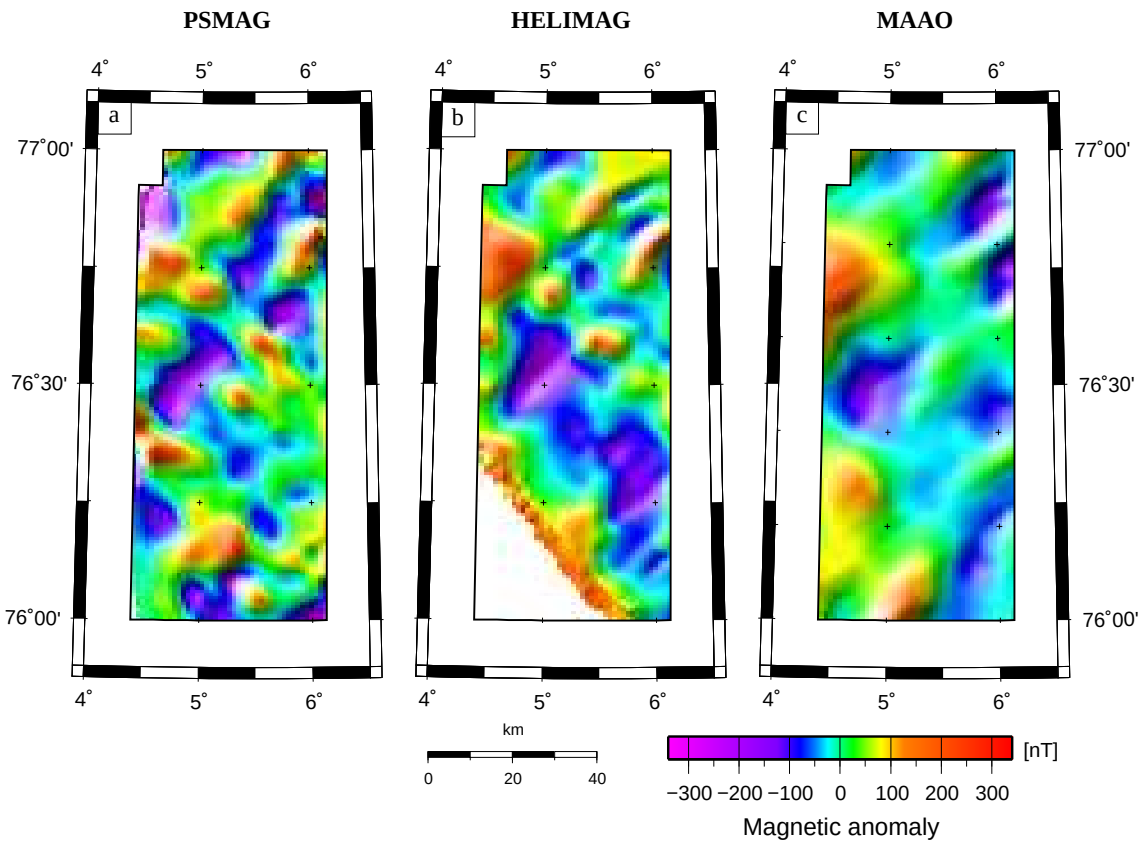

Figure 2.6-4: Magnetic anomaly grids compiled from a) shipborne magnetic anomaly data, b) helicopter-borne magnetic anomaly data and c) a regional magnetic anomaly compilation for the Arctic Ocean (Verhoef et al, 1996). See the text for processing details.

The helicopter-borne data were acquired during the same expedition as the shipborne data. The specifications for data acquisition are the same as presented in chapter 2.5. The profiles used to compile the helicopter based magnetic anomaly grid are shown in figure 2.6-1b. Their spacing varies between 9 and 10 km. Adjacent data points have a spacing of about 33 m, and the profiles are flown 150 m above sea level. The gridding was performed with the same parameters as for the shipborne data (Fig. 2.6-4b).

The MAAO compilation was originally calculated on a grid with a cell size of 5×5 km but, for the purpose of comparison, the data were re-gridded to 2×2 km and the grid interpolated to 0.5×0.5 km cells (Fig. 2.6-4c). The data used for the compilation of the original MAAO grid is shown in figure 2.6-1c. The profile data were acquired in 1972 as part of various aeromagnetic projects led by the US NAVY (Naval Research Laboratory) with a line spacing of 7.5 km and a mean altitude of about 300 m (Verhoef et al. (1996) and references therein). Adjacent data points along profile have a

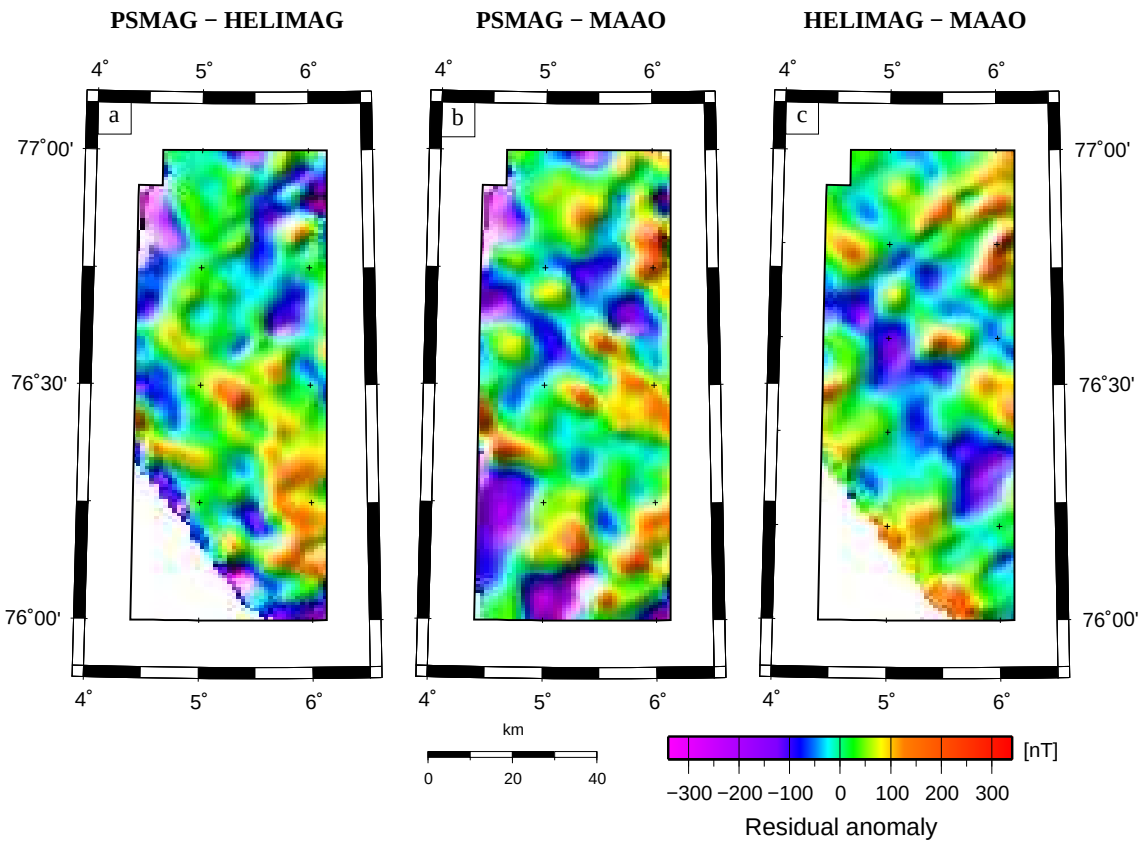

Figure 2.6-5: Residual magnetic anomaly grids after removing a) the helicopter-borne data from the shipborne grid, b) the MAAO data from the shipborne grid and c) the MAAO data from the helicopter grid. See the text for details.

spacing of about 563 m.

Figure 2.6-5 shows the residual field calculated from the difference of the grids presented in figure 2.6-4. Figure 2.6-5a shows the differences between shipborne and helicopter-borne anomaly grids, figure 2.6-5b the differences between the shipborne and MAAO anomaly grids, and figure 2.6-5c the differences between helicopter-borne and MAAO anomaly grids. Note that the same color palette table is applied to all the grids in figures 2.6-4 and 2.6-5.

Looking at the long/intermediate wavelength component of the magnetic anomalies in the grids in figure 2.6-4, some common features are immediately apparent. There is a long positive anomaly present in the northwestern part of the grid striking from southwest to northeast. Additionally, there are several smaller southwest-northeast striking anomalies visible in the northern part of all the three grids. In the residual anomaly grids in figure 2.6-5, there are no large scale high amplitude differences visible. This means that no large remaining offsets or drifts are present in the grids.

Due to the different spatial distribution of data points, the shipborne anomaly grid has the highest resolution of the three (Fig. 2.6-4). The spacing between adjacent data points along the profiles of the ship magnetic data is about 5 m, compared to 33 m for the helicopter-borne and 563 m for the MAAO data set. Accordingly, many of the short wavelength differences between the shipborne data grid and the MAAO grid result from the different spatial distribution of the data points (Fig. 2.6-5b). Similarly, this effect is evident in the difference between shipborne and helicopter-borne data in figure 2.6-5a.
Furthermore, in the northern and eastern parts of the survey area, a number of positive anomalies appear in the differences between the shipborne and MAAO data grids (Fig. 2.6-5b), and the helicopter data grid and the MAAO data grid (Fig. 2.6-5c). This again states the fact that the different spatial distribution of the data sets is responsible for the short wavelength amplitudes present in figure 2.6-5b.
The mean variations (standard deviations) of the residual anomaly grids (Fig. 2.6-5) listed in table 2.6-T1. The standard deviations are grouped at around 77 nT with a

Table 2.6-T1: Standard deviations (std).

Difference	std [nT]
PSMAG - HELIMAG	77
PSMAG - MAAO	90
HELIMAG - MAAO	66

variation of about 12 nT. The generally higher values for the differences including the shipborne magnetics (PSMAG) may result from the higher spatial resolution of this data set.

Finally, from the comparison of the three magnetic anomaly grids, it is concluded that the magnetic anomaly map calculated from the shipborne data is, in general, similar to that calculated from helicopter-borne data and a reginal magnetic anomaly compilation, but has the advantage of a better horizontal along track resolution.

2.7 Summary

A magnetometer system has been installed onboard the German icebreaker and research vessel RV *Polarstern* in order to continuously record the variations of the geomagnetic field during scientific expeditions into the polar regions of both hemispheres.

The vector magnetic field is measured using a three-component fluxgate sensor system. The ship's position and attitude data are simultaneously recorded with a high precision inertial navigation system in order to correct the measured data for the ship's interfering field and calculate the vector of the compensated magnetic field in a geodetic coordinated system.

A processing procedure for the compensation and evaluation of such shipborne magnetometer data has been presented and the accuracy of the sensor system was estimated. A magnetic anomaly map has been generated and compared with data grids, calculated from other sources, to demonstrate the capabilities of the new sensor system.

Raw magnetic data acquired onboard the ship have to be corrected for the ship's interfering field. This correction is applied by using a set of compensation coefficients that describe the ship's interfering field. Calibration loops, with a radius of about 1 nm, carried out at a speed of 5-7 kt, are performed in order to determine the coefficients. Although there are large variations in the values of the coefficients calculated from several different loops, their relative sign and size can be in general correlated with the ship's geometry. The vector of the geomagnetic field along the ship's track is calculated by inversion from the measured vector magnetic data, applying the compensation coefficients of a nearby calibration loop. High frequency noise that persists in the compensated magnetic anomaly data is removed by the use of a zero-phase, forward-backward, finite impulse response lowpass filter of order 30 and with a cutoff frequency at 0.033 Hz (30 sec).

The accuracy of the magnetometer system depends on the state of sea during which the calibration loop data and profile data were acquired, as well as on the applied filters. Under quiet sea conditions, compensated and filtered magnetic anomaly data have a maximum error of about 20 nT, while the maximum error of data acquired under moderate to rough sea conditions is less than 30 nT. Horizontal resolution in the data is estimated to be about 150 m, assuming a ship speed of 10 kt. This is supported by comparing shipborne and helicopter-borne magnetic anomaly data measured along almost-coincident profiles.

The estimated accuracy of about 20 nT at a horizontal resolution of 150 m is sufficient for the identification of seafloor spreading anomalies with amplitudes of less than 50 nT and widths of less than 0.5 km. Under the scope of continuous measurements, this opens up a wide range of applications for the ship-mounted magnetometer system as installed onboard RV *Polarstern*. Besides the identification of seafloor spreading anomalies in dedicated survey areas, measurements made on transit can significantly contribute to existing data bases and yield valuable information on the physical properties of the ocean crust. Furthermore, helicopter-borne surveys carried out in remote areas can be supported by shipborne magnetometer data, filling gaps in crucial flight lines and/or providing magnetic base station data.

However, improvements to the ship-mounted magnetometer system are suggested for the future:

- It is proposed to set up the two magnetometer sensors longitudinally in fore and aft direction to improve the accuracy and spatial resolution of the sensor system. This arrangement permits the elimination of daily variations and thus significantly enhances the accuracy of the compensated anomaly data. By interpreting the horizontal gradient between the two sensors small spatial anomalies can be located with higher confidence.

- High frequency noise might be significantly reduced if a better correlation between the ship's attitude data and the magnetometer data can be provided. The installation of an attitude sensor system in close vicinity to the magnetometer sensors is hence suggested. However, the availability of high precision attitude sensor systems of considerable size and costs is limited.

- Finally, semipermanent magnetism should be investigated in greater detail to reduce errors due to course changes and to better describe the ship's interfering field.

3 A detailed model for the Mesozoic break-up of Gondwana in the South Atlantic region

The drift history of the continents and continental fragments in the South Atlantic region is well constrained for ages younger than Late Cretaceous (< 83 Ma). However, this is not the case for the early stages of Gondwana break-up between Africa, Antarctica, and South America during Jurassic and Early Cretaceous times. A key to this problem is the opening history of the Weddell Sea in the southwestern corner of Gondwana. Until recently, no clear seafloor spreading anomalies could be identified close to the continental margin of western Dronning Maud Land bordering the Weddell Sea to the east, where the separation between South America and Antarctica took place. But it is this kind of magnetic (and gravimetric) anomaly data that yields crucial information about the age and structure of the ocean floor created during the opening of the ocean basin.

Intensive aeromagnetic surveys were carried out onshore Dronning Maud Land and across the Antarctic Peninsula into the western Weddell Sea by various nations in the last 30 years. But still only sparsely distributed ship track lines existed in the regions of the eastern Weddell Sea, Lazarev Sea, and Riiser-Larsen Sea (Fig. 3.0-1). To fill this gap and to unravel the processes involved in the disintergration of Gondwana, a challenging aeromagnetic and gravity mapping project has been set up by the Alfred-Wegener-Institute in 1996. Within the next six Antarctic summer seasons an area of 680000 km^2 has been covered along the west coast of Dronning Maud Land by high resolution aeromagnetic flight campaigns having an average line spacing of about 9 km. This project was named the East Antarctic Margin Aeromagnetic and Gravity Experiment (EMAGE).

Results of this extensive aerogeophysical dataset were published by Jokat et al. (2003b) after the completion of the EMAGE project. For the first time, a complete set of seafloor spreading anomalies could be identified and precisely dated off the west coast of Dronning Maud Land. These anomalies were formed when southernmost South America (the Falkland Plateau) cleared the coast of East Antarctica in Early Cretaceous times. Together with another aeromagnetic dataset from the Riiser-Larsen Sea, covering an area where once Africa and Antarctica started to separate, these authors present a new model for the early break-up of Gondwana.

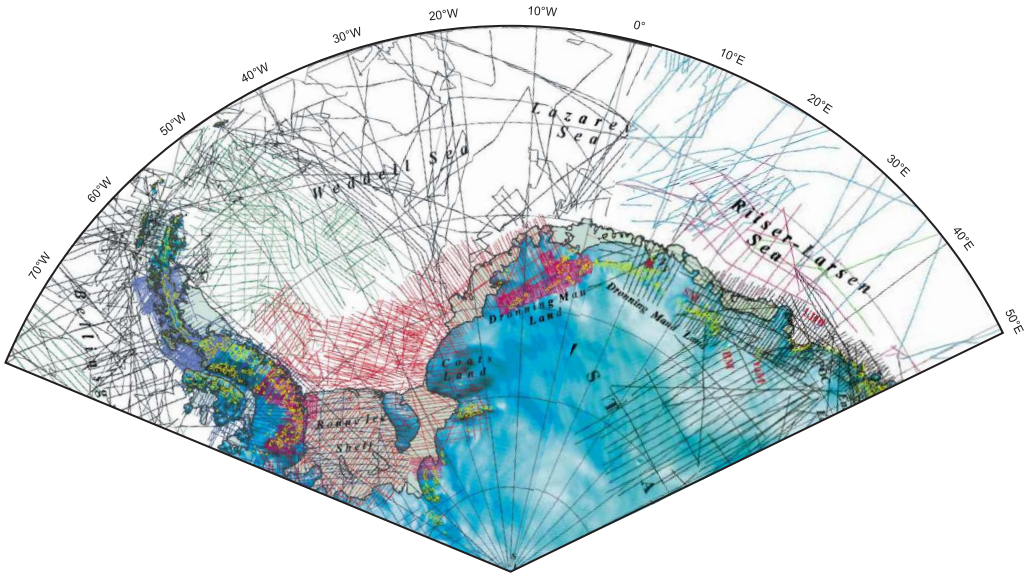

Figure 3.0-1: Previous database of magnetic track data in the Weddell Sea and along the coast of East Antarctica. Note sparsely distributed data between 25°W and 50°E in the eastern Weddell Sea, the Lazarev Sea, and the Riiser-Larsen Sea. Compilation of magnetic data combined under the Antarctic Digital Magnetic Anomaly Project (ADMAP). Left side of figure from 70°W to 0° modified after Golynsky et al. (2002a) and right side of figure from 0° to 50°E modified after Golynsky et al. (2002b). Red lines in the southern Weddell Sea are from Russian regional aeromagnetic projects (1976-1989), green lines in the western Weddell Sea result from an collaborative effort of the United States, Argenitna and Chile between 1977 and 1979, all other lines in the Weddell Sea, Lazarev Sea and the Riiser-Larsen Sea are ship track data of various nations.

New rotation parameters are presented for the Africa-Antarctica spreading system describing the movements between these two continents between 160 Ma and 80 Ma. For the eastern Weddell Sea, the propagation of a rift along the west coast of Dronning Maud Land in northeasterly direction is proposed for magnetic chrons M19N to M17N. However, no precise age and position are given for the time and location of the onset of basin formation in the Weddell Sea. Furthermore, in the model presented by Jokat et al. (2003b), the Antarctic Peninsula is fixed with respect to East Antarctica excluding any stretching and extensions in the Filchner-Ronne Shelf. Similarly, no extensions in the Falkland Plateau basin are included. This means that no details about the tectonic settings in the region enclosing the Weddell Sea basin were included in the model. The paper concentrated only on the areas where new magnetic data were gathered.

In this thesis, a refined model for the break-up of Gondwana is established, which also accounts for the movements of the continents and continental blocks in the southwestern corner of Gondwana and provides a newly defined set of rotation parameters for the reconstruction of the break-up process in the South Atlantic region from 167 Ma to 83 Ma. Complementary to the paper of Jokat et al. (2003b), a new

model for the spreading system in the Weddell Sea is calculated, combining age constraints from the EMAGE dataset with other published profile data from the central and southwestern Weddell Sea. Since only one side of this spreading system still exists, the calculation of the rotation parameters is done by step-by-step rotation back in time of the well known magnetic anomaly C34 (83 Ma). Together with a great amount of additional geological and geophysical data from the ocean basins in the South Atlantic region a, consistend new model for the break-up of Gondwana is calculated. This model provides strong constraints on the early movements between South America, the Antarctic Peninsula and East Antarctica in the southwestern corner of Gondwana including extensional forces in the Filchner-Ronne Shelf and the Falkland Plateau. The timing for the opening of the Weddell Sea is reviewed to an age of 147 Ma, which is about 15-20 million years later than previously published in other models. The combination of the newly defined rotation parameters with recently published finite rotations for the northern Natal Valley results in a verified model for the development of the Mozambique Ridge between Africa and Antarctica, suggesting an opening of the Lazarev Sea at about 122 Ma.

As part of this thesis, the compilation of the aeromagnetic data from the six EMAGE campaigns as well as the grid preparation were contributed to the paper of Jokat et al. (2003b). These parts of data processing are also presented in this thesis in chapter 3.3.1. Additionally, the preparation of the reconstructions in the paper of Jokat et al. (2003b) (Fig. 7a-d) including data selection, digitizing of line data, rotation and layout were provided by the author of this thesis.

The model presented in the paper of Jokat et al. (2003b) was prepared using the ATLAS software distributed by Cambridge Paleomap Software Ltd. (CPSL). A set of finite rotations, shipped with the software package, was adjusted and modified by one of the co-authors (T. Boebel) to fit the new constraints from the AFR-ANT spreading system. However, this software turned out to be not the appropriate tool for the calculation of a spreading model for the Weddell Sea. Instead, a suite of MATLAB (The Mathworks Inc.) programs has been developed that fits the following tasks:

- calculation of any kind of rotation parameters given a set of poles and angles describing relative motions between continental blocks at specified times,
- calculation of rotation parameters if magnetic anomaly data of only one side of a spreading system exist,
- easy rotation of line data with GMT (Generic Mapping Tools) compatible (ASCII) in- and output,
- high resolution graphical output,

- creation of animated sequences (movies) in common formats,
- plattform independent (UNIX, PC, Macintosh);

Besides its computational and graphical strength, MATLAB also offers a highly programmable, machine independent platform that can be used for the programming of batch jobs and scripts to facilitate calculations like those mentioned above. No ready-to-use program was available at the time that could be used for these purposes, instead.

In the following, a short description of the content of the various chapters of this part of the thesis is given.
After an introduction to the different and differing models for the Mesozoic break-up of Gondwana in the Weddell Sea basin (Chapter 3.1) an introduction to the geological and tectonic settings of the Weddell Sea basin is given in chapter 3.2. Data processing is explained in chapter 3.3 and the EMAGE aeromagnetic data base and resulting magnetic anomaly grid are presented in chapter 3.3.1. This data set is combined with additional airborne and shipborne magnetic anomaly data from other national and international expeditions in the central and western Weddell Sea in chapter 3.3.2. The magnetic anomalies in this extensive data set are identified in chapter 3.3.2. Using the anomaly identifications for the Weddell Sea and additional data from other ocean basins and continents, a detailed model for the break-up of Gondwana is calculated. The method for determining this model is described in chapter 3.3.3. In chapter 3.4, the final Gondwana break-up model is presented, followed by a detailed discussion of its consequences in chapter 3.5. Finally, the consequences of the new model are summarized in chapter 3.6.

3.1 Gondwana break-up models

Precise knowledge of plate motions in the region of the South Atlantic Ocean (Fig. 3.1-1) during the early break-up of Gondwana is essential to describe Mesozoic changes in paleoceanography and terrestrial environment (Scotese and Sager, 1989; Lawver et al., 1992). The opening of gateways between continents has significant influences on basin formation and their depsositional environment (Macdonald et al., 2003).

Detailed reconstructions for the opening of the South Atlantic Ocean between South America (SAM) and Africa (AFR) were already presented e.g. by Martin et al. (1982) and Nürnberg and Müller (1991) and have been the subject to many other studies in the following years (e.g. Lawver et al. (1998)). Early reconstructions of the spreading regime between Africa and Antarctica (ANT) were provided e.g. by

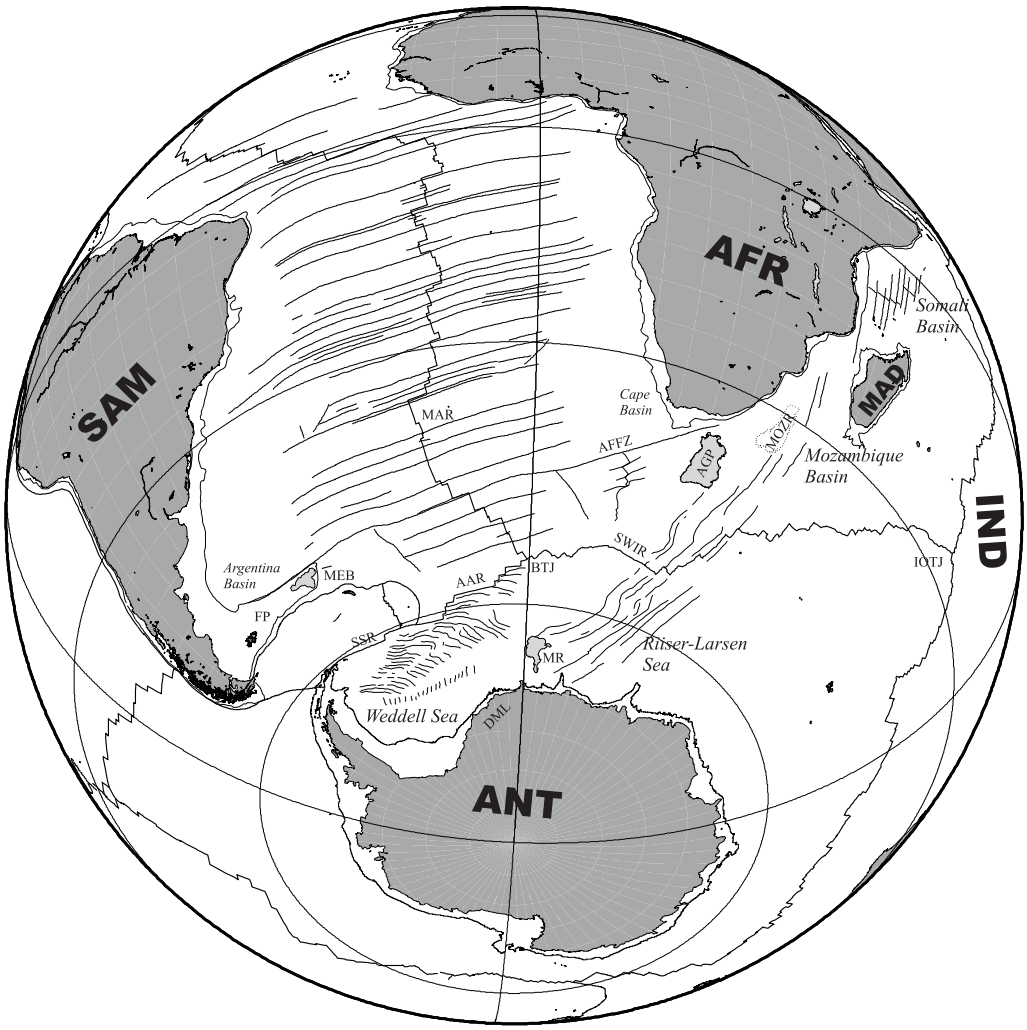

Figure 3.1-1: Overview map for the South Atlantic and southwestern Indian Ocean. The strikes of the major fracture zones between South America (SAM), Africa (AFR) and Antarctica (ANT) indicate the principal directions of movement during the dispersal of Gondwana. Abbreviations: AAR: America-Antarctic Ridge, AFFZ: Agulhas Falkland Fracture Zone, AFR: Africa, AGP: Agulhas Plateau, ANT: Antarctica, BTJ: Bouvet Triple Junction, DML: Dronning Maud Land, FP: Falkland Plateau, IND: India, IOTJ: Indian Ocean Triple Junction, MAD: Madagascar, MAR: Mid-Atlantic Ridge, MEB: Maurice Ewing Bank, MOZR: Mozambique Ridge, MR: Maud Rise, SAM: South America, SSR: South-Scotia Ridge, SWIR: Southwest Indian Ridge;

Bergh (1977), Norton and Sclater (1979), Martin and Hartnady (1986) and Roeser et al. (1996) and verified by recent investigations e.g. of Jokat et al. (2003b). However, much uncertainty still exists about the geometrical fit and subsequent drift history between SAM and ANT. Geophysical and geological data to describe the history of tectonic movements between these two continents are sparsely distributed and often of poor quality (Grunow, 1993; Ghidella et al., 2002; Jokat et al., 2003b). This is mostly due to the remoteness of the region, with parts of it being covered by ice for almost the entire year. Additionally, seafloor spreading anomalies

from the spreading system between SAM and ANT are strongly subdued in the southern Weddell Sea where the oceanic basement is covered by several kilometers of sediments (LaBrecque and Ghidella, 1997; Rogenhagen and Jokat, 2000). Thus, valuable information on the age of the ocean floor is very hard to interpret for the ANT side of the spreading system. The situation on the SAM side is even worse. There, the ocean floor that would have contained useful geochronological information about the early evolution of the plate pair has been destroyed by subduction beneath the overriding Sandwich plate. On the basis of these ambiguous data, a great number of different and differing models for the early opening of the Weddell Sea and the tectonic evolution of its neighboring continents has been developed in the last 25 years (Barker and Jahn, 1980; LaBrecque and Barker, 1981; Martin et al., 1982; Lawver et al., 1985; Martin and Hartnady, 1986; Lawver et al., 1992; Storey et al., 1996; Ghidella and LaBrecque, 1997; LaBrecque and Ghidella, 1997; Ghidella et al., 2002; Kovacs et al., 2002; Jokat et al., 2003b).

Due to the lack of sufficient data, many models providing reconstructions of SAM with respect to ANT are based on the combination of their motions with respect to neighboring plates (Lawver et al., 1985; Livermore and Hunter, 1996). The most direct and commonly used link in a global plate circuit is via the spreading regimes AFR-ANT and SAM-AFR. Problems resulting from this indirect determination of SAM-ANT rotations in the Weddell Sea were discussed by Barker and Jahn (1980).

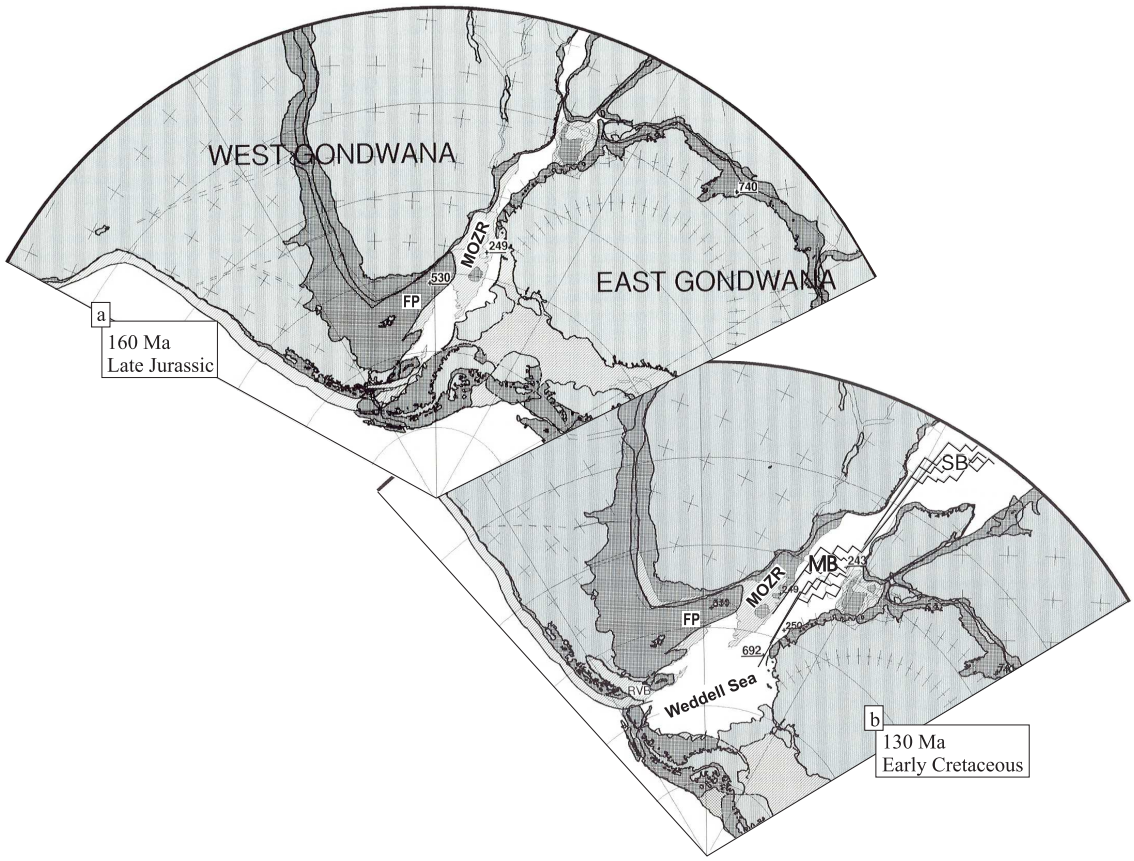

Figure 3.1-2: Reconstructions for the break-up of Gondwana for a) 160 Ma and b) 130 Ma, after Lawver et al. (1992). See text for a discussion. Abbreviations: FP: Falkland Plateau, MB: Mozambique Basin, MOZR: Mozambique Ridge, SB: Somali Basin; Figures modified after Lawver et al. (1992).

Lawver et al. (1992)

Some of the above mentioned models describe the early break-up of Gondwana as a 2-plate problem between rigid East (ANT, India and Madagascar) and West Gondwana (AFR and SAM) plates (Lawver et al., 1992; Reeves and de Wit, 2000; Kovacs et al., 2002). The assumption is made that AFR and SAM acted as a single rigid plate at least between 160 Ma and 130 Ma (Lawver et al., 1992; Kovacs et al., 2002). In the model of Lawver et al. (1992), this results in a large dextral strike-slip movement (several 100 km) between the Mozambique Ridge (MOZR) and East Antarctica (Figs. 3.1-2a,b) while seafloor spreading was active in the Mozambique and Somali basins between East- and West Gondwana. In this way, the sheared conjugate margins of western Dronning Maud Land and the eastern part of the MOZR were formed.

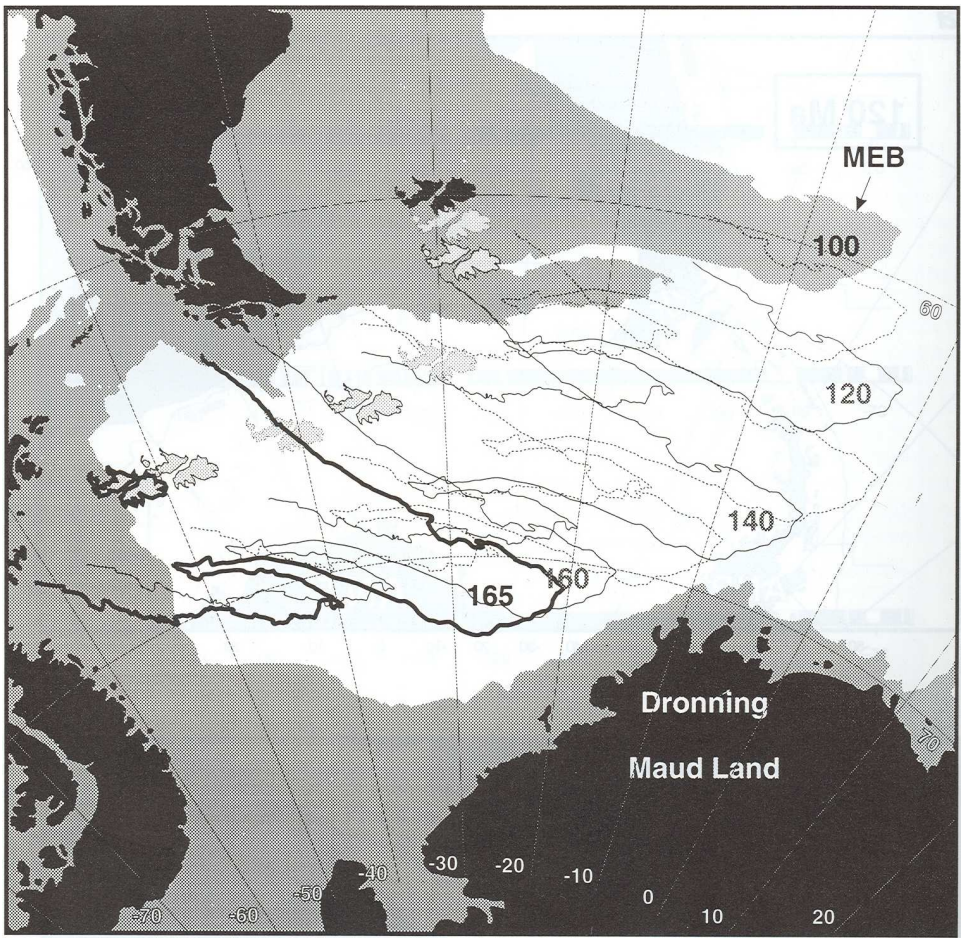

Figure 3.1-3: Reconstructions of the Falkland Plateau with respect to Antarctica (100-165 Ma), after Livermore and Hunter (1996). South America is shown in its 100 Ma position relative to Antarctica. Figure modified after Livermore and Hunter (1996).

Livermore and Hunter (1996)

The model presented by Livermore and Hunter (1996) confines the early movements between SAM and East ANT to strike-slip motions between the eastern end of the Falkland Plateau, namely the Maurice Ewing Bank, and the west coast of Dronning Maud Land (Fig. 3.1-3). In their model, the opening of the Weddell Sea starts with continental stretching at 165 Ma and finally leads to the separation of SAM from East ANT at about M10N (∼132 Ma) when north-south oriented spreading commences. The age information and constraints on the geometry of the spreading system are derived from a combined interpretation of marine magnetic anomaly and satellite derived free-air gravity data. However, due to uncertainties in the age of the oldest anomalies in the southern Weddell Sea, the final model for SAM-ANT is derived by combining rotations for the more precisely defined spreading regime between AFR and ANT with SAM-AFR rotations.

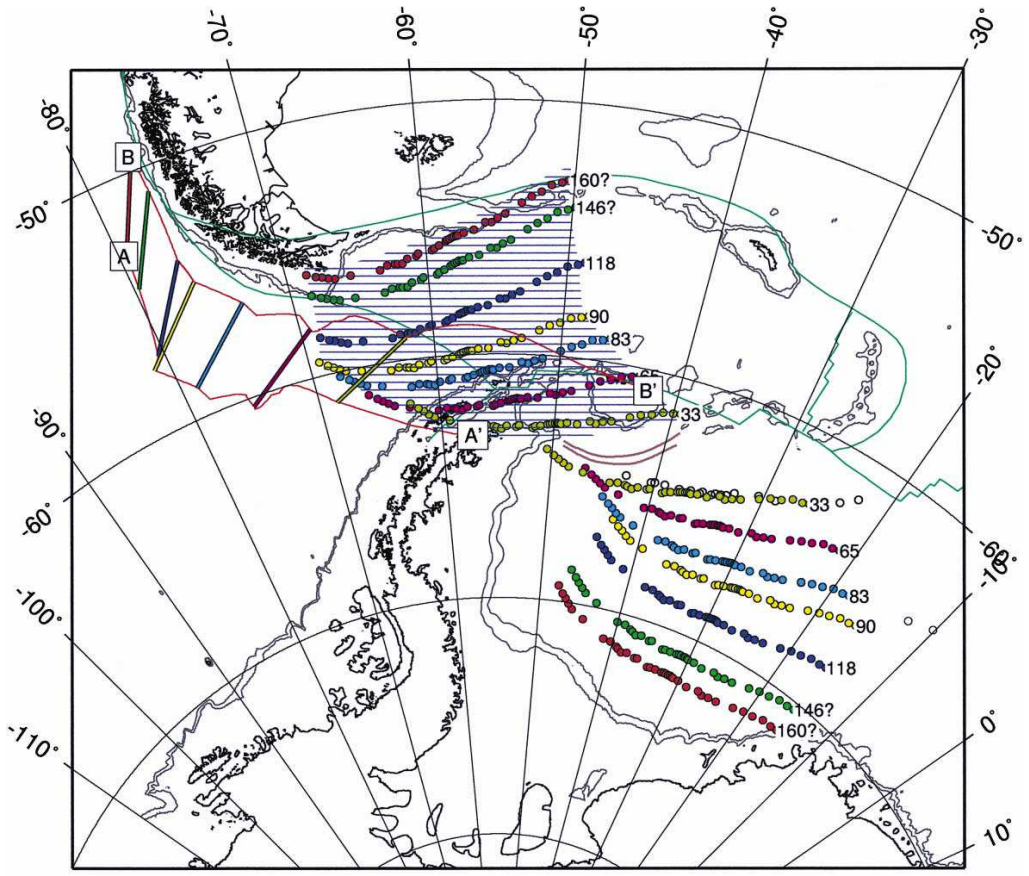

Figure 3.1-4: Synthetic isochrons (colored small circles) calculated from successive rotations of the C34 (83 Ma) magnetic anomaly picks backwards and forwards in time, by Ghidella et al. (2002). The isochrons south of SAM are plotted to show what their position would be if the Sandwich plate had not overridden the older seafloor. Figure modified after Ghidella et al. (2002).

Ghidella et al. (2002)

Ghidella et al. (2002) derived SAM-ANT rotations directly from an interpretation of magnetic anomaly and free-air gravity data in the Weddell Sea (Fig. 3.1-4). By successive rotations of the well-known C34 magnetic anomaly in the central Weddell Sea onto older identified anomaly lineations, stage poles for 83-90 Ma, 90-118 Ma, 118-146 Ma and 146-160 Ma were calculated. Using a total reconstruction pole for 83 Ma, total reconstruction rations were calculated for 90 Ma, 118 Ma, 146 Ma, 160 Ma. The sequence of synthetic isochrons in figure 3.1-4 indicates an almost constant spreading direction from the beginning of seafloor spreading at about 160 Ma until 90 Ma. Separation between SAM (with the Maurice Ewing Bank at its eastern end) and East ANT happens at about 146 Ma. As mentioned by Ghidella et al. (2002), the age constraints for the 146 Ma and 160 Ma rotations are very poor and so the older rotations are only tentatively dated.

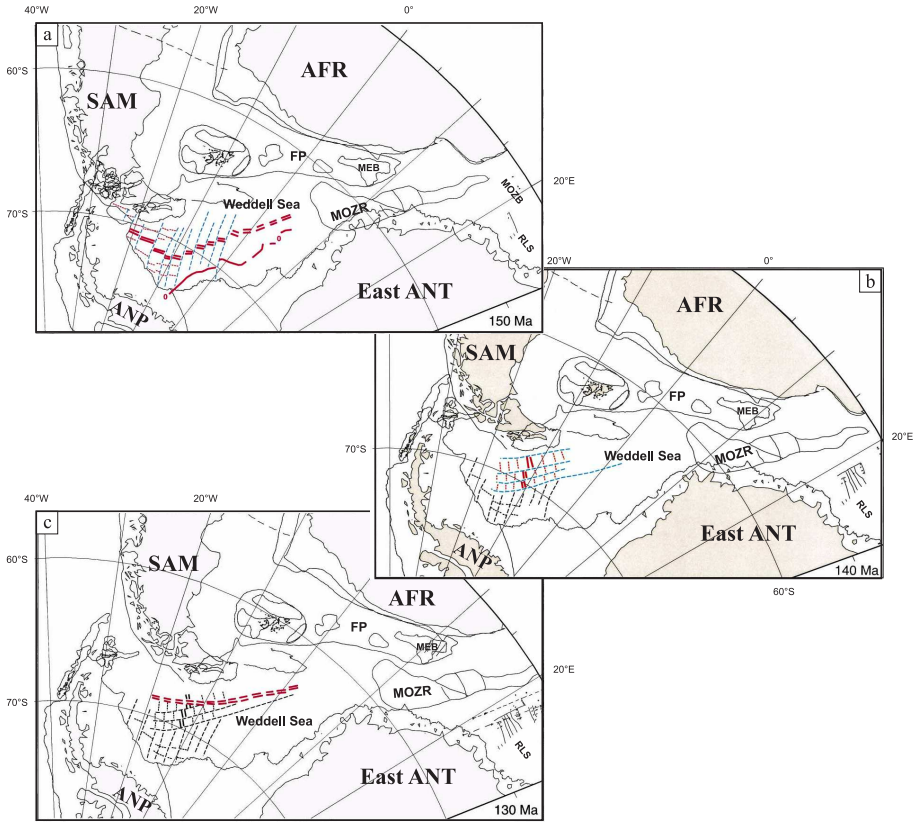

Figure 3.1-5: Reconstructions for the early stages of Gondwana break-up at a) 150 Ma, b) 140 Ma and c) 130 Ma, modified after Kovacs et al. (2002). Note the north-south orientation of the spreading system in the Weddell Sea at 140 Ma compared to the east-west oriented spreading system at 150 Ma and 130 Ma. See text for a more detailed discussion.

Kovacs et al. (2002)

Kovacs et al. (2002) used a comprehensive compilation of existing magnetic anomaly data and identified magnetic anomalies in the Weddell Sea Basin from present until M12A (135 Ma, using Gradstein et al. (1994)) (Fig. 3.1-5). Their model starts with an initial stage of north-south oriented spreading in the Weddell Sea acting between East- and West-Gondwana shortly before 150 Ma (Fig. 3.1-5a). This changes to an east-west orientated spreading system that is active at the time as north-south directed spreading between East- and West-Gondwana in the Mozambique Basin - Riiser-Larsen Sea and Somali Basin started around 140 Ma (Fig. 3.1-5b). At 130 Ma (Fig. 3.1-5c), the spreading direction in the Weddell Sea reverts to north-south, adopting lines of weakness inherited from the former east-west oriented spreading regime. This accompanies the beginning of the three-plate system ANT, SAM and AFR.

Jokat et al. (2003b)

Based on an interpretation of an extensive aeromagnetic dataset in the eastern Weddell Sea, the Lazarev Sea and the Riiser-Larsen Sea, Jokat et al. (2003b) propose an alternative model for the break-up of Gondwana. Thereafter, the first oceanic crust between Africa and Antarctica formed in the Riiser-Larsen Sea and the conjugate Mozambique Basin at about 155 Ma (M24). This occured contemporaneously with initial rifting in the Somali Basin. According to the interpreted magnetic anomaly data, a rift is proposed in the Weddell Sea propagating from southwest to northeast along the coast of western Dronning Maud Land for the time between magnetic chron M19N (145 Ma) and M17N (142 Ma). From the different spreading directions and velocities modeled for the AFR-ANT and SAM-ANT separation, Jokat et al. (2003b) conclude that extensional forces must have been active in the South Atlantic region between SAM and AFR at least since 155 Ma when the first spreading in the Riiser-Larsen Sea and the conjugate Mozambique Basin began. At M14N (∼137 Ma) SAM and AFR separated from the Antarctic continent in the area of the Lazarev Sea and the eastern Weddell Sea as interpreted from the coast parallel magnetic anomalies along the coast of western Dronning Maud Land. As a consequence of the above mentioned divergent movements between AFR, ANT and SAM, there were three separate large ocean basins developing independently already during the early stages of Gondwana break-up. This differs significantly from previously suggested models, e.g. by Lawver et al. (1998), proposing strike-slip movements in the Weddell Sea as a consequence of East-West Gondwana separation.

Uncertainties, however, still exist about the tectonic settings in the southwestern corner of Gondwana shortly before and during the initial opening of the Weddell Sea Basin. Since Jokat et al. (2003b) made no efforts to extend their model to the western Weddell Sea, no model parameters are presened describing the spreading system in the Weddell Sea. East Antarctica and the Antarctic Peninsula are treated as a single rigid plate excluding any extensional movements in the Filchner-Ronne Shelf. Thus, the relative position of SAM and the Antarctic Peninsula remains unclear for the period before SAM and AFR cleared the margin of East Antarctica at about 137 Ma. Similarly, the size of the Falkand Plateau is fixed throughout the opening scenario, which results in an unspecified overlap of the Maurice Ewing Bank onto the African continent during the initial stages of Gondwana break-up. Further uncertainties exist about the formation and development of the Mozambique Ridge. Although it is believed to be a continental sliver, no precise information exists about when and how this continental fragment cleared the coast of central Dronning Maud Land.

In this thesis, more detailed and extended reconstructions of the tectonic settings

during the break-up of Gondwana are presented for the western Weddell Sea, the Antarctic Peninsula and South America. The key to the development of a refined Gondwana break-up model is the determination of finite rotations for the opening of the Weddell Sea. The age constraints from the EMAGE aeromagnetic dataset, as presented by Jokat et al. (2003b), are used and combined with older published magnetic track data to determine a new age model for the ocean floor in the southern Weddell Sea. The strike and age of the magnetic anomaly identifications constrain the calculations of the new rotation parameters describing the opening of the Weddell Sea Basin. Combined with constraints from the other ocean basins in the South Atlantic region, a refined set of Gondwana break-up reconstructions is determined. This new model yields detailed information about the plate configurations shortly before and during the disintergration of Gondwana between 167 Ma and 83 Ma. The essential features defined by this model and their consequences are presented and discussed in chapters 3.4 and 3.5 of this thesis.

Before the data base and its processing will be discussed (Chapter 3.3) the major tectonic features in the Weddell Sea area and their interpretation are introduced.

3.2 Structural units and boundaries in the Weddell Sea

The major tectonic features of the Weddell Sea (Fig. 3.2-1) were investigated in the 1970's and 1980's by magnetic, bathymetric, gravimetric and seismic surveys of various nations (Germany, Great Britain, Japan, Norway, Russia, USA).

Knowledge of the southwestern Weddell Sea was significantly enhanced by the accomplishment of airborne surveys (magnetics and gravimetry) like the U.S.-Argentina-Chile (USAC) Project between 1985 and 1989 (LaBrecque et al., 1986; LaBrecque, 1987; LaBrecque et al., 1989) or the reconnaissance flights by Russian Antarctic expeditions in the years 1979 to 1989 (Masolov, 1980; Golynsky and Aleshkova, 2000). As part of the Antarctic Digital Magnetic Anomaly Project (ADMAP), these magnetic data were merged into a single data set together with a vast number of additional airborne and shipborne track data (Fig. 3.0-1). From this extensive magnetic database, a regional magnetic anomaly grid was calculated and is displayed in figure 3.2-2 (Golynsky et al., 2001). This grid covers almost the complete western and central Weddell Sea but has significant gaps in the eastern Weddell Sea and the Lazarev Sea.

On the magnetic anomaly map (Fig. 3.2-2), east-west oriented seafloor spreading anomalies are clearly visible between 45°W and 15°W in the northern Weddell Sea. The most significant anomaly is the strong negative polarity anomaly C33r (79 Ma) at about 65°S. This is followed to the south by the onset of C34 (83 Ma - 118 Ma),

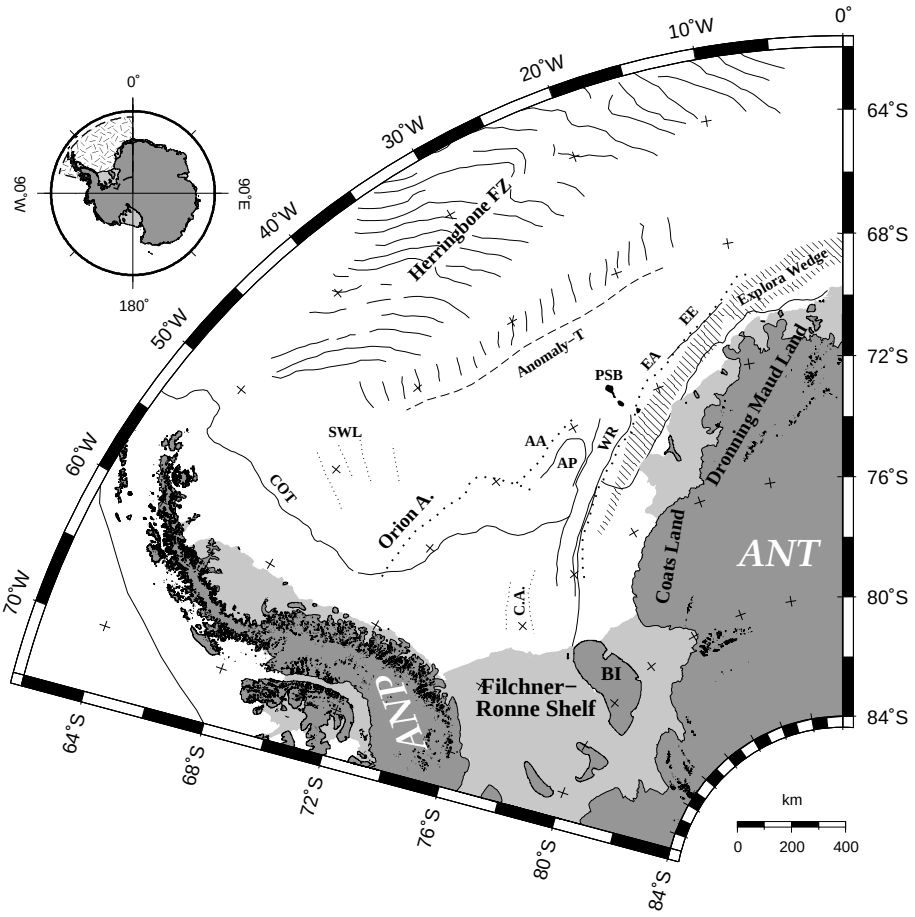

Figure 3.2-1: Tectonic overview of the Weddell Sea. The dominant features that are clearly identifiable on the magnetic and free-air gravity anomaly maps of figures 3.2-2 and 3.2-3 are the Orion Anomaly and the Explora Wedge (hatched area) in the southern and eastern Weddell Sea and the Herringbone fracture zone pattern in the northern Weddell Sea. Abbreviations: AA: Andenes Anomaly, ANP: Antarctic Peninsula, AP: Andenes Plateau, BI: Berkner Island, C.A.: Central Anomalies (after Ferris et al. (2000)), COT: Continent Ocean Transition, EA: Explora Anomaly, EE: Explora Escarpment, PSB: Polarstern Bank, SWL: Southwest striking lineations (after Ghidella et al. (2002)), WR: Weddell Rift.

the Cretaceous normal polarity superchron. The amplitudes of the magnetic anomalies are strongly reduced south of C34. Precise dating of this part of the ocean floor is difficult and rather tentative as reported, for example, by Livermore and Hunter (1996) and Ghidella et al. (2002). At 70°S between 55°W and 40°W, an elongated magnetic anomaly high, named the Orion Anomaly by LaBrecque et al. (1986), is juxtaposed with an area of low magnetic amplitudes further north. The dominant feature along the west coast of Dronning Maud Land is a continuous magnetic anomaly high of several hundred kilometers length and amplitudes of up to 500 nT. This is the Explora Anomaly (Johnson et al., 1992; Hunter et al., 1996). Its tectonic origin and relevance will be discussed later in this chapter.

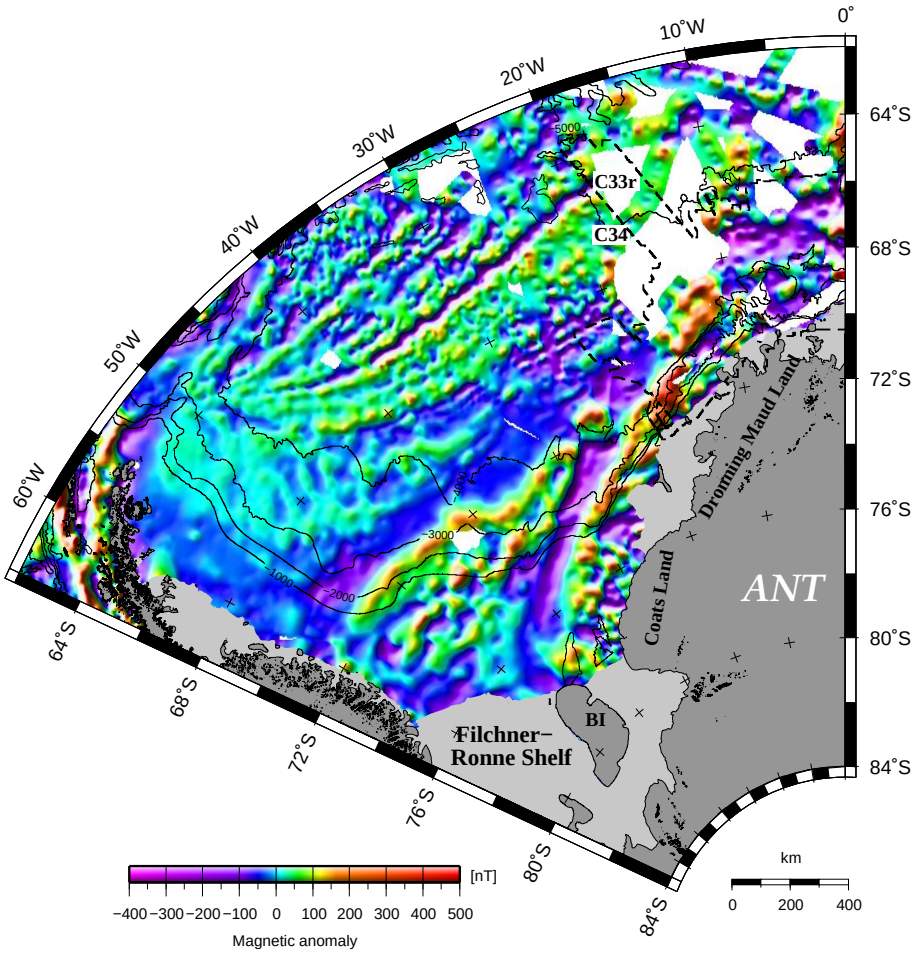

Figure 3.2-2: Magnetic anomaly map for the Weddell Sea. The data is extracted from the ADMAP compilation (Golynsky et al., 2001) and gridded on 2×2 min cells. The east-west oriented seafloor spreading anomalies in the northern Weddell Sea and the positive Orion and Explora anomalies in the southern and eastern Weddell Sea are the major magnetic signatures. The thick dashed line north of Dronning Maud Land indicates the survey area covered by the EMAGE project.

The recently acquired (1996 - 2002) high-resolution aeromagnetic data set of the East Antarctic Margin Aeromagnetic and Gravity Experiment (EMAGE) (Jokat et al., 2003b) closes one of the outstanding gaps in the ADMAP compilation (Figs. 3.0-1 and 3.2-2). While the area between 20°W and 8°E is only sparsely covered by a loose network of ship tracks, available to the ADMAP compilation, a dense network of aeromagnetic flight lines is provided by the EMAGE project for this region. In chapter 3.3.2, the EMAGE dataset will be introduced in greater detail. As shown by (Jokat et al., 2003b), this data set yields significant information on the age of the ocean floor north of Dronning Maud Land. Together with other published magnetic anomaly data further west in the Weddell Sea, anomaly identifications can be traced across the central and southern Weddell Sea and help to define the age of the oldest

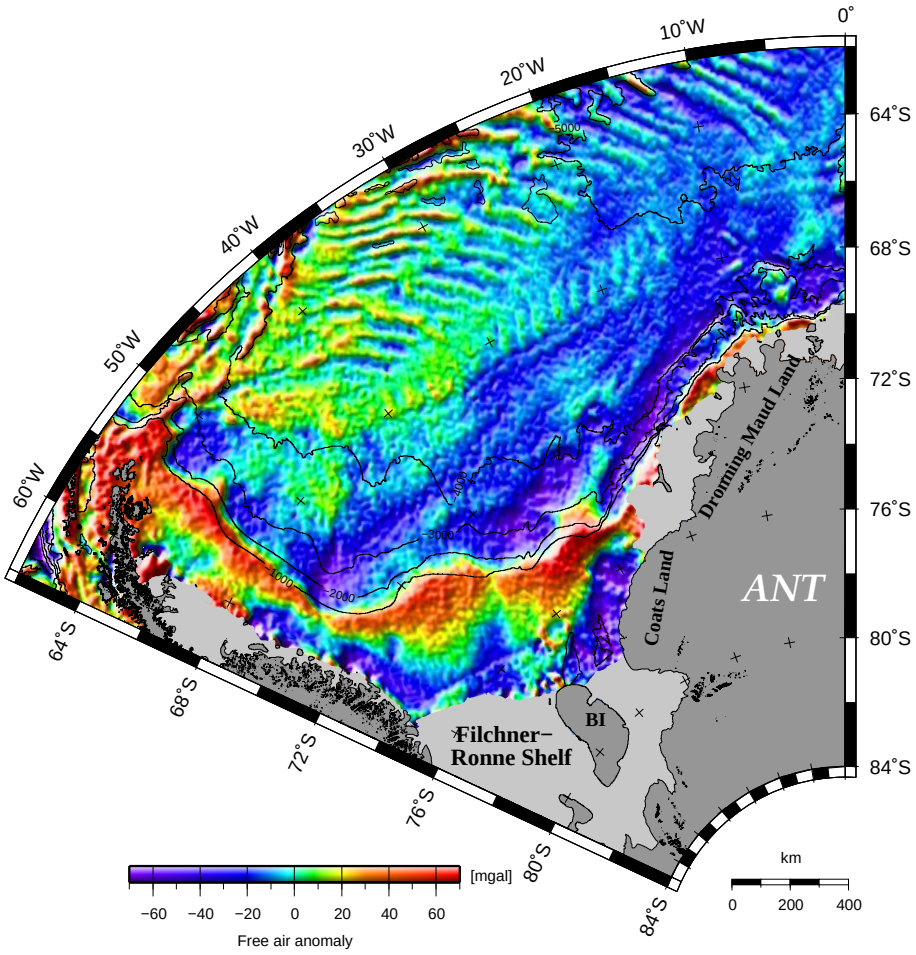

Figure 3.2-3: Free-air gravity anomaly map after McAdoo & Laxon (1997) calculated on 2×2 min cells. The Herringbone Fracture Zone pattern in the northern Weddell Sea is clearly identifiable.

ocean floor created during the inital stages of Gondwana break-up in the southern Weddell Sea.

Another comprehensive data set is provided by the means of satellite altimetry (Haxby, 1988; McAdoo and Marks, 1992a; McAdoo and Marks, 1992b). The latest and most detailed compilation for the Weddell Sea was released by McAdoo and Laxon (1997) who calculated a free-air gravity anomaly grid from retracked phase waveform data from the ERS-1 satellite (Fig. 3.2-3). The most prominent feature revealed by this free-air gravity anomaly grid is a pattern of closely spaced curvilinear gravity highs and lows in the northern Weddell Sea (Haxby, 1988) (Fig. 3.2-3). These anomalies are caused by fracture zones resulting from seafloor spreading between SAM and ANT (Haxby, 1988; Livermore and Woollett, 1993). Combination of magnetic anomaly data with this herringbone pattern (Livermore and Hunter, 1996) of flow lines indicates a WNW-ESE directed spreading regime being active

from before magnetic anomaly C34 (83 Ma) until the present (Livermore et al., 2005). South of the well defined onset of C34, the direction of the flow lines, and consequently the earlier spreading direction changes to NNE-SSW. Precise dating of this event is difficult since it occurs entirely within the Cretaceous normal polarity superchron (Livermore and Hunter, 1996). The southern part of the fracture zone pattern is bound to the south by a linear east-west oriented low amplitude gravity anomaly, termed Anomaly-T by Livermore and Hunter (1996) (Figs. 3.2-1 and 3.2-3). A continuation of the fracture-zone-related gravity anomalies across Anomaly-T was mentioned by Livermore and Hunter (1996) and McAdoo and Laxon (1996), but the anomalies are rather vague and were not included in their interpretations. Anomaly-T is interpreted as the gravity expression of an abrupt decline in spreading rate (Livermore and Hunter, 1996; Rogenhagen and Jokat, 2000). Due to uncertainties in the identification of the magnetic anomalies that are older than C34 (83 Ma), Anomaly-T could only be tentatively dated at between M0 (118 Ma) and M4 (126 Ma) in these publications. From interpretation of marine geophysical data (seismic and gravity), Rogenhagen and Jokat (2000) confirm the interpretation of Anomaly-T as being related to a decrease in spreading velocity during the opening between SAM and ANT. However, they are able to show that this gravity anomaly is not caused by a basement step as proposed by Livermore and Hunter (1996), or an inactive ridge as suggested by Barker and Jahn (1980).

Despite the existence of regional potential field data sets and thousand of kilometers of seismic lines in the central Weddell Sea, the structure and age of the oceanic crust south of Anomaly-T is still only sparsely known. One major problem that arises from uncertainties in the crustal structure is the definition of the continent ocean transition (COT) in this region. In general, it is believed that the prominent Orion magnetic anomaly (Figs. 3.2-1 and 3.2-2) marks the northern limit of the COT in the southwestern Weddell Sea (LaBrecque et al., 1986; Ghidella et al., 1991; Ghidella and LaBrecque, 1997; Ferris et al., 2000). The Orion anomaly is the southernmost pronounced magnetic anomaly and may be formed over extensive volcanic rocks that erupted at a volcanic rifted margin during the final break-up between SAM and ANT. The southern boundary of the COT may be located further south below the Filchner-Ronne Shelf along the long wavelength gravity high between 72°S, 50°W and 74°S, 30°W (Fig.3.2-3) and the 500 m isobath (Jokat et al., 1996). If this assumption is true, a long phase of extension and rifting took place in the southern Weddell Sea before the onset of seafloor spreading. Since no wide angle seismic data exist across the Orion anomaly to give more information on the deeper structure of the source body, no definite solution to this problem can be proposed.

Along the eastern margin of the Antarctic Peninsula (ANP), the COT is marked between 54°W and 56°W by a strong linear north-south striking gravity gradient (Bell et al., 1990; Brozena et al., 1990) (Fig. 3.2-3). The low amplitude magnetic anomalies along the entire margin, the thick sedimentary overburden, and the characteristic bathymetry, caused Ghidella and LaBrecque (1997) to suggest that the eastern margin of the ANP is a non-volcanic rifted margin. Ferris et al. (2000), on the other hand, interpret the sharply defined, straight nature of the gravity signal as typical of a sheared margin.

The eastern margin of the Weddell Sea, bound by the coast of western Dronning Maud Land, is a volcanic rifted margin (Hinz and Krause, 1982; Kristoffersen and Haugland, 1986). A continuous pattern of seaward dipping reflectors, named the Explora Wedge (Hinz, 1981) (Fig. 3.2-1), forms part of this volcanic margin between 25° - 0°W. Between 20°W and 10°W, the Explora Wedge coincides with the Explora Escarpment (Fig. 3.2-1) a pronounced bathymetric feature (Hinz and Krause, 1982; Kristoffersen and Haugland, 1986; Hinz and Kristoffersen, 1987; Miller et al., 1990; Kaul, 1991). The Explora Anomaly represents the magnetic expression of this structural boundary. The anomaly was correlated with the seaward dipping reflectors of the Explora Wedge by Kristoffersen and Hinz (1991). Jokat et al. (1996) propose the existence of a COT zone between the northern limit of the seaward dipping reflector sequences and a positive free-air gravity anomaly (50-100 mgal), which roughly coincides with the 500 m shelf break, on the continental side.

Further south in the eastern Weddell Sea, the Weddell Rift (Fig.3.2-1), a failed rift attributed to transtensional rifting between SAM and ANT during or before the opening of the Weddell Sea (Kristoffersen and Haugland, 1986; Kristoffersen and Hinz, 1991), marks a structural boundary between the East Antarctic craton and the Weddell Sea basin. This rift structure was correlated with a magnetic anomaly low of 100 km width by Johnson et al. (1992). Hunter et al. (1996) propose a southwestward continuation of the failed Weddell Rift along the prolongation of the magnetic low to the north-western corner of Berkner Island. East of this magnetic low, a pronounced Bouguer anomaly low is interpreted as representing Precambrian continental crust almost 200 km off the west coast of Coats Land (Studinger, 1998). Another hint of the existence of continental crust directly east of the inferred Weddell Rift comes from an interpretation of seismic lines off the coast of Coats Land by Haugland et al. (1985). These authors report basement outcrops, which may represent the East Antarctic craton, up to 50-100 km west of the ice front between 78°-75°30'S.

As reported from seismic refraction experiments by Grikurov et al. (1991), Miller et al. (1984), Hübscher et al. (1996), and Leitchenkov and Kudryavtzev (2000), the southernmost part of the Weddell Sea in front of the Filchner-Ronne Ice Shelf apparently consists of highly stretched continental crust (about 20 km thick, after Hübscher et al. (1996)) overlain by a 10-15 km thick sedimentary unit. Ferris et al. (2000) present a gravity and magnetic model for the Weddell Sea Embayment starting north of the Filchner-Ronne Ice Shelf and ending at about 68°S north of the Orion Anomaly. They modelled a thinned continental crust with up to 10 km of sediment loading over a large area in the southern Weddell Sea. This model supports the interpretation that the southern Weddell Sea underwent significant extension during or prior to seafloor spreading in the Weddell Sea and the break-up of Gondwana.

The structural units and continental boundaries described in this chapter are the data to be dealt with in any plate tectonic reconstruction for the Weddell Sea. These data put strong constraints on the fit of continental shore lines and the initial extend of continents and continental fragments. In the next chapter the magnetic anomaly database is introduced constraining the age of the ocean floor and thus the dynamics of the plate tectonic reconstruction. The refined model for the break-up of Gondwana presented in this thesis is based on the combination of these on- and offshore geological and geophysical data and seeks to satisfy all the different constraints in a best fitting way.

3.3 Data processing

The processing of the aeromagnetic data acquired during the EMAGE project (1996 - 2002), as presented in the next paragraph (3.3.1), is a contribution of the author of this thesis to the paper of Jokat et al. (2003b). This includes the compilation of the six individual EMAGE campaigns and their integration into a single database, the combined processing of the merged data set as described below and the grid production. All these steps of data processing were exclusively performed by the author of the thesis. Only, a first evaluation of the raw data was done in the field by the corresponding scientific field leader. The author attended the helicopter-borne survey during the season 2001-2002.
Parts of the text and figures in the following paragraph are taken from the paper of Jokat et al. (2003b) and will be referenced therein. However, it should be noted that all figures that are shown in the next paragraph and similarly in the paper of Jokat et al. (2003b) were compiled by the author of this thesis.

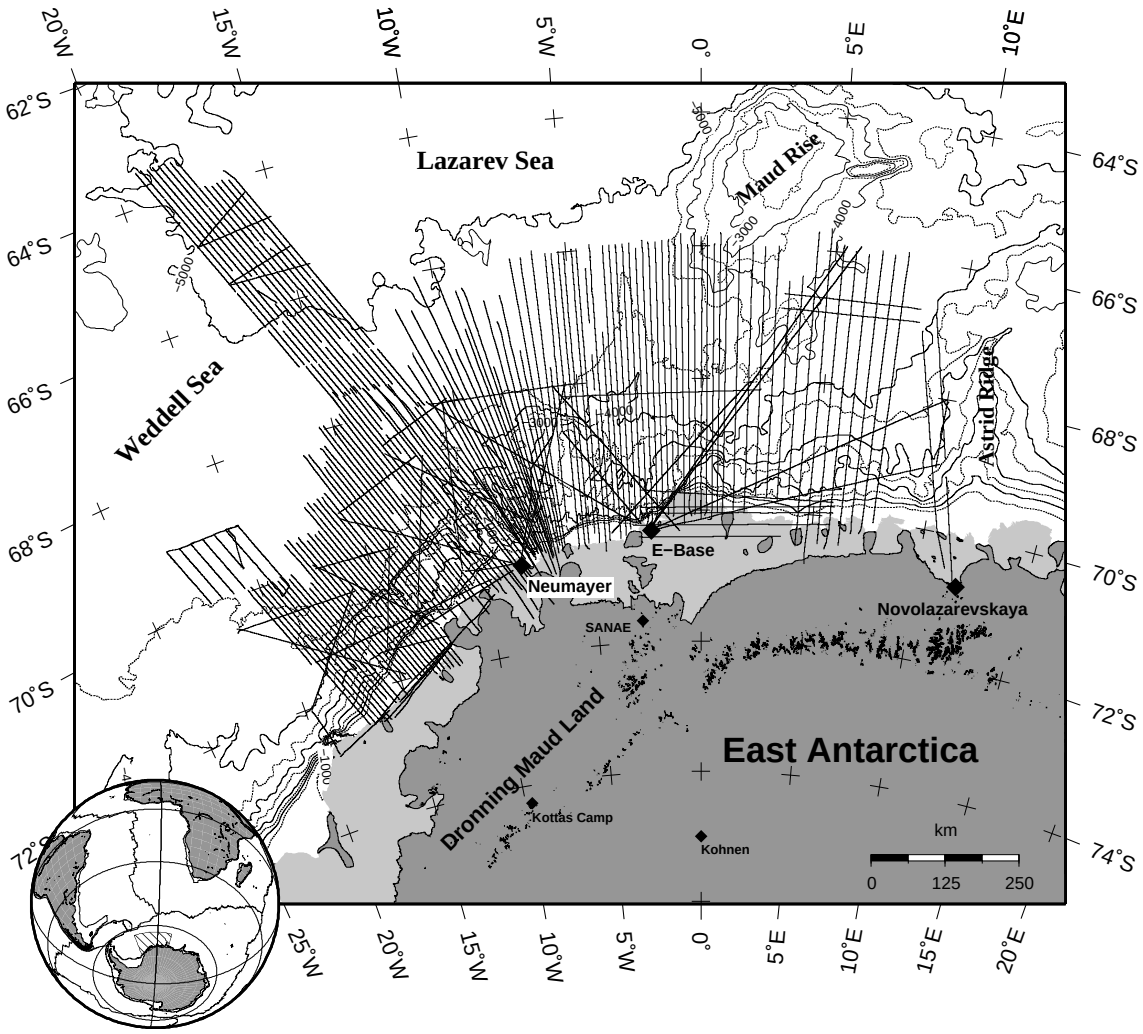

Figure 3.3-1: Flight lines performed during the EMAGE project. The inset shows the position of the plotted area in a South Atlantic Ocean perspective.

3.3.1 Compilation of the magnetic anomaly data

The East Antarctic Margin Aeromagnetic and Gravity Experiment (EMAGE) was carried out between 1996 and 2002. The area of interest was the region off the coast of central Dronning Maud Land (Fig. 3.3-1). Within six aeromagnetic campaigns, an overall length of 90000 km of magnetic data were flown on closely spaced flight lines covering an area of 680000 km^2. The average line spacing was about 9 km.

Most of the aeromagnetic measurements were carried out with the German research aircraft Polar-2, a Dornier-228. Additional lines still farther north, between 64°S and 68°S, were flown by helicopter operating from the RV *Polarstern* (Fig. 3.3-1). Both platforms were equipped with Cesium cell sensors (LRS Scintrex Inc.). The aircraft, bearing two sensor systems, one at each wingtip, operated at an average

speed of about 280 km/h and a flight level of 300 m, and the helicopter, towing the sensor about 30 m below its body, operated at an average speed of 120 km/h and a flight level of 150 m.

A first evaluation of the raw data was already performed during the respective field campaign by the involved scientists. This initial step of data processing included the visual inspection of the raw data and the elimination of spikes or sections of poor signal quality due to other errors. Especially, in the helicopter magnetic data spikes had to be edited resulting from short-wave radio transmissions. A correction for the International Geomagnetic Reference Field (IGRF) (e.g. IAGA (1996)) was applied next.
Further processing steps were performed during the compilation of the final data set as part of this thesis. The LCT software package (Fugro-LCT) was used for most of the line data processing during and after the field work. Only the IGRF correction and upward continuation (see below) were performed with software adopted from other sources. For the IGRF correction source code distributed by the National Geophysical Data Center (Boulder, Colorado) was used.
For correcting data for the daily variations of the earth's magnetic field, base station data were available from observatories and temporary field stations at Neumayer Station (Germany), E-Base (Republic of South Africa) and Novolazarevskaya (Russia) (Fig. 3.3-1). Large distances between these base stations and the far end of the track lines were inavoidable, since the flight lines were located completely over the ocean and base stations could be deployed only at certain sites restricted to the coast of Dronning Maud Land (Jokat et al., 2003b). Distances of up to 1000 km occurred with the helicopter survey and about 500 km with the fixed wing survey. However, in order to reduce the influence of strong diurnal magnetic variations during local (magnetic) night time hours, flight times were adjusted to the predominantly magnetically quietest hours (Jokat et al., 2003b). Additionally, a 1800 sec lowpass filter was applied to the data in order to reduce the disturbing effect of high frequency variations in the base station data. The final correction was done by removing the IGRF-corrected and filtered base station data from the track line data.
Since different flight levels were adopted by the aircraft and helicopter and variations in the flight altitude were sometimes necessary due to bad weather conditions, all data were continued to a common datum of 1500 m (Jokat et al., 2003b). This means an average upward continuation of 1350 m for the helicopter borne survey and 100-500 m for all other surveys. The field continuation was applied using the equivalent source algorithm of Hansen and Miyazaki (1984) (not implemented in FUGRO's LCT software).
After merging the data into one common database, a systematic adjustment proce-

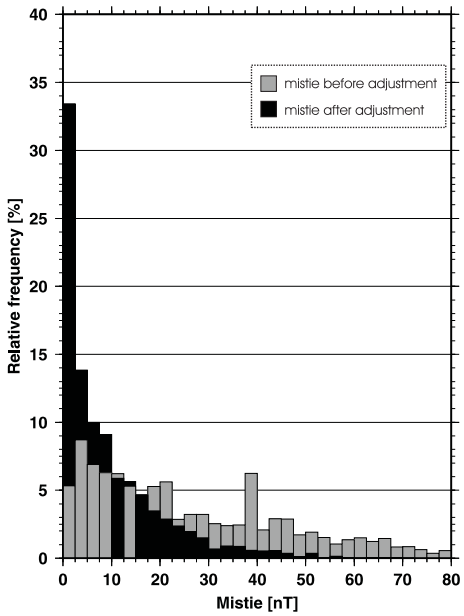

Figure 3.3-2: Histogram plot of the cross point errors before and after the systematic adjustment procedure Jokat et al. (2003b).

dure was used to reduce the crossover errors (Jokat et al., 2003b). A total of 3608 cross points were available, having a mean error of 31.7 nT before and 9.4 nT after, the adjustment procedure (Fig. 3.3-2). The individual lines were adjusted by a first order polynomial fit. This means each line was shifted and tilted by amounts that minimize the sum of the squared crossover errors. The distribution of the crossover errors before and after this processing step is given in figure 3.3-2. Track lines without any cross point were adjusted manually afterwards.

Figure 3.3-3 shows the processed magnetic anomaly data along their flight lines (wiggle plot) after the above mentioned corrections and adjustments were applied to the data. Clearly, coherent anomalies parallel to the coast of Dronning Maud Land are visible in the western part of the survey area (>10°W). Rather long wavelength high amplitude anomalies occur in the east. Maximum amplitudes of the anomalies reach values of more than 600 nT.

For the last processing step, the gridding, a minimum curvature algorithm was used, provided by the Generic Mapping Tools (GMT) of Wessel and Smith (1998). This processing step varies from the one described in the paper of Jokat et al. (2003b) since here, the final grid comprises of three individual parts accounting for the varying line spacings of the individual campaigns.
Due to different line spacings in the eastern, middle and western parts of the sur-

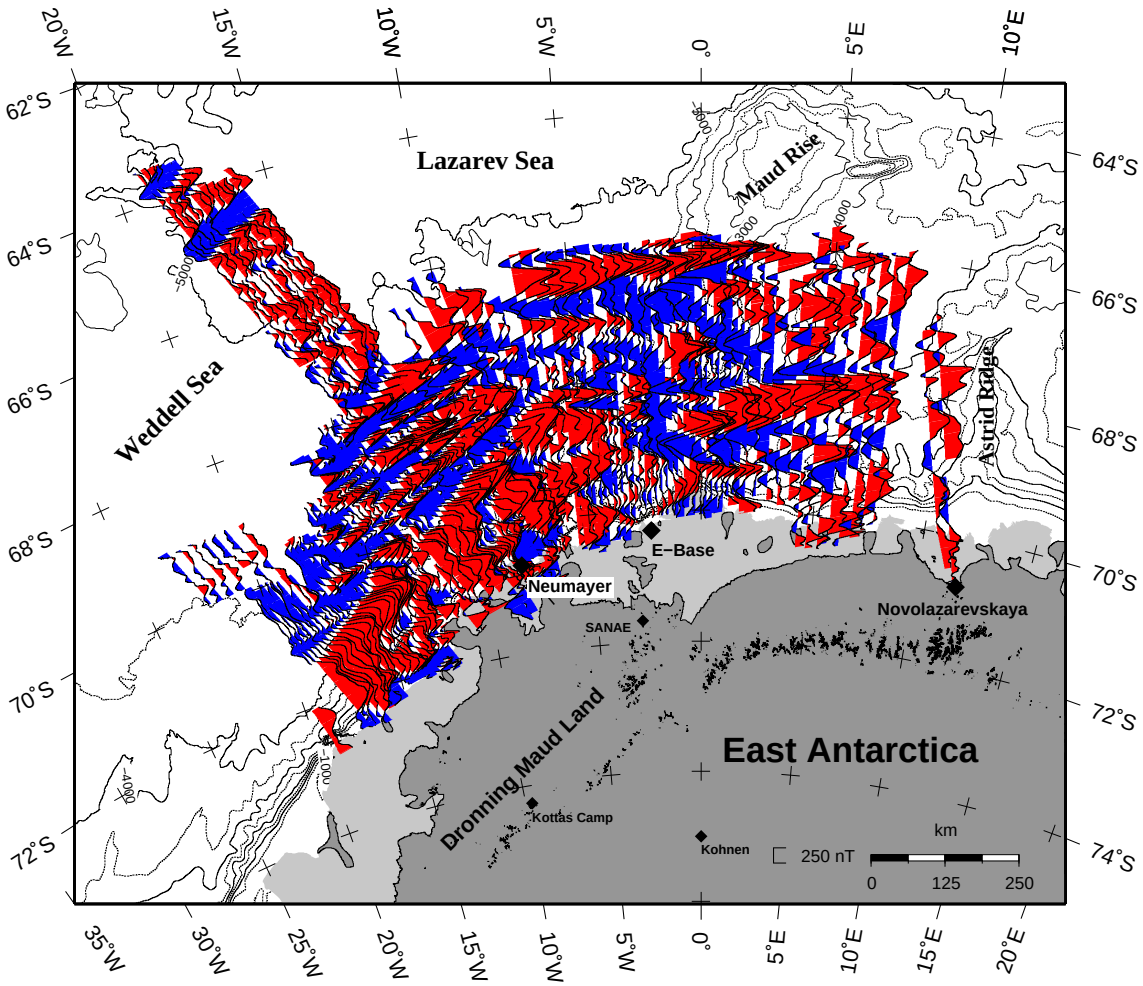

Figure 3.3-3: Wiggle plot of all processed EMAGE lines. The tie lines are omitted for clarity. Red filling indicates positive anomalies and blue filling negative anomalies. 500 m bathymetric contours are derived from the ETOPO2 2×2 min data set from the NGDC (National Geophysical Data Center, Boulder, Colorado). Figure modified after Jokat et al. (2003b).

vey area (∼15 km, ∼10 km, ∼6 km), the final grid is the result of merging three individual grids with cell sizes of 10×10 km, 5×5 km and 2×2 km, respectively. For gridding operations, the data were first transformed from the geodetic to a polar stereographic coordinate system. After merging the 3 independent grids, a lowpass with a cutoff wavelength of 20 km was applied to reduce distortions at the grid boundaries. The resulting grid was interpolated to a cell size of 2×2 km and is shown as a color-shaded relief in figure 3.3-4. 200 nT contours are plotted on top of the grid to visually enhance the strike of the major magnetic anomalies. Some of the well correlated magnetic anomalies are labelled according to the identifications of Jokat et al. (2003b). Anomaly identifications shown in this and all following chapters are labelled after the geomagnetic polarity time scale of Cande and Kent (1995) for chrons younger than C34 (83 Ma) and after Kent and Gradstein (1986)

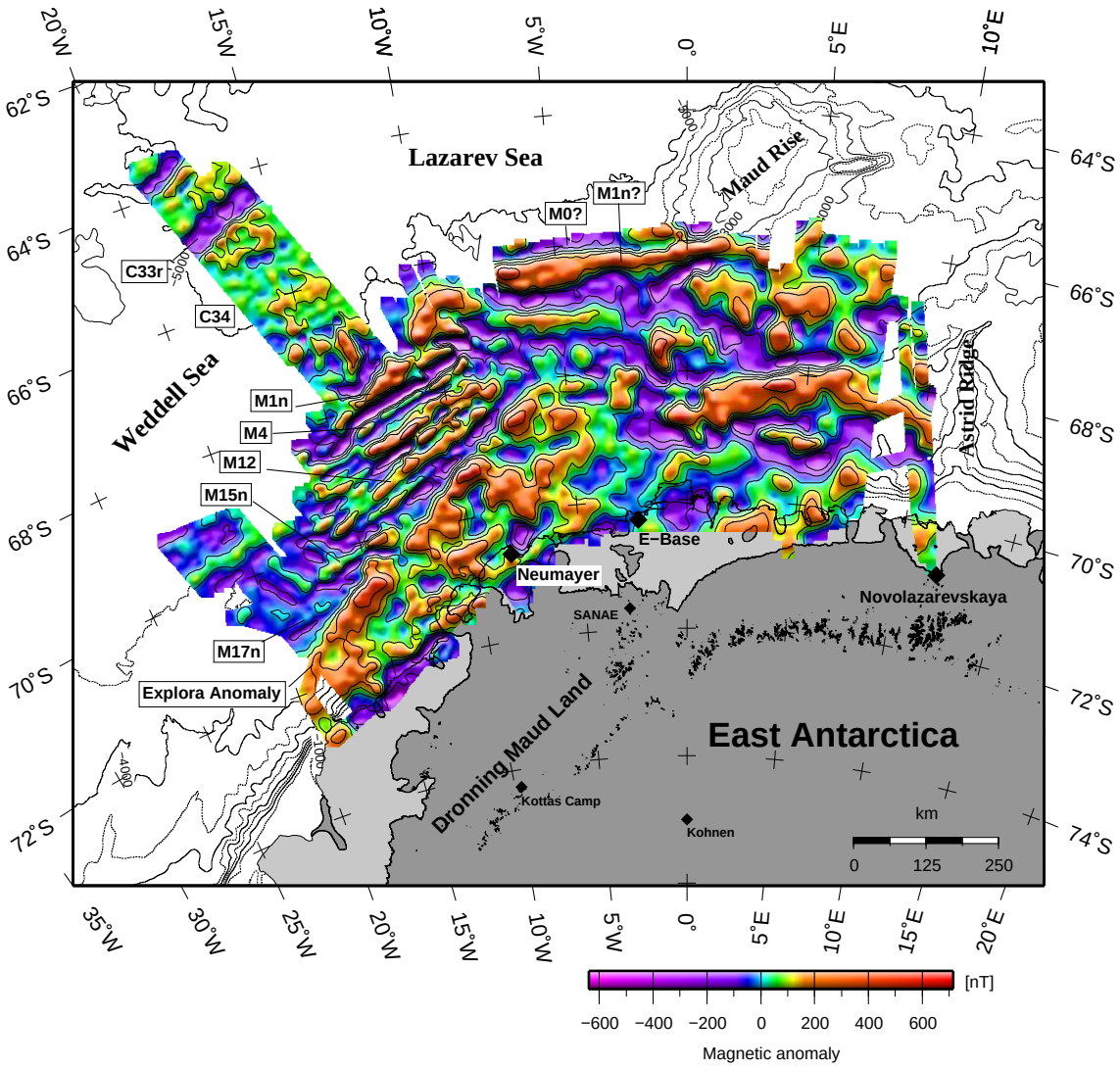

Figure 3.3-4: High resolution aeromagnetic anomaly grid for the eastern Weddell Sea and Lazarev Sea, based on the EMAGE data set (Fig. 3.3-1). A grid cell size of 2×2 km is used. The underlying bathymetric contours are derived from the ETOPO2 2×2 min data set from the NGDC. See text for details. Figure modified after Jokat et al. (2003b).

for older times. Figure B in the appendix shows the Kent and Gradstein (1986) geomagnetic polarity time scale for reference.

In figure 3.3-4, the coast-parallel strike of the seafloor spreading anomalies in the eastern Weddell Sea is apparent (Jokat et al., 2003b). These anomalies terminate in the south against the long wavelength (∼50 km) high amplitude (>600 nT) Explora Anomaly. Through a correlation of these well constrained magnetic anomaly identification with aeromagnetic and ship track data further west in the Weddell Sea, the ocean floor in the central and southern part of the Weddell Sea can be dated more precisely than previously published, for example, by Livermore and Hunter

(1996) and Ghidella et al. (2002). The resulting set of anomaly identifications for the southern Weddell Sea will be presented in the next chapter.

3.3.2 Magnetic anomaly identifications

To better constrain the age of the ocean floor in the Weddell Sea Basin, the detailed set of magnetic anomaly identifications made from the EMAGE data set in the eastern Weddell Sea (Jokat et al., 2003b) was correlated with additional published magnetic anomaly data acquired in the central and southern Weddell Sea in the last 30 years (Fig. 3.3-5).

Early magnetic anomaly data were acquired in the eastern and southern Weddell Sea during reconnaissance expeditions carried out by the British Antarctic Survey (BAS) in 1974 to 1980 (Barker and Jahn, 1980). Since navigation was restricted to satellite fixes performed every 16 km, the ship track is only known to about 2 km. For data acquisition, a ship-towed proton precession magnetometer was used. No diurnal variations were removed from the data, but the three-hourly planetary indices were checked for the presence of large magnetic disturbances (Barker and Jahn, 1980).

An extensive aeromagnetic data set from the southernmost parts of the Weddell Sea and onshore Dronning Maud Land was provided by the Polar Marine Geological Research Expedition (PMGRE, Russia) carried out in the years 1979 to 1989 (Masolov, 1980; Golynsky and Aleshkova, 2000). An area of about 1850000 km^2 was covered with 14 surveys on a line spacing of mostly 20 km and onshore Dronning Maud Land even 5 km (Golynsky and Aleshkova, 2000). The latter one was not used in this study. The proton precession magnetometer measurements were primarily registered on analog charts and subsequently digitized. Diurnal corrections were applied to the data in a post-processing sequence (Golynsky and Aleshkova, 2000). This data set was not used for the modelling of magnetic anomaly sequences but significantly enhanced the interpretation of geologic structures and boundaries in the southern Weddell Sea and the Filchner-Ronner Shelf.

Another important data set for the Weddell Sea Basin and the Antarctic Peninsula comes from the U.S.-Argentina-Chile project (LaBrecque et al., 1986; LaBrecque, 1987; LaBrecque et al., 1989). This was carried out in the years 1985 to 1989 using a long range Orion P-3 based at Punta Arenas and Ushuaia. As for the surveys introduced above, a proton precession magnetometer was used for data acquisition. An early version of a Global Positioning System (GPS) as well as the aircraft's inertial navigation system served for track positioning (Ghidella et al., 2002).

These additional track data from the central and southern Weddell Sea were used in combination with the EMAGE data set to constrain the age of the ocean floor across

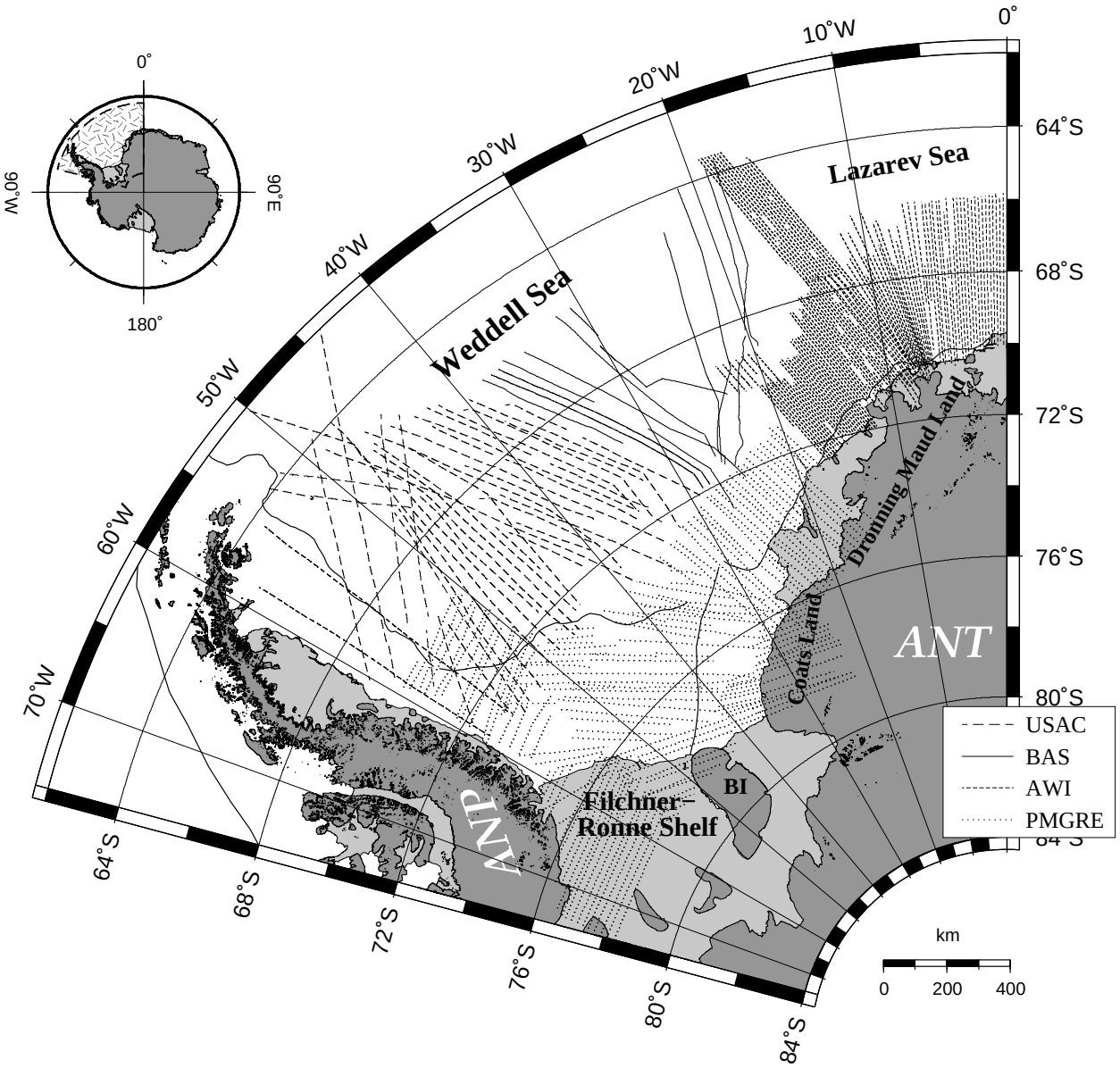

Figure 3.3-5: Overview map of the Weddell Sea showing magnetic track lines used to identify the magnetic anomalies. Abbreviations used in the legend: USAC: U.S.-Argentina-Chile project (1985-1989), BAS: British Antarctic Survey expeditions (1974-1980), AWI: Alfred-Wegener-Institute (1996-2002), PMGRE: Polar Marine Geological Research Expedition (1976-1989), former Soviet Antarctic Expedition.

the Weddell Sea Basin. A wiggle plot of these lines is shown in figure 3.3-6. The final set of magnetic anomaly picks made throughout the Weddell Sea is overlain on the anomaly data.

Note that the wiggles from the EMAGE data set are scaled to half the amplitude of the USAC and BAS track data. Amplitudes along the Explora Anomaly and within the magnetic seafloor spreading stripes in the eastern Weddell Sea are almost twice as high as those in the central and southern part of the Weddell Sea.

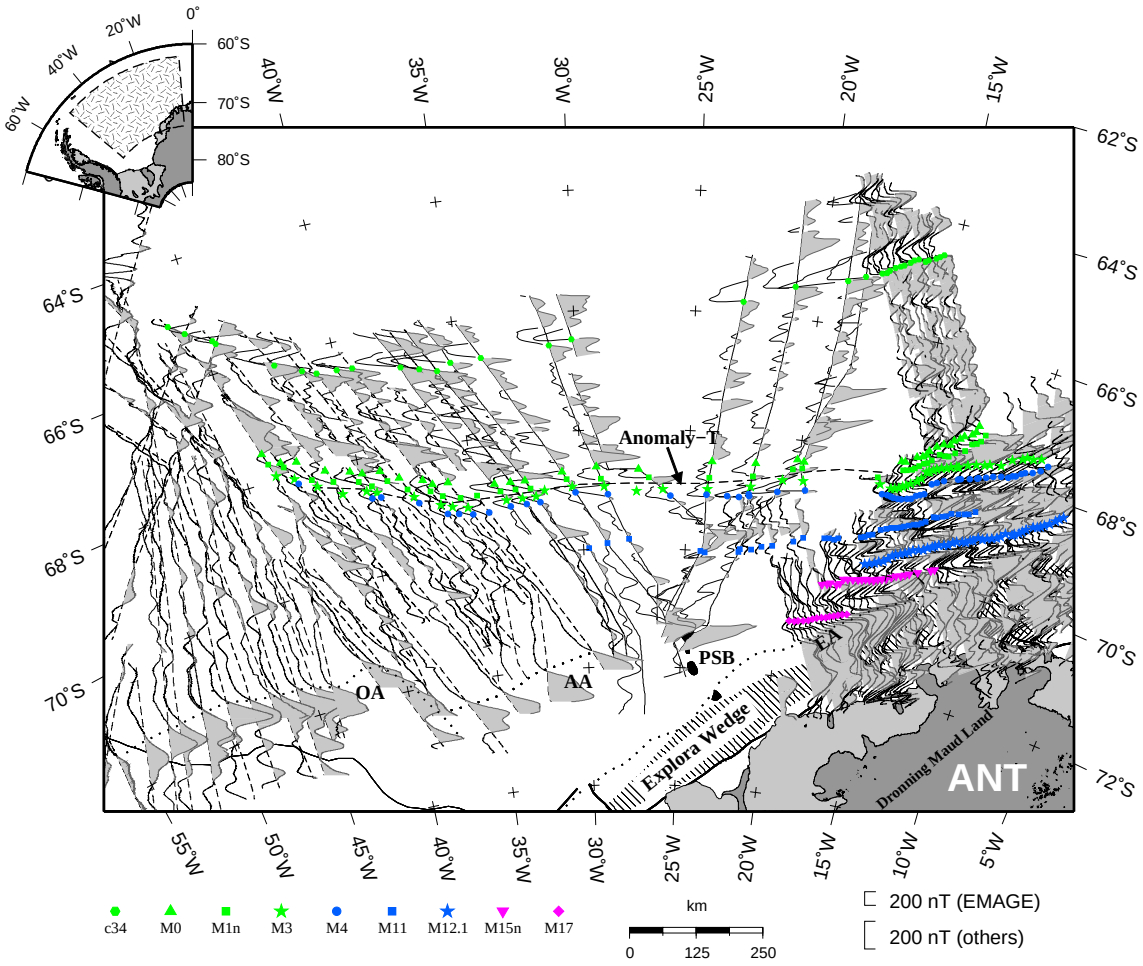

Figure 3.3-6: Wiggle plot of profiles used to identify the magnetic anomalies in the Weddell Sea. The anomaly picks shown are those used to define the rotations for the opening of the Weddell Sea. Note the different scale of the magnetic anomalies for the EMAGE and BAS, USAC profiles. Abbreviations: AA: Andenes Anomaly, EA: Explora Anomaly, OA: Orion Anomaly, PSB: Polarstern Bank.

Most of the lines from the USAC project end just to the south of the Orion Anomaly. Thus, seafloor spreading anomalies along the aeromagnetic profiles can only be identified north of this long wavelength anomaly. Unfortunately, amplitudes are rather low in this area, due to the 5-7.5 kilometers of nonmagnetic sedimentary cover (Rogenhagen and Jokat, 2000). Correlations of magnetic anomalies across several lines are only possible north of 69°S. The ship track data from the British Antarctic Survey (BAS) are overprinted in the south by the magnetic expression of the Polarstern Bank, a chain of seamounts off the northwestern coast of Dronning Maud Land (Jokat et al., 1996). The strong magnetic signature of the seamounts interferes with any possible seafloor spreading anomaly signal and makes their identification almost impossible in this region. From figure 3.3-6, an eastward continuation of M17

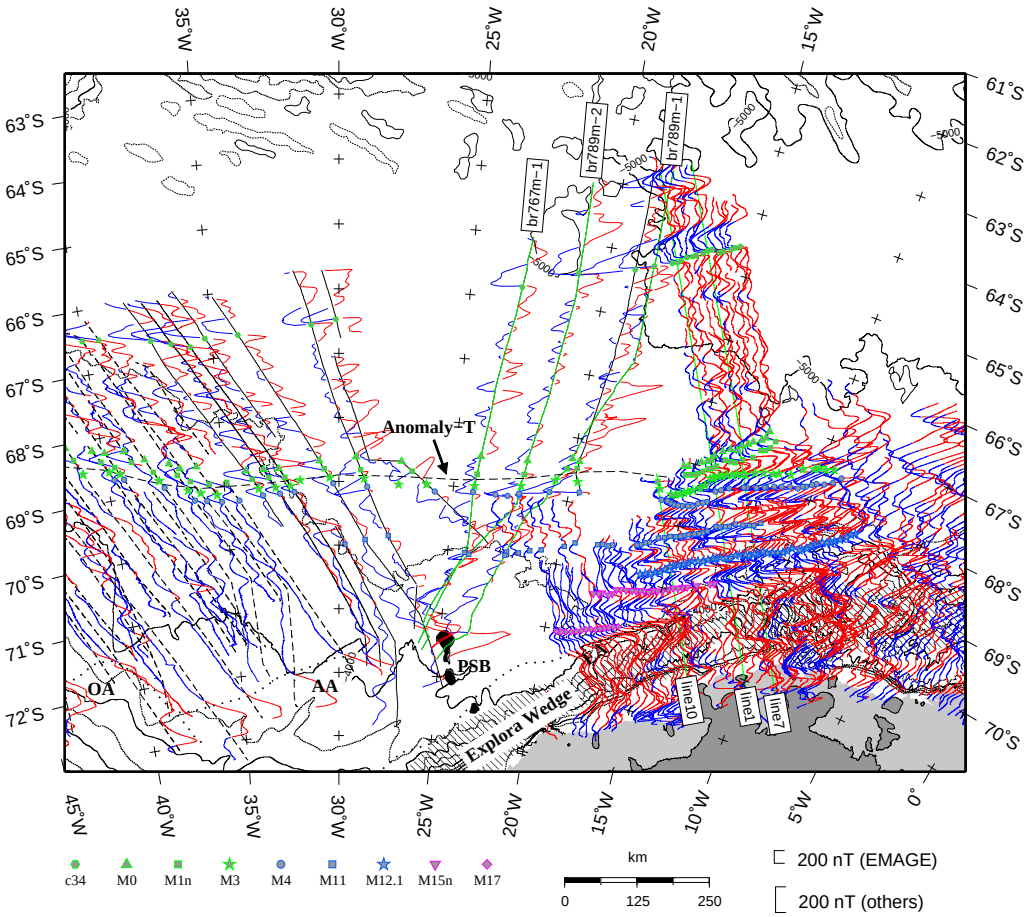

Figure 3.3-7: Magnetic anomaly plot of all profiles used to define the magnetic anomaly picks. Red wiggles indicate positive anomalies and blue ones negative anomalies. The profiles that are correlated with the calculated spreading model in figure 3.3-8 are labeled. Note the different scales of the magnetic anomalies for the EMAGE, BAS, and USAC profiles. Abbreviations are the same as in figure 3.3-6.

(142 Ma) would be expected to be present in the vicinity of the Polarstern Bank, but cannot be identified in the data due to the strong magnetic overprint induced by the seamounts. In the northern part of the Weddell Sea, the distinctive onset of magnetic anomaly C34 (83 Ma) can clearly be correlated between all profiles. This and the younger C31 (∼68 Ma) magnetic anomaly have been used as anchors for the calculation of synthetic anomaly sequences.
The profiles for which correlations with synthetic anomaly sequences were made are indicated in figure 3.3-7 and the correlations themselves are shown in figure 3.3-8.

The selected EMAGE lines are arbitrarily numbered. The BAS line names correspond to the ship's name RRS Bransfield (br) and the season of acquisition. For example, br767 means the expedition during the austral summer 1976/77. Spread-

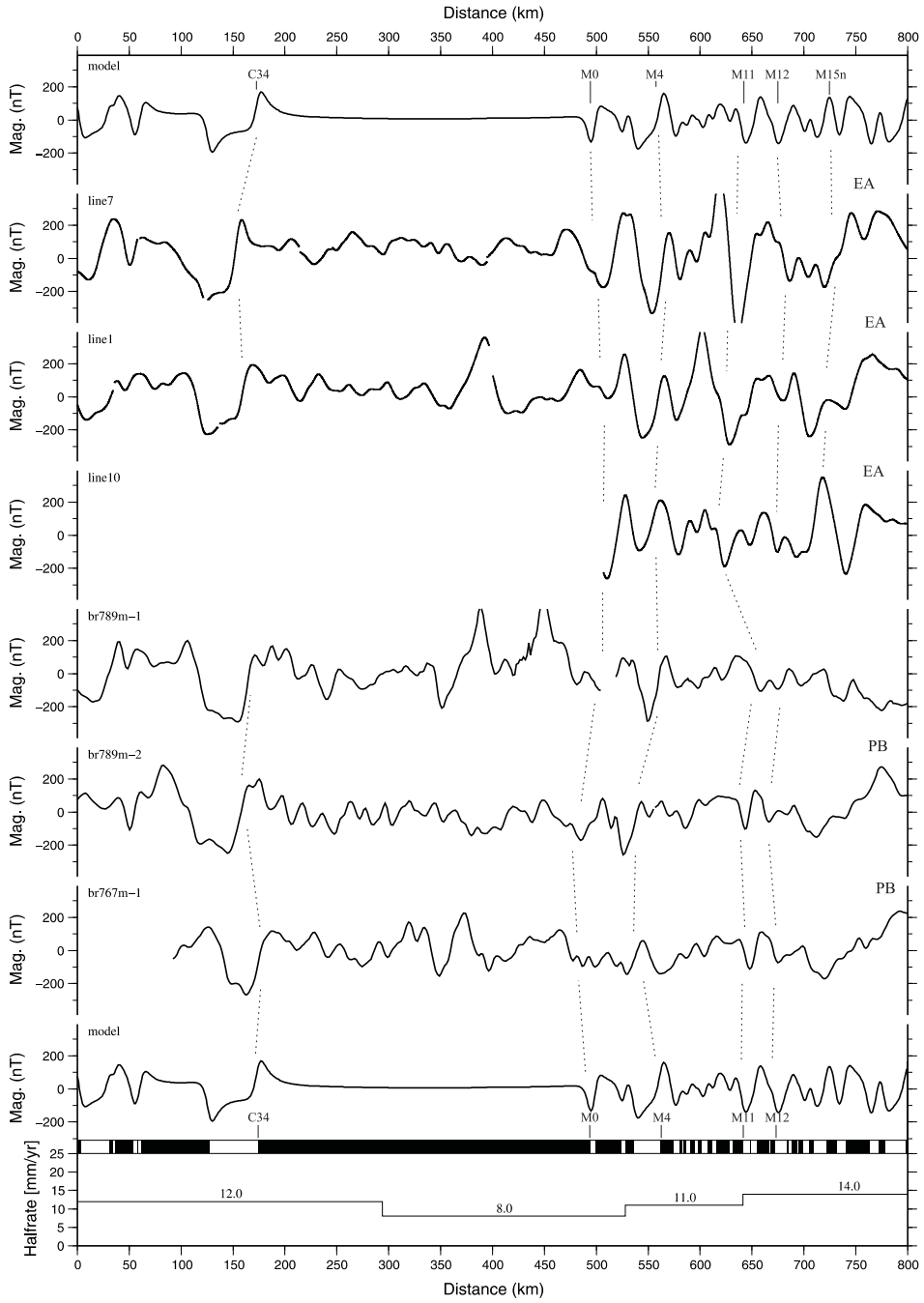

Figure 3.3-8: Selected magnetic anomaly profiles correlated with a spreading model for the Weddell Sea. The anomaly profiles shown here are indicated in figure 3.3-7.The EMAGE profiles (line7, line1, line10) are projected onto 155°, and the BAS profiles onto 170°. The spreading model is calculated using a 1 km-thick source layer at 6 km constant depth. The lowermost line shows the corresponding spreading halfrates. Correlated anomalies are connected with dashed lines. Abbreviations: EA: Explora Anomaly, PB: Polarstern Bank.

ing models were calculated also for all other profiles shown on figure 3.3-6 to identify magnetic anomaly C34 (83 Ma), M0 (118 Ma), M1n (122 Ma), M3 (123 Ma) and M4 (125 Ma). However, no unique identifications could be made for the older anomalies

along these profiles.
In order to reduce the skewness of the anomalies along the selected profiles, the track data were projected onto lines parallel to the expected spreading direction. Thus, the EMAGE lines were projected onto lines with an azimuth of 155° and the BAS profiles onto 170° (counterclockwise positive from north). The synthetic anomaly sequence was calculated using a magnetic block model confined to a magnetic layer at 6 km depth and a thickness of 1 km. The spreading rates used to calculate the model are shown in figure 3.3-8.

The onset of magnetic anomaly C34 (83 Ma) can easily be identified on all lines in figure 3.3-8. The long period of the Cretaceous normal polarity superchron consists of several isolated anomaly highs on line1, br789m-1 and br767m-1, but these cannot be correlated over larger distances. The beginning of M-sequence anomalies, starting with M0 (118 Ma), can be identified on all lines. Although the westernmost line, br767m-1, shows no distinctive negative anomaly for M0, the position of the picked anomaly correlates with the anomalies identified further east (Fig. 3.3-7). M1n (122 Ma) and M3 (123 Ma) are also picked on all profiles and presented in figure 3.3-7. These two anomalies almost perfectly bracket the indicated position of Anomaly-T (thick dashed line). Magnetic anomaly M4 (125 Ma) can be identified as a dominant positive anomaly on all profiles. While M11 (133 Ma) can be revealed as a strong negative anomaly in all the EMAGE lines, its correlation on the ship track data is more difficult. However, the small helicopter magnetics pattern between 69°S-70°S and 20°W-23°W clearly indicates the continuation of the pronounced M11 (133 Ma) anomaly in the east and can be used to constrain M11 (133 Ma) on the ship track data further west. M12 can also be identified on the BAS ship track data, except for line br789m-1. Further south, no unique correlations can be made between the ship profiles and anomalies picked from the EMAGE data set. Consequently, anomalies M15n (138.3 Ma) and M17 (142 Ma) can only be identified on the EMAGE profiles.
This set of magnetic anomaly picks (Fig. 3.3-6) and the spreading rates shown in the lower part of figure 3.3-8 were used to constrain the rotations for the opening of the Weddell Sea as shown in the next chapter.

3.3.3 Calculation of rotation parameters

Doing paleogeographic reconstructions for the Mesozoic break-up of Gondwana calls for some description of the relative plate motions of the major continents SAM, AFR and ANT. This is a three-plate system, the relative motions of which can be calculated by performing numerical inversions if sufficient magnetic anomaly and fracture zone data are available (e.g. Nankivell (1997) and references therein). This is the

case for ages younger than 83 Ma, the beginning of the Cretaceous normal polarity superchron. A high resolution three-plate reconstruction for the South Atlantic Ocean was presented by Nankivell (1997) for the time from 84 Ma until present. In this study, however, calculations were done by trial-and-error in view of the sparse data basis, especially for times shortly before and after the onset of seafloor spreading in the ocean basins. A MATLAB (The MathWorks, Inc.) software package has been developed to perform the calculations and visualize the results since no other program was available at the time which provided the desired functionality as already mentioned in greater detail at the beginning of chapter 3.

In the first part of this chapter, the calculation of the finite rotations for the SAM-ANT spreading system is explained, and the constraints used to define the motions between AFR-ANT and SAM-AFR are introduced. This mainly concentrates on the presentation of the magnetic anomaly identifications of the respective ocean basins. In the second part, the method applied for determining the rotation parameters for the three-plate system of SAM-AFR-ANT is described.

The reconstructions presented in this thesis are calculated assuming rigid lithospheric plates. Motions of rigid plates on a sphere can be described by Euler rotations. These rotations are performed around a rotation axis through the center of the Earth. The intersection of the rotation axis with the Earth's surface is called the Euler pole. The angle of rotation about this pole is conventionally measured counterclockwise. In plate tectonic reconstructions, two kinds of Euler rotations are commonly used (Cox and Hart, 1986). Finite rotations (pole + angle) reconstruct the relative position of two continents at a given time. These are also called total reconstructions if the rotation has the present day at its end point. Stage rotations describe the relative motion of two plates during a period of constant rotation. While total reconstructions always start at present, stage rotations can be defined for any time interval. A mathematical formulation of Euler rotations and their use in plate tectonic reconstructions can be found, for example, in Cox and Hart (1986) or Greiner (1999) and references therein.

While seafloor spreading anomalies from conjugate ocean basins are fit to one another to constrain the relative position of two continents at a given time; fracture zone data from the ocean basins are compared with calculated flow lines to verify the direction of the plate motions.
Unfortunately for the spreading regime between SAM and ANT, no seafloor spreading anomalies conjugate to the Weddell Sea anomalies exist along the southern margin of the Falkland Plateau. Another way to determine the rotations was used

instead and will be described in the next paragraph.

SAM-ANT

The SAM-ANT spreading regime is only constrained by magnetic anomaly and fracture zone data from the Weddell Sea Basin. While fracture zones can be identified in free-air gravity data north of Anomaly-T, they are either absent or their signal is too weak for being detected south of Anomaly-T (Figs. 3.2-3 and 3.3-9). Thus, the only available information constraining the SAM-ANT spreading history for times older than Anomaly-T comes from the interpretation of magnetic anomaly data. This sparse database makes the use of inversion techniques like those presented by Livermore et al. (2005) for the northern Weddell Sea difficult and the results rather speculative.

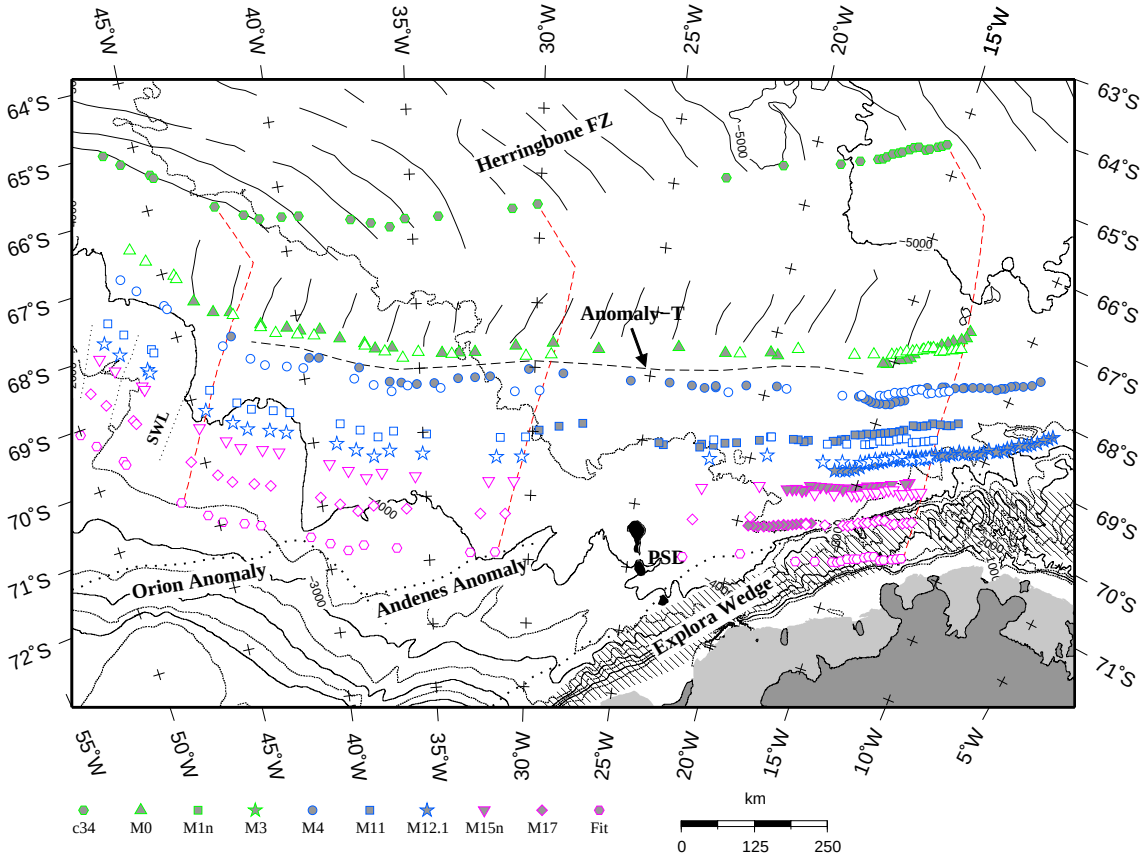

Figure 3.3-9: Synthetic isochrons calculated from the successive rotations of C34 (83 Ma) magnetic anomaly picks to fit the older identified anomalies. Calculated flowlines are compared to fracture zone lineations north of Anomaly-T. The southernmost synthetic isochron (labeled Fit) is determined from an extrapolation of the spreading system to the south assuming constant spreading rate and azimuth.

Therefore, a method like the one presented by Ghidella et al. (2002) was used in this thesis. In this method, rotation parameters are estimated by rotating picks of a well constrained magnetic anomaly of one flank of the spreading system to fit the picks of older or younger anomalies of the same flank of the spreading system. Assuming symmetric spreading, these stage rotations can be used to calculate total reconstructions for the two-plate system. In this way, Ghidella et al. (2002) calculated a set of finite rotations for the SAM-ANT spreading system for the time between 160 Ma and 33 Ma.
In this thesis, picks of the well defined northern limit of magnetic anomaly C34 (83 Ma) are rotated to fit picks of older anomalies in the southern Weddell Sea. A comparison between the picks made on the anomaly data and the rotated and adjusted C34 anomaly picks is shown in figure 3.3-9. The rotation parameters used to calculate the position of the rotated C34 anomaly picks are listed in table 3.3-T1.

Table 3.3-T1: Rotations applied to the C34 magnetic anomaly picks to calculate the synthetic isochrons shown in figure 3.3-9.The finite rotation for 83.00 Ma is used to calculate the total reconstruction rotations.

Ages [Ma]	Lon. [°]	Lat. [°]	Angle [°]
0.00 - 83.00	-77.92	246.51	-30.08
83.00 - 118.00	-71.90	296.21	-7.83
118.00 - 125.36	-80.08	312.78	-1.08
125.36 - 132.53	-94.90	336.15	-0.88
132.53 - 134.75	-120.50	27.27	-0.34
134.75 - 138.30	-66.38	299.14	-1.38
138.30 - 142.27	-117.83	30.64	-0.59
142.27 - 147.00	-117.77	30.74	-0.71

The poles are stage poles for the rotation of SAM with respect to ANT. The angles are half the angles of the stage rotations (the angle for the 83.00 Ma total reconstruction is a full angle). To calculate the total reconstruction rotation for SAM with respect to ANT from these stage rotations, one has to add up all stage rotations starting from the present day.
If t_n is the age for which a total reconstruction is to be calculated, this calculation can be written as (Cox and Hart, 1986):

$$^{0}_{SAM}ROT^{t_n}_{ANT} = ^{0}_{SAM}ROT^{t_1}_{ANT} + ^{t_1}_{SAM}ROT^{t_2}_{ANT} + \ldots + ^{t_{n-1}}_{SAM}ROT^{t_n}_{ANT}$$

In this way, total reconstruction rotations for M0 (118 Ma), M4 (125 Ma), M11 (133 Ma), M12.1 (135 Ma), M15n (138 Ma) and M17 (142 Ma) are obtained. These

are listed in table C-1 in the appendix.

Assuming a constant spreading rate and direction for times older than magnetic anomaly M17 (142 Ma), the spreading system is extrapolated to the south until the rotated C34 (83 Ma) anomaly picks occupy a position just north of the Orion magnetic anomaly (Fig. 3.3-9). Since purely oceanic crust is very unlikely to exist further south in the Weddell Sea (see chapter 3.2 for details), this may be the position of the initial rift after initiation of the SAM-ANT separation. This extrapolation results in a maximum age for the oldest ocean floor in the Weddell Sea of about 147.00 Ma (Table 3.3-T1).

Synthetic flowlines were calculated using the rotation parameters presented above (Fig. 3.3-9). These are used to visualize the spreading direction and to make a comparison with fracture zone lineations digitized from gravity data (McAdoo and Laxon, 1997).

AFR-ANT

Mesozoic seafloor spreading between AFR and ANT was confined to the conjugate Riiser-Larsen Sea and Mozambique Basin. Magnetic anomaly and fracture zone data used to constrain the relative position of these two continents are shown in figures 3.3-10 and 3.3-11.

Magnetic anomaly data in the Riiser-Larsen Sea were digitized from ship track data presented by Bergh (1977) and picked on line data from the high resolution aeromagnetic data set presented by Jokat et al. (2003b). For the conjugate part, the Mozambique Basin, data from Cande et al. (1989) and the "Digital seafloor spreading lineations for the World's Oceans" database (NGDC, Boulder) were used (Fig. 3.3-11). Outlines of the major fracture zones in these two ocean basins were digitized from the satellite altimetry-derived free-air gravity data of Sandwell and Smith (1997).

Tikku et al. (2002) proposed that an extinct Cretaceous spreading center was active between AFR and the Mozambique Ridge in the northern Natal Valley between about 132 Ma and 122 Ma. This implies an independent Mozambique Ridge block at least for this time period. To define the boundaries of this block its positive signal in the free-air gravity field has been used as proposed by Tikku et al. (2002). The magnetic anomaly identifications in the northern Natal Valley were digitized from Tikku et al. (2002) and are shown in figure 3.3-11.

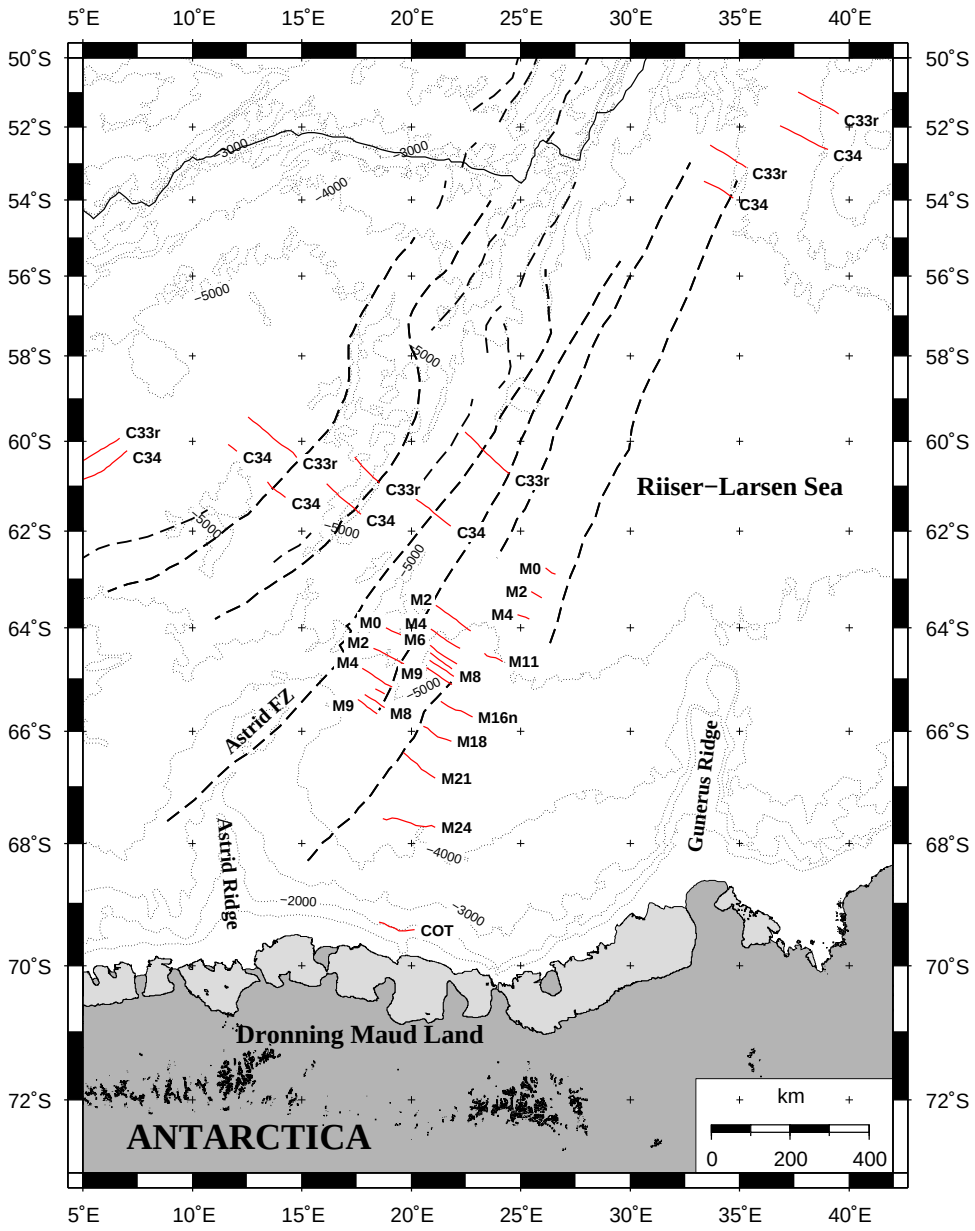

Figure 3.3-10: Magnetic anomaly and fracture zone data in the Riiser-Larsen Sea used to constrain the position of ANT with respect to AFR. Fracture zones are plotted as heavy dashed lines. See text for references.

SAM-AFR

Constraints on the early seafloor spreading history between SAM and AFR are obtained from magnetic anomaly and fracture zone data in the conjugate Argentine and Cape basins and the Georgia and southern Natal basins. Figures 3.3-11 and 3.3-12 give an overview of the data used to describe this spreading regime.

Magnetic anomaly lineations in the Argentine Basin were digitized from data presented by Rabinowitz and LaBrecque (1979) and Max et al. (1999). For the Cape Basin, anomaly data presented by Rabinowitz and LaBrecque (1979) and Schrecken-

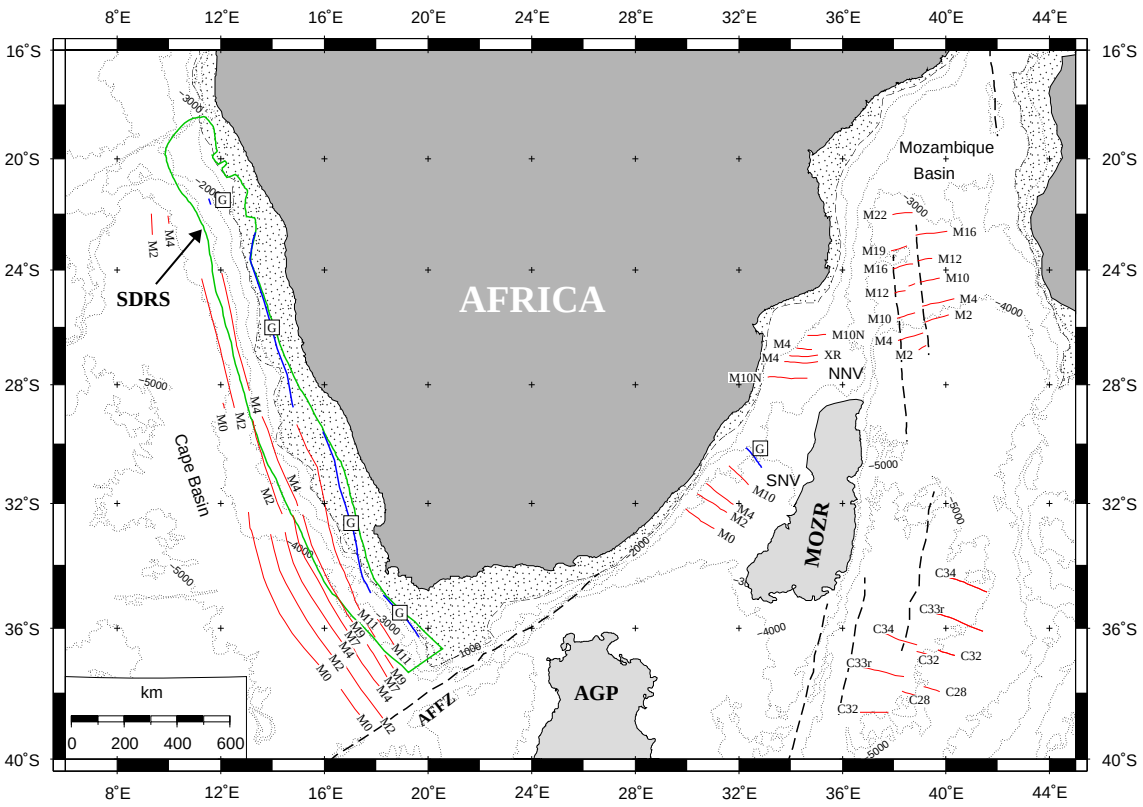

Figure 3.3-11: Map of the ocean basins bordering the AFR continent and the magnetic anomalies used to constrain the AFR-ANT and SAM-AFR reconstructions. Magnetic anomaly G (blue line) is interpreted as an edge effect anomaly separating oceanic from continental basement, after Rabinowitz and LaBrecque (1979). The maximum extent of continental material is indicated by the stippled area bordered by thin dashed lines. See text for references. Abbreviations: AFFZ: Agulhas Falkland Fracture Zone AGP: Agulhas Plateau MOZR: Mozambique Ridge NNV: Northern Natal Valley SDRS: Seaward dipping reflector sequences (green outline) SNV: Southern Natal Valley

berger and Neben (2003) were used. The outline of magnetic anomaly C34 (83 Ma) in both ocean basins was taken from Cande et al. (1989).

Anomalies in the Georgia Basin (east of Maurice Ewing Bank), representing the SAM side of a spreading system between the Falkland Plateau and AFR, were picked from the original track line data as distributed by the NGDC on the GEODAS CD-Rom and from digitized maps for the 1976 cruise of RRS Shackleton (Barker, 1979; Martin et al., 1982). The identification of the anomalies was taken from LaBrecque and Hayes (1979). For the conjugate to the Georgia Basin, the southern Natal Valley, magnetic anomaly lineations were digitized from the original work of Goodlad et al. (1982).

Fracture zone lineations in the above mentioned ocean basins were digitized from the gravity data presented by Sandwell and Smith (1997).

To define the fit of the continents, detailed knowledge of the continent-ocean tran-

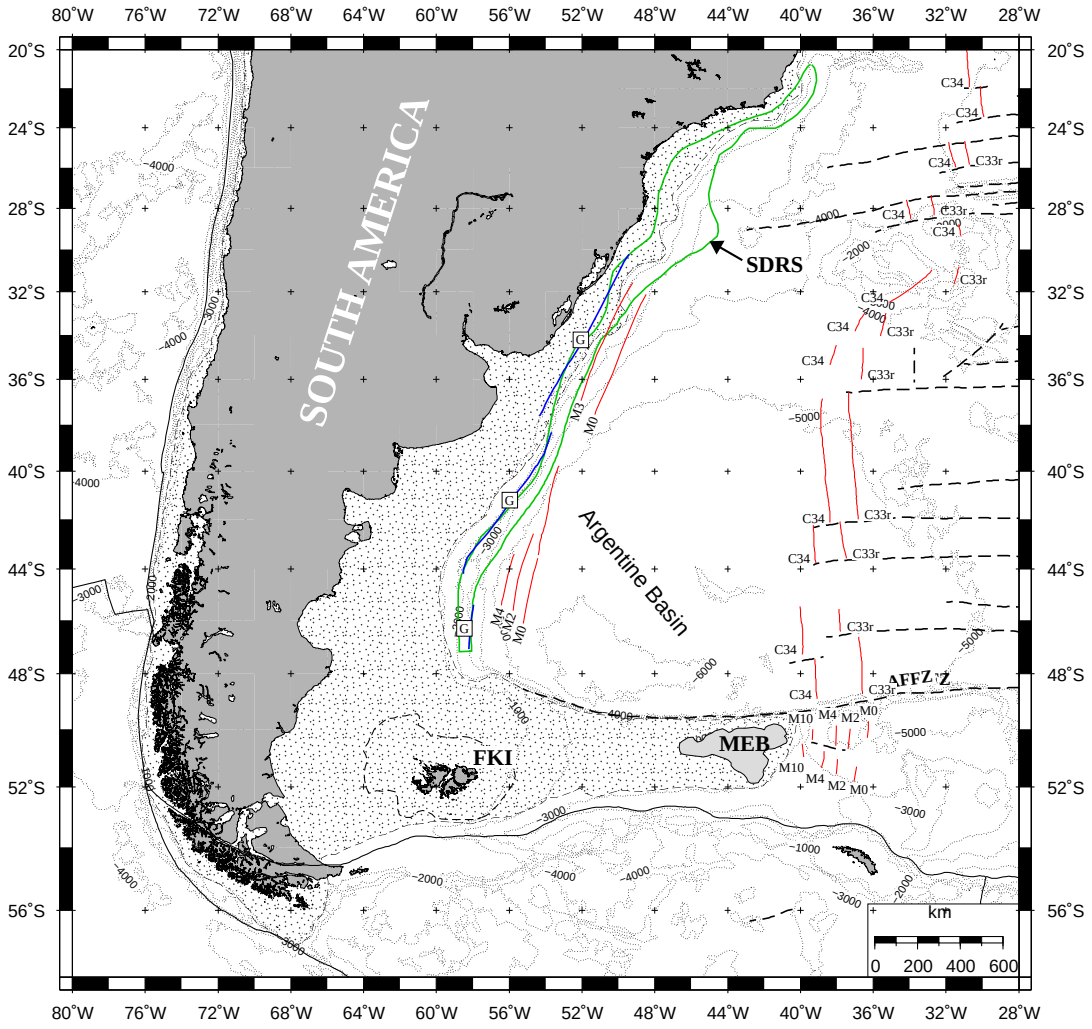

Figure 3.3-12: Magnetic anomaly and fracture zone data off the coast of South America and the Falkland Plateau used to constrain the reconstruction of SAM with respect to AFR. See text for references.

sition (COT) is of crucial importance. Lawver et al. (1998) used the coastal free-air gravity anomaly high as a proxy for the mean position of the COT along the margins of SAM and AFR. This interpretation was adopted here and the outline of the anomaly was digitized from the satellite-derived free-air gravity data set of Sandwell and Smith (1997). The outline of the COTs off the coast of SAM and AFR is shown in figures 3.3-11 and 3.3-12 as a dashed line, and the area residing over continental crust is lightly stippled.

Additionally, where present the occurrence of seaward dipping reflector sequences (SDRS) was used to further constrain the position of the outer and inner parts of the COT. Recent results from the cruises of the German Bundesanstalt für Geowissenschaften und Rohstoffe (BGR) across the continental margins of SAM and AFR show that the landward edge of the SDRS (feather edge) is underlain by stretched

continental crust, as indicated by seismic velocities of 7.2-7.6 km/s (Neben, pers. communication). The oceanward side, on the other hand, occurs over pure oceanic crust. This implies that the outline of the SDRS contains the COT. Along the coast of SAM, the outline of the province of SDRS was digitized from Hinz et al. (1999) (Fig. 3.3-12). On the AFR side of the spreading system, outlines of SDRS provinces were digitized from data presented by Bauer et al. (2000), Hinz et al. (1999) and Gladczenko et al. (1997) (Fig. 3.3-11).

Closing the plate circuit and estimation of accuracies

Total reconstructions for the break-up of Gondwana were determined by searching for the best fitting set of rotations in the three-plate system SAM-AFR-ANT that bring together magnetic anomalies from conjugate ocean basins and maintain the spreading directions indicated by fracture zone data.
The resulting finite rotations are listed in tables C-1 to C-12 in the appendix.

Closure of the plate circuit is maintained and checked for each rotation by independently rotating the southern boundary of the Falkland Plateau via the linked rotations of SAM-ANT-AFR and SAM-AFR with AFR fixed in its present day position. Closure occurs if the calculated finite rotation parameters are the same for both links.
An example of the determination of the final rotation parameters is visualized in figure 3.3-13, for the 125 Ma (M4) reconstruction. While the red line in figure 3.3-13 defines the outline of the Falkland Plateau, rotated with SAM-AFR rotation parameters, the black dashed line shows the position of the southern boundary of the Falkland Plateau obtained by SAM-ANT-AFR rotation. As expected from the calculation of the rotation parameters, both rotations result in an identical position for the southern boundary of the Falkland Plateau. Additionally, the rotated picks of magnetic anomaly M4 (125 Ma) are shown for all ocean basins including the synthetic isochrons for the SAM-ANT spreading system.
Accuracies for the angles of rotation are estimated by visually assessing the fits of conjugate magnetic anomaly picks. Inaccuracies can be seen, for example, in the Georgia Basin and conjugate southern Natal Valley. In the Weddell Sea, inaccuracies in the rotation angles result in misfits between synthetic isochrons and the identified magnetic anomalies (Fig. 3.3-9). From inspection of the fits between rotated conjugate anomaly picks, or synthetic isochrons and picked anomaly data, the maximum spatial error for all stages seems to be less than 25 km or 0.25°.

Finally, the resulting model for the break-up of Gondwana involves not only motions of rigid SAM, AFR and ANT plates but also incorporates intra-continental

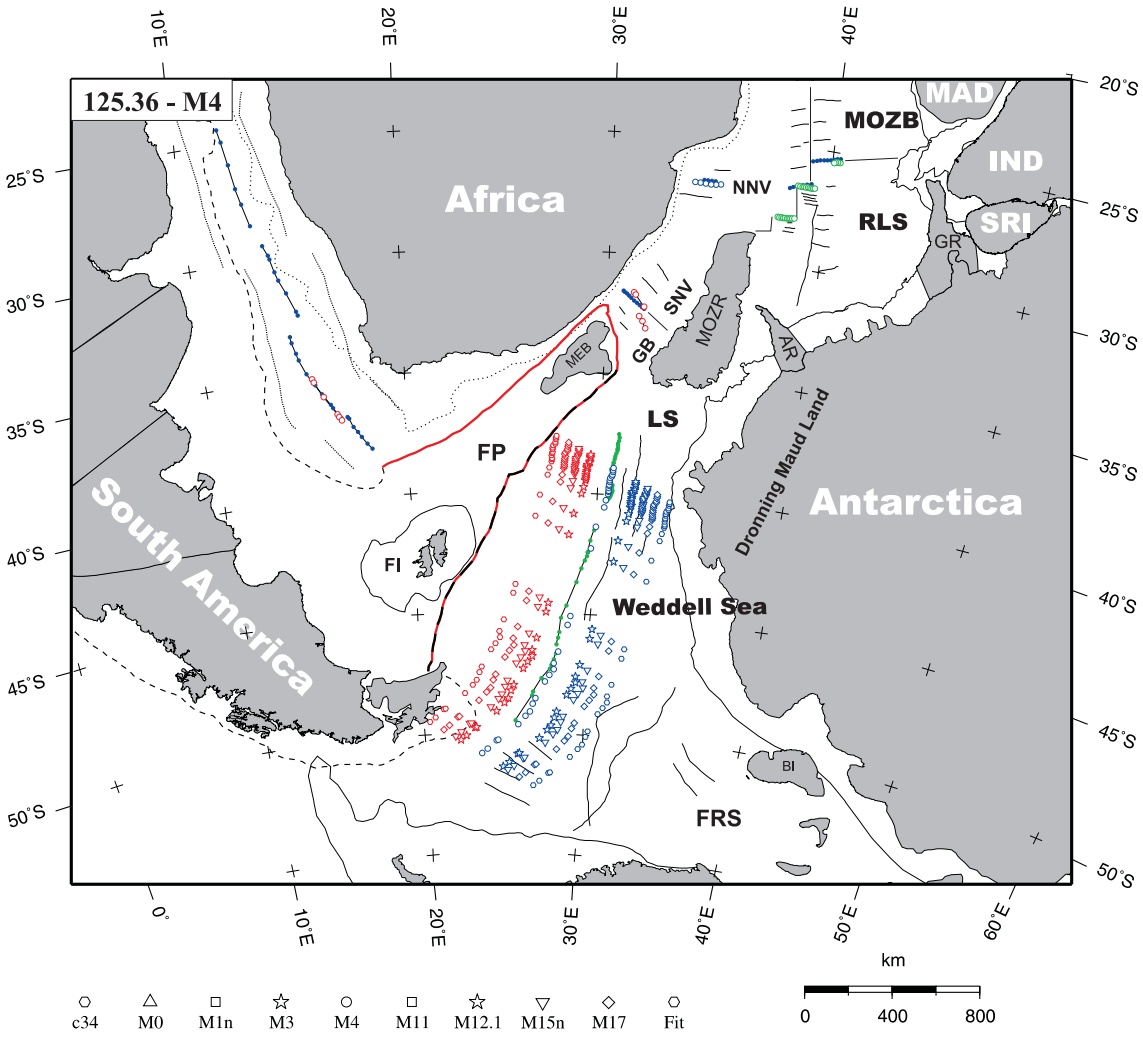

Figure 3.3-13: Example for the determination of best fit total reconstructions for the 3-plate system SAM-AFR-ANT. Red open symbols are rotated anomaly picks on the SAM plate, blue filled symbols are rotated anomaly picks on the AFR plate and green filled symbols are rotated anomaly picks on the ANT plate. The blue open symbols are rotated isochrons on the ANT plate. AFR is fixed to its present-day positon. For a discussion on the fit of the anomalies see the text.

deformations in SAM and the motion of micro-continents or continental fragments like the Antarctic Peninsula and the Mozambique Ridge (see tables C-1 to C-12 for rotation parameters). Where necessary, motions of these smaller elements were adjusted in accordance with the constraints resulting from the motions of the major continents and surrounding ocean basins. If not otherwise mentioned, rotation parameters from other authors are used.

Special attention should be drawn to the rotation parameters for 93 Ma. This time lies within the Cretaceous magnetically quiet zone (C34, 83.0 -118.0 Ma) and cannot be calculated from a fit of seafloor spreading anomalies. However, within this 35

million years of normal polarity, a significant change in spreading direction occurs, as can be inferred from fracture zones seen in satellite gravity data (McAdoo and Laxon, 1997) (Fig. 3.2-3). The pole of rotation used in this model has been adopted from Livermore and Hunter (1996). These authors made an extrapolation of older stage pole parameters to fit the change in direction of flowlines in the Weddell Sea and to infer the age of this significant change in spreading direction. These authors gave their rotation the name 'E' (extrapolated).

In the next chapter, the refined model for the break-up of Gondwana, as defined by the finite rotations listed in the appendix (Tables C-1 to C-12), will be introduced.

3.4 A refined model for the Mesozoic break-up of Gondwana

The new model for the opening of the Weddell Sea and Gondwana break-up is based on the database presented in chapters 3.3.1, 3.3.2 and 3.3.3 and was calculated as described in chapter 3.3.3. The resulting finite rotation parameters are listed in tables C-1 to C-12 in the Appendix. Paleogeographic reconstructions calculated with these rotation parameters are presented in figures 3.4-1 to 3.4-6. The reconstructions show the configuration of the continents and ocean basins at 167.2 Ma, 147.0 Ma, 140.0 Ma, 130.0 Ma, 118 Ma and 83 Ma in a reference frame with AFR fixed in its present day position. These stages cover a sequence of events during the break-up of Gondwana, which begins with rifting between AFR and ANT at about 167.2 Ma and ends after the Falkand Plateau (SAM) cleares the continental margin of AFR at about 100 Ma and a deep water circulation between the South Atlantic and the Indian Ocean is established.
In figures 3.4-7 and 3.4-8, spreading directions and rates for the SAM-ANT and AFR-ANT spreading regimes are shown. These yield valuable information on the dynamics of the plate motions and are referred to in the forthcoming discussion of the different stages of the break-up of Gondwana. The displayed spreading directions and rates were calculated by rotating a point on the well observed magnetic anomaly C34 step-by-step about consecutive stage poles until the closure of the corresponding ocean basin is reached.

Early stages - 167.2 Ma and older
The 167.2 Ma reconstruction (Fig. 3.4-1) shows the configuration of the continents within Gondwana after an initial phase of east-west oriented rifting between AFR and ANT has occured. This is referred to as stage 1 in the break-up of Gondwana by Cox (1992). The existence and timing of this early rifting event is documented in

the occurrence of the north-south oriented Lebombo and Rooi-Rand dyke swarms, parallel to the Lebombo Mountains in southeast Africa. The emplacement of these dykes occurred contemporaneously with the eruption of the Karoo volcanic suite at 183 Ma (Reeves and de Wit, 2000; Storey et al., 2001).

For this time, the position of ANT with respect to AFR is defined by extrapolation of the 155 Ma rotation parameters in the AFR-ANT spreading regime (Figs. 3.4-7 and 3.4-8) until a closure of the Mozambique Basin - Riiser-Larsen Sea is obtained. According to the trend in the spreading direction as seen on figure 3.4-7 for ages younger than 155 Ma and a modelled spreading halfrate of more than 21 mm/yr by Jokat et al. (2003b), the AFR-ANT spreading system is extrapolated using a spreading direction of about 34°E and a halfrate of about 21.5 mm/yr. Further constraints on the relative position of ANT with respect to AFR, before seafloor spreading in the Riiser-Larsen Sea and Mozambique Basin began, are provided by onshore geology. The Archaean Grunehogna Craton in East ANT is interpreted to be a fragment of the Zimbabwe-Kaapval Craton (proto-Kalahari Craton) in south-east AFR for at least Late Mesoproterozoic times (Peters et al., 1991; Jacobs et al., 2003; Jacobs and Thomas, 2004). In late Neoproterozoic-early Paleozoic time (between 650 and 500 Ma), various parts of proto-East and West Gondwana formed the East African-Antarctic orogen by continental collision (Jacobs and Thomas, 2004). The Grunehogna Craton became part of what is today East ANT and remained fixed in its Gondwana position until the beginning of Gondwana break-up (<183 Ma). Maybe during this orogeny, recently described by an Himalayan-type indenter-escape tectonics model by Jacobs and Thomas (2004), a zone of weakness formed in the eastern part of the proto-Kalahari Craton facilitating the complete detachement of the Grunehogna craton during Gondwana break-up (Jacobs and Thomas, 2004). Another anchor for the inital position between AFR and ANT, as shown in figure 3.4-1, is provided by the correlation of the Beatty-Anomaly in southern AFR with the Sverdrupfjella-Kirvanveggen anomaly in ANT (Corner and Groenewald, 1991; Corner et al., 1991). As discussed by Jokat et al. (2003b), both magnetically similar features may belong to the Pan-African (500 Ma) Namaqua-Natal-Maud Belt that is continuous in southern and eastern Africa and parts of Dronning Maud Land (Groenewald et al., 1991).

In the model presented in this thesis, north-south oriented rifting and subsequent seafloor spreading in the Somali Basin and the conjugate Mozambique Basin and Riiser-Larsen Sea began about 15 Ma after the stage 1 rifting between East and West Gondwana occured. The existence of the early rifting event was proposed by Cox (1992). No direct information regarding the exact timing of the onset of

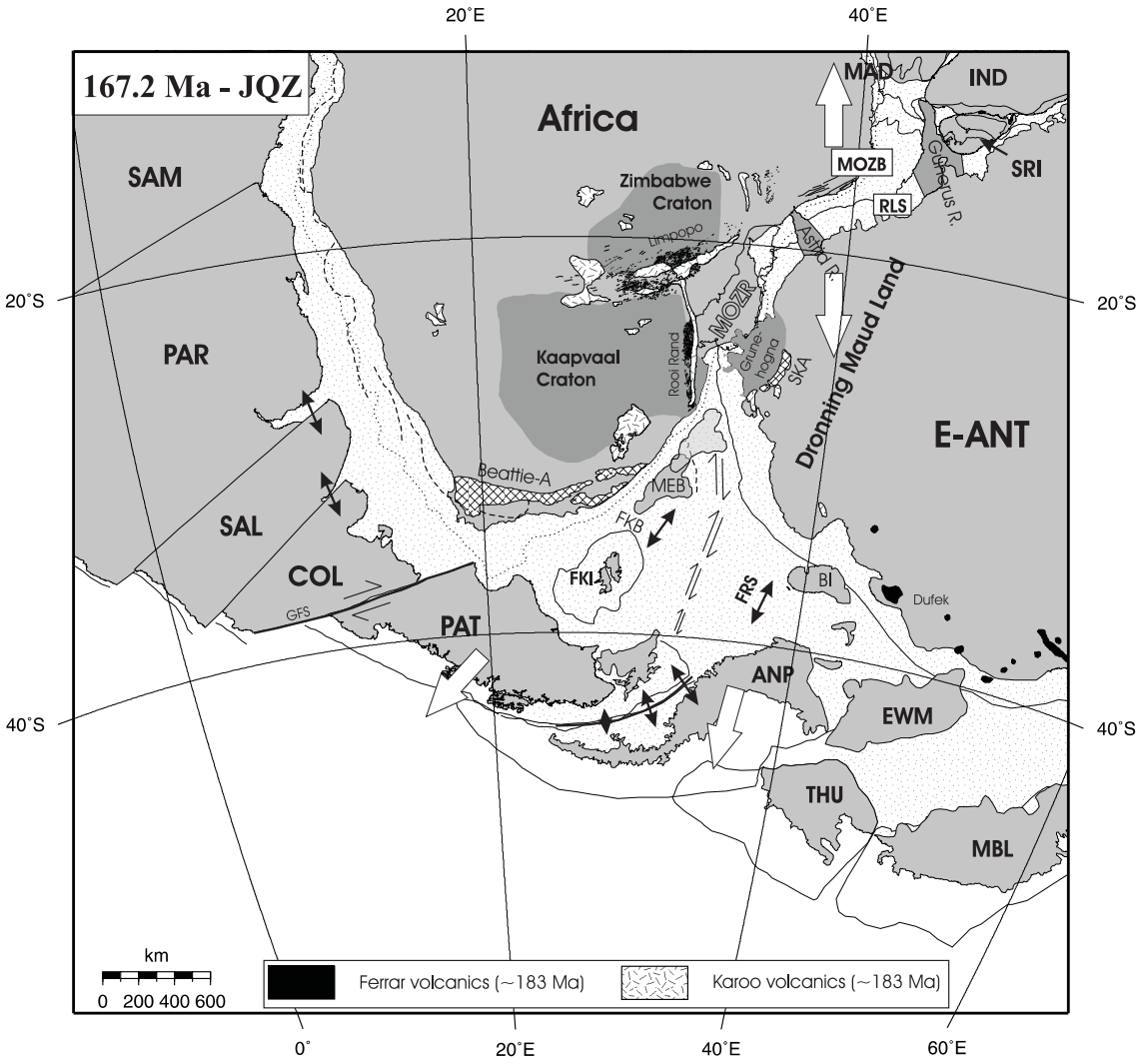

Figure 3.4-1: 167.2 Ma (JQZ) reconstruction for the break-up of Gondwana, showing the situation after initial east-west oriented rifting between Africa and Antarctica and before first north-south directed rifting in the Mozambique Basins - Riiser-Larsen Sea and Somali Basin began (not shown). In this, and all consecutive reconstructions, Africa is fixed in its present day position. A Lambert azimuthal equal-area projection centered on 25°E and 35°S with a scale of 1:37000000 is used. Abbreviations used in this and the following figures 3.4-2-3.4-6: AFFZ: Agulhas Falkland Fracture Zone, AFR: Africa ANP: Antarctic Peninsula AP: Agulhas Plateau, Beattie-A: Beattie Anomaly, C.A.: Central Anomalies (Ferris et al., 2000), COL: Colorado, E-ANT: East Antarctica, EWM: Ellsworth Whitmore mountains, FKB: Falkland Plateau Basin, FKI: Falkland Islands, FRS: Filchner-Ronne Shelf, GFS: Gastre Fault System, IND: India, LZS: Lazarev Sea, MAD: Madagascar, MBL: Marie Byrd Land, MEB: Maurice Ewing Bank, MOZB: Mozambique Basin, MOZR: Mozambique Ridge, MR: Maud Rise, O-A: Orion Anomaly, PAR: Paraná, PAT: Patagonia, RLS: Riiser-Larsen Sea, RV: Rocas Verdes, SAL: Salado, SAM: South America (northern part) SKA: Sverdrupfjella Kirwanveggen Anomaly, SRI: Sri Lanka, THU: Thurston Island;

north-south rifting and the transition to seafloor spreading was available from the data used in this study. However, it is possible to infer the timing of these events given knowledge of the oldest seafloor spreading anomalies in the corresponding

ocean basins. In the Somali Basin, these are dated as M22 (152 Ma) (Segoufin and Patriat, 1980; Cochran, 1988) or possibly even older (M25, 157 Ma), as proposed by Rabinowitz et al. (1983). The oldest magnetic anomaly in the Mozambique Basin - Riiser-Larsen Sea was tentatively dated as M24 (155 Ma) (Jokat et al., 2003b) off the coast of central Dronning Maud Land, giving rise to the suggestion that rifting started in these ocean basins almost simultaneously between 170 Ma and 160 Ma. Jokat et al. (2003b) presented a spreading model for the opening of the Mozambique Basin - Riiser-Larsen Sea, with halfrates between 20-25 mm/yr, from calculation of synthetic anomaly sequences for the Riiser-Larsen Sea. Accordingly, a halfrate of 22 mm/yr was used to extrapolate the AFR-ANT spreading system in the refined model presented here (Fig. 3.4-8). Consequently, rifting in the Mozambique Basin - Riiser-Larsen Sea starts at about 167.2 Ma.

Early stages of stretching and basin development take place in the southwestern corner of Gondwana contemporaneously with initial rifting events between AFR and ANT in the Mozambique Basin and Riiser-Larsen Sea (Fig. 3.4-1). The Antarctic Peninsula (ANP) is moving in a southwesterly direction from a position closer to ANT than today's, which results in highly stretched continental curst beneath the Filchner-Ronne Shelf (Hübscher et al., 1996; Hunter et al., 1996; Leitchenkov and Kudryavtzev, 2000). A ratio of stretched to unstretched crust of 2.5 was used for the Filchner-Ronne Shelf to reconstruct the initial position of ANP with respect to ANT. Stretching factors of 1.5-3.0 are proposed by Hübscher et al. (1996) and Leitchenkov and Kudryavtzev (2000). Rifting between ANP and ANT is accompanied by westward motions of southernmost SAM, namely Patagonia, with respect to AFR and the Maurice Ewing Bank, which results in stretching and extension in the Falkland Plateau Basin (Lorenzo and Mutter, 1988; Marshall, 1994; Platt and Philip, 1995). From a detailed synthesis of single-channel and multi-channel seismic data and interpretation of DSDP borehole data (leg 36 and 71), Lorenzo and Mutter (1988) proposed a crustal extension ratio beneath the Falkland Plateau of 140% - 280%. This ratio has been used to constrain the extension in the Falkland Plateau basin between 167.2 Ma and 130 Ma. An alternative position for the Maurice Ewing Bank within the Falkland Plateau is given for 167.2 Ma (Fig. 3.4-1 light grey), based on a position proposed by Storey et al. (1999). This allows an increased size for any potential continental material in the Falkland Plateau, or for a more easterly Jurassic position of the Falkland Islands as proposed by Adie (1952), Taylor and Shaw (1989), Marshall (1994) and Storey et al. (1999).

Intra-continental deformations in AFR or SAM have to be introduced for reconstructing SAM with respect to AFR, as suggested by Burk and Dewey (1974), Un-

ternehr et al. (1988), Fairhead (1988), Nürnberg and Müller (1991), Lawver et al. (1998) and Macdonald et al. (2003). The necessary deformations are extensions and transcurrent movements, which are attested to by dykes or faults and graben systems on both continents. To portray these complex deformations, SAM is subdivided into four individual blocks, as proposed by Nürnberg and Müller (1991). The sub-plates used by those authors are the (northern) South America sub-plate, the Paraná, Salado, and Colorado sub-plates. Additionally, a Patagonia sub-plate is used, which is bound to the north by the Colorado sub-plate and that moves along the Gastre Fault System (Rapela and Pankhurst, 1992). Since only rough estimates of the possible amount of extension or displacement exist for these movements (Unternehr et al., 1988; Sibuet et al., 1984; Rapela and Pankhurst, 1992), intra-continental deformations in SAM are kept to a minimum throughout this model. In the 167 Ma reconstruction, Patagonia is shifted for 345 km to the east, relative to SAM, to avoid any overlap of the northern tip of ANP onto southernmost SAM or the Falkland Plateau. Dextral transcurrent movements of up to 500 km were already suggested by Rapela and Pankhurst (1992).

Weddell Sea opening - 147.0 Ma

After about 20 million years of stretching and rifting in the Filchner-Ronne Shelf and the Falkland Plateau Basin, the first true ocean floor is created in the southern Weddell Sea at about 147.0 Ma (M20) (Fig. 3.4-2). The pre-drift position of the southern boundary of the Falkland Plateau with respect to the coast of Dronning Maud Land and the Filchner-Ronne Shelf is defined by extrapolation of the rotation parameters for the SAM-ANT spreading system, as explained in the previous chapter 3.3.3 and visualized in figures 3.4-7 and 3.4-8. Polarstern Bank also formed during the initial stages of seafloor spreading, and reflects the general direction of plate motions during this early phase of Weddell Sea opening (Jokat et al., 1996). The strike of this bathymetric high and its associated magnetic anomaly aligns almost perpendicular to the rotated magnetic anomaly C34. The ANP has already reached its present day position relative to east ANT at 147.0 Ma. So far, there exists no unique evidence for or against the argument that stretching in the Filchner-Ronne Shelf occurred at the same time as seafloor spreading in the Weddell Sea. However, stretching continued in the Falkland Plateau Basin until the Lower Cretaceous (Lorenzo and Mutter, 1988). While extensional forces were active in the Falkland Plateau, Patagonia was still subject to forces acting in a westerly direction, resulting in continued dextral shear along the Gastre Fault system (Rapela and Pankhurst, 1992). The position of AFR with respect to ANT at 147.0 Ma is constrained by the close proximity of anomaly M22 (∼152.1 Ma) in the Mozambique Basin and M21 (∼149.7 Ma) in the Riiser-Larsen Sea (Fig. 3.4-2).

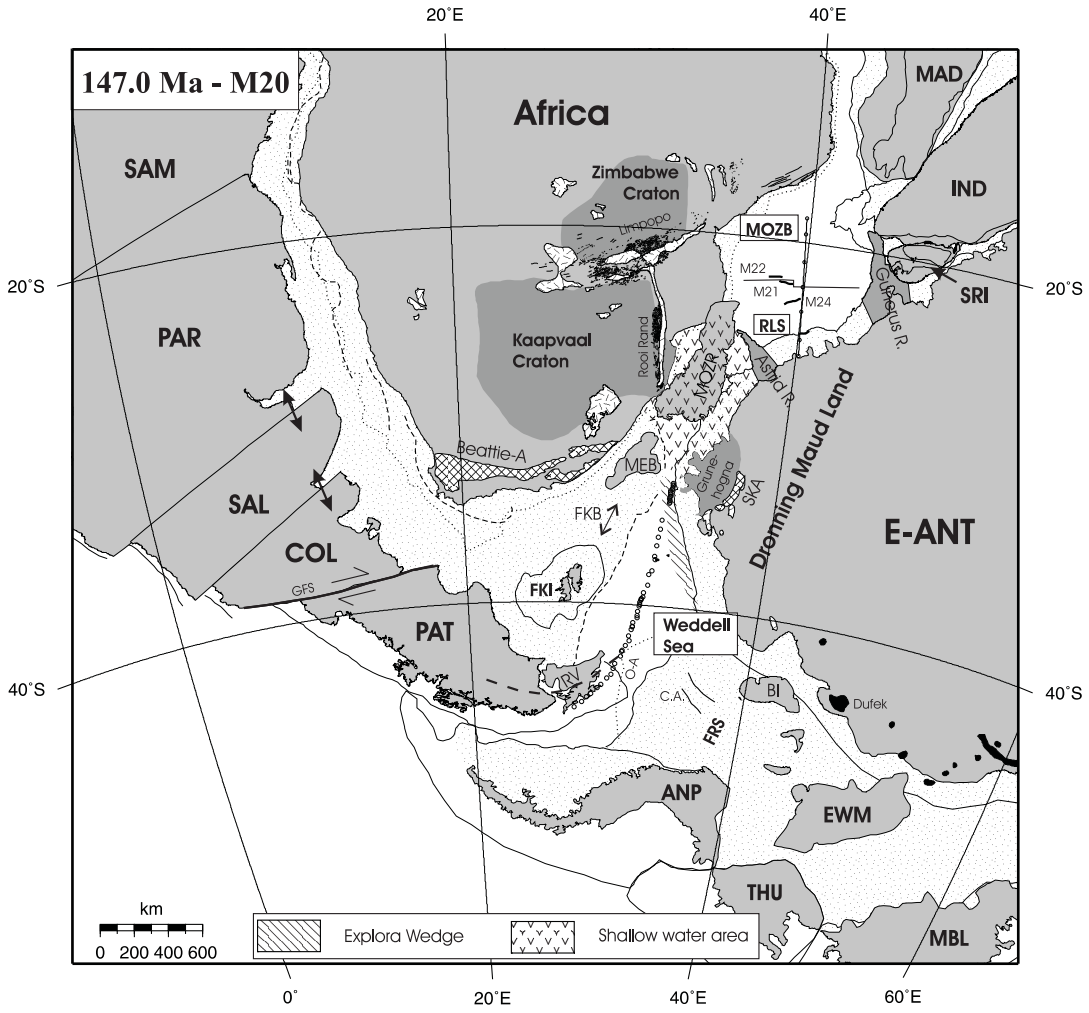

Figure 3.4-2: 147 Ma (M20) reconstruction. Seafloor spreading in the Riiser-Larsen Sea and Mozambique Basin has already begun, with the oldest identified magnetic anomaly north of central Dronning Maud Land identified as M24 (155 Ma) by Jokat et al. (2003b). In the Weddell Sea, rifting between Patagonia and the Antarctic Peninsula created the eastern continental margins of the Antarctic Peninsula. The initial spreading axis in the southern Weddell Sea may have been located in the Rocas Verdes basin in southern Patagonia and propagated eastwards from there to the west coast of Dronning Maud Land. From this time on, there are three separate basins developing independently during the break-up of Gondwana. These basins are the Somali Basin, the Mozambique Basin - Riiser-Larsen Sea, and the Weddell Sea Basin.

Early opening of the South Atlantic Ocean - 140.0-130.0 Ma

The ongoing opening of the Weddell Sea finally leads to the complete development of an east-west oriented spreading system along the coast of western Dronning Maud Land, by ridge-crest propagation from southwest to northeast up to about 10°E (Jokat et al., 2003b). This led to the final separation of SAM and the Falkland Plateau from ANT at around M12 (135 Ma) (Figs. 3.4-3 and 3.4-4). Between AFR and ANT, north-south oriented spreading continued during this time, as defined by magnetic anomalies M16 (141.5 Ma) and M12 (135.8 Ma) in the Mozambique Basin and M16n (140.4 Ma) and M11 (133.1 Ma) in the Riiser-Larsen Sea.

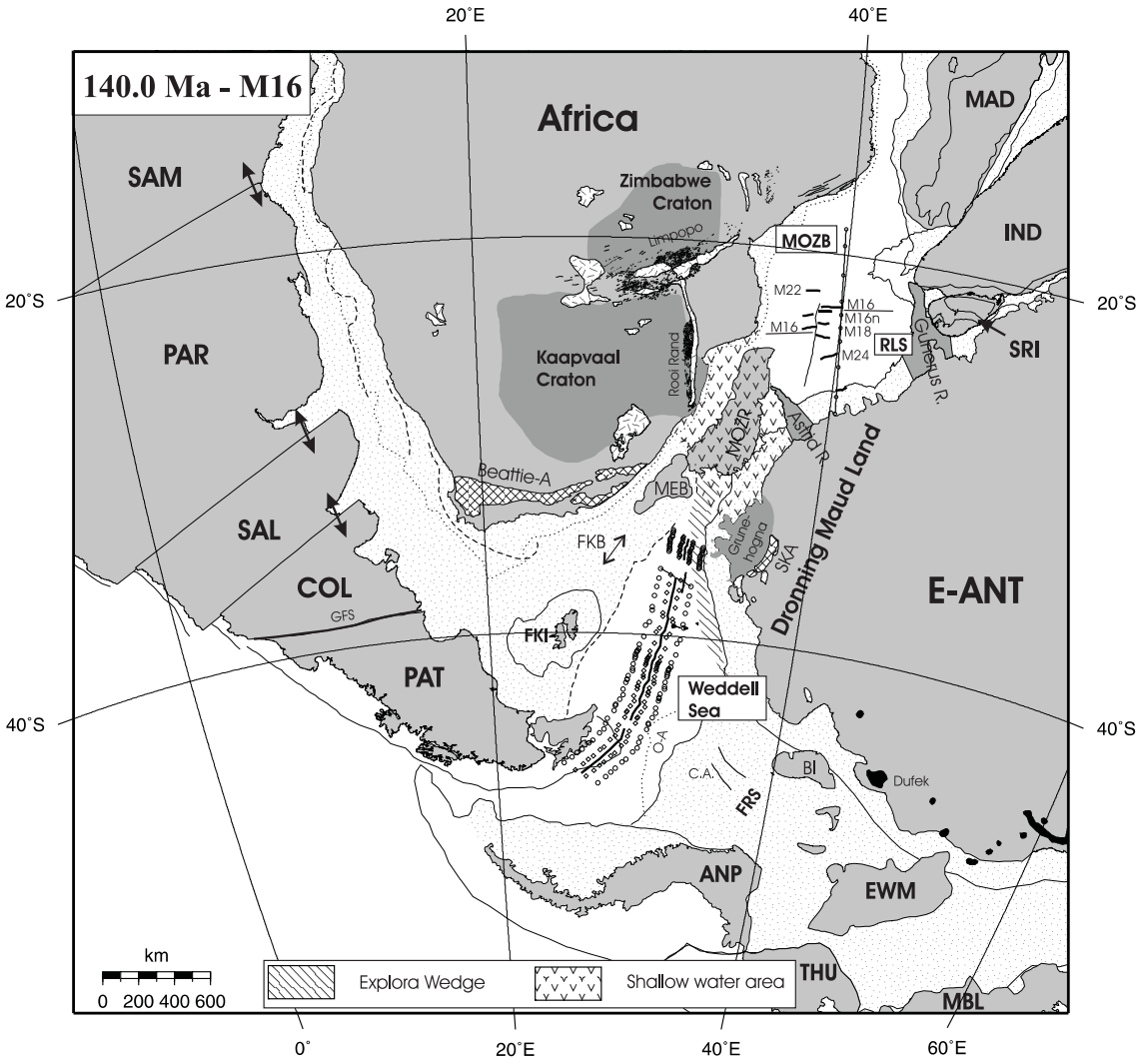

Figure 3.4-3: 140 Ma (M16) reconstruction. Spreading in the Riiser-Larsen Sea and Mozambique Basin continues in an almost north-south direction while the opening of the Weddell Sea occurs in a northwest-southeast direction (in a reference frame with Africa fixed). These differential spreading directions result in a continuous extensional regime between South America and Africa, and also lead to further extension in the Falkland Plateau Basin between the Falkland Islands and Maurice Ewing Bank. No deep ocean connection exists at this time between the Mozambique Basin and the Weddell Sea Basin. The ancient core of the Mozambique Ridge may have prevented any deep water circulation so that only shallow water, or even subaerial conditions, prevailed in what is today the Lazarev Sea.

The final opening of the southern South Atlantic Ocean between SAM and AFR is related to the extrusion of seaward dipping reflector sequences (SDRS) along the volcanic passive margins of SAM and AFR and is shown in the 130 Ma reconstruction in figure 3.4-4 (Gladczenko et al., 1997; Hinz et al., 1999). The occurrence of SDRS correlates with the appearance of Anomaly-G along the coasts of both continents (Rabinowitz and LaBrecque, 1979). In the southern Natal Valley and its conjugate, the Georgia Basin, the first ocean floor was already created by 130 Ma.

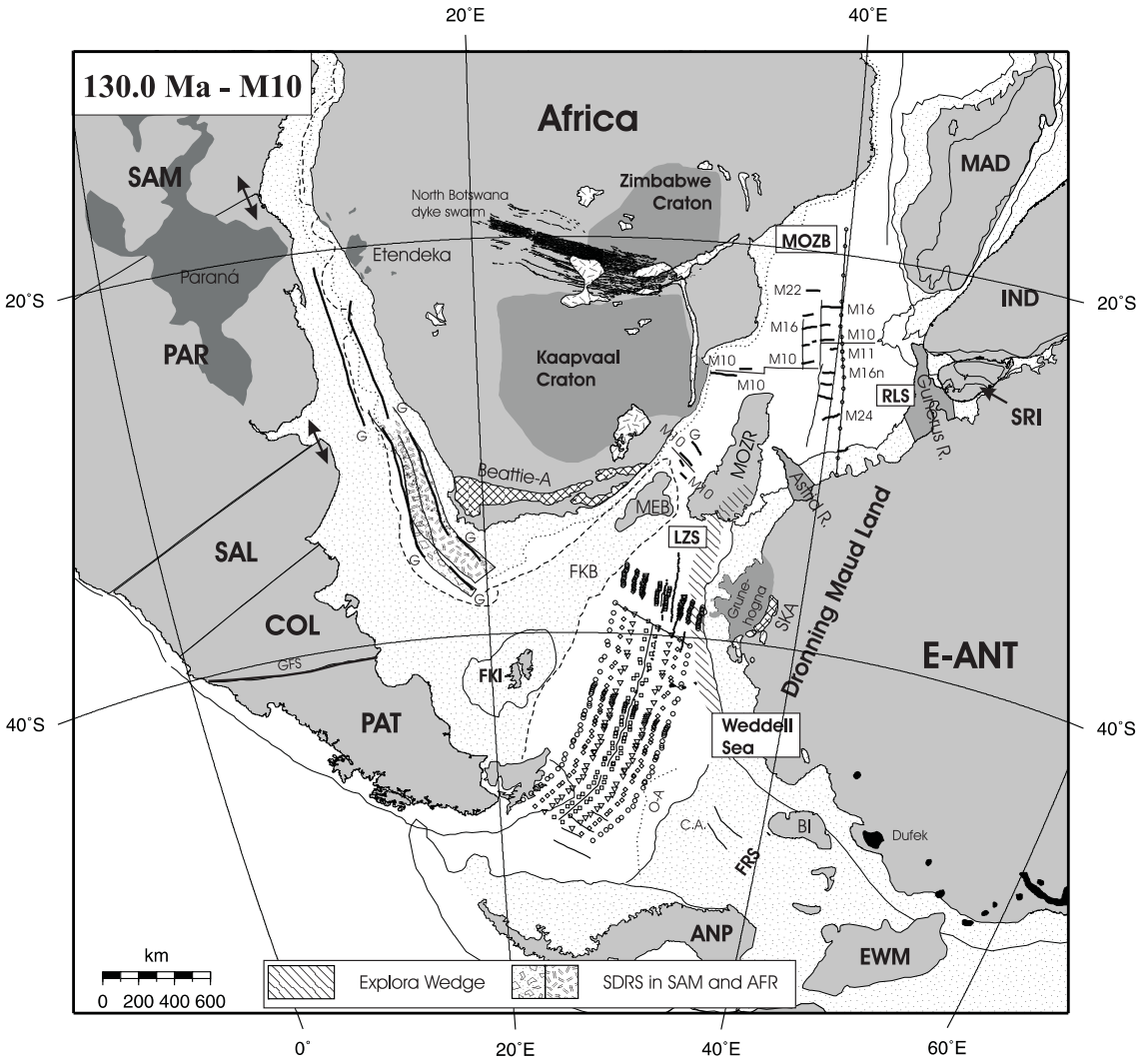

Figure 3.4-4: 130 Ma (M10) reconstruction. While the Riiser-Larsen Sea, Mozambique Basin and Weddell Sea Basin are developing further, the first ocean floor or seaward dipping reflector sequences in the South Atlantic between South America and Africa are formed. Seafloor spreading also started in the southern and northern Natal Valley. Differential movements between Patagonia and the Colorado block in South America are finished, and only further north do intra-continental deformations still take place between the Salado and Paraná blocks and the northern part of South America. The latter movement is related to the emplacement of the Paraná - Etendeka volcanics between 138 Ma and 132 Ma (Courtillot et al., 1999). In the Lazarev Sea, there is still no deep water connection between the southwest Indian Ocean and the Weddell Sea. The Mozambique Ridge is still attached to Antarctica, preventing any deep water passing through from one ocean basin to the other.

Magnetic anomaly M10 (130 Ma) on both continental margins was used to constrain the position of the Falkland Plateau with respect to AFR. The spreading centers between SAM-AFR and AFR-ANT are defined through the rotation of magnetic anomaly C34 (83 Ma) onto older anomalies in the Weddell Sea and the correlation of magnetic anomaly M10 (130 Ma) in the Mozambique Basin with anomaly M11 (133.8 Ma) in the Riiser-Larsen Sea.

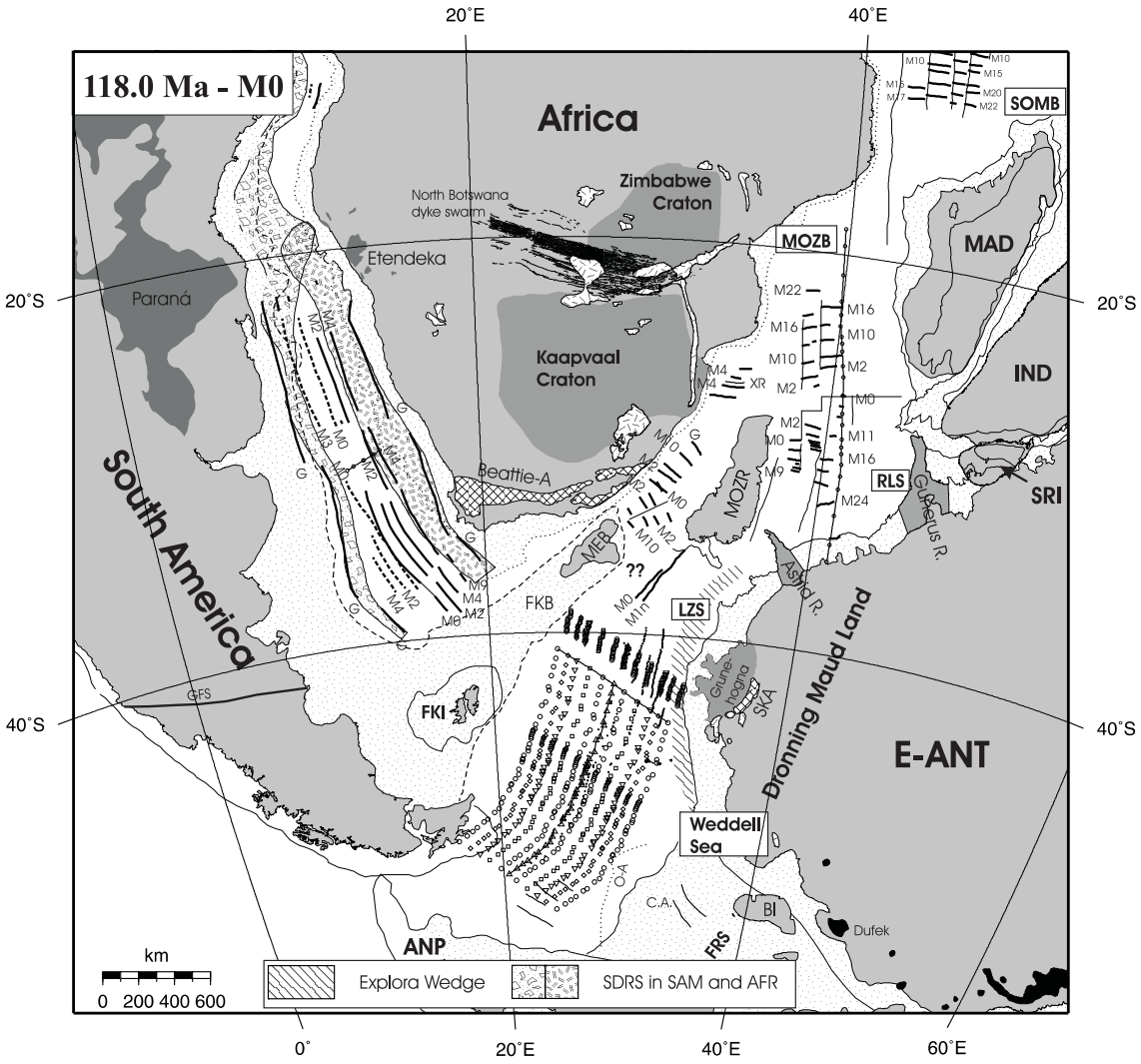

Figure 3.4-5: 118 Ma (M0) reconstruction. The spreading system in the South Atlantic between South America and Africa has developed completely. A deep water connection between the southwest Indian Ocean and the Weddell Sea became established once the Mozambique Ridge cleared the coast of central Dronning Maud Land. Intra-continental deformation in South America is no longer occuring and the Falkland Plateau, including the Falkland Islands and the Maurice Ewing Bank, behaves as a single rigid plate with respect to South America.

Complete opening of the South Atlantic Ocean - 118.0-83.0 Ma

Finally, the reconstructions for 118.0 Ma (M0) and 83.0 Ma (C34) in figures 3.4-5 and 3.4-6 show the ongoing opening of the South Atlantic Ocean. Between 110 Ma and 100 Ma, the Falkland Plateau clears the southwestern tip of AFR and opens a deep water connection between the South Atlantic and the southwest Indian Ocean (Lawver et al., 1992). The Mozambique Ridge has already rifted off the coast of central Dronning Maud Land in the Lazarev Sea (∼122 Ma) and gave the way free for ocean currents to establish between the southwest Indian Ocean and the Weddell Sea. The ocean gateway between SAM and ANP is still closed and probably blocked by the South Orkney block (Lawver et al., 1992).

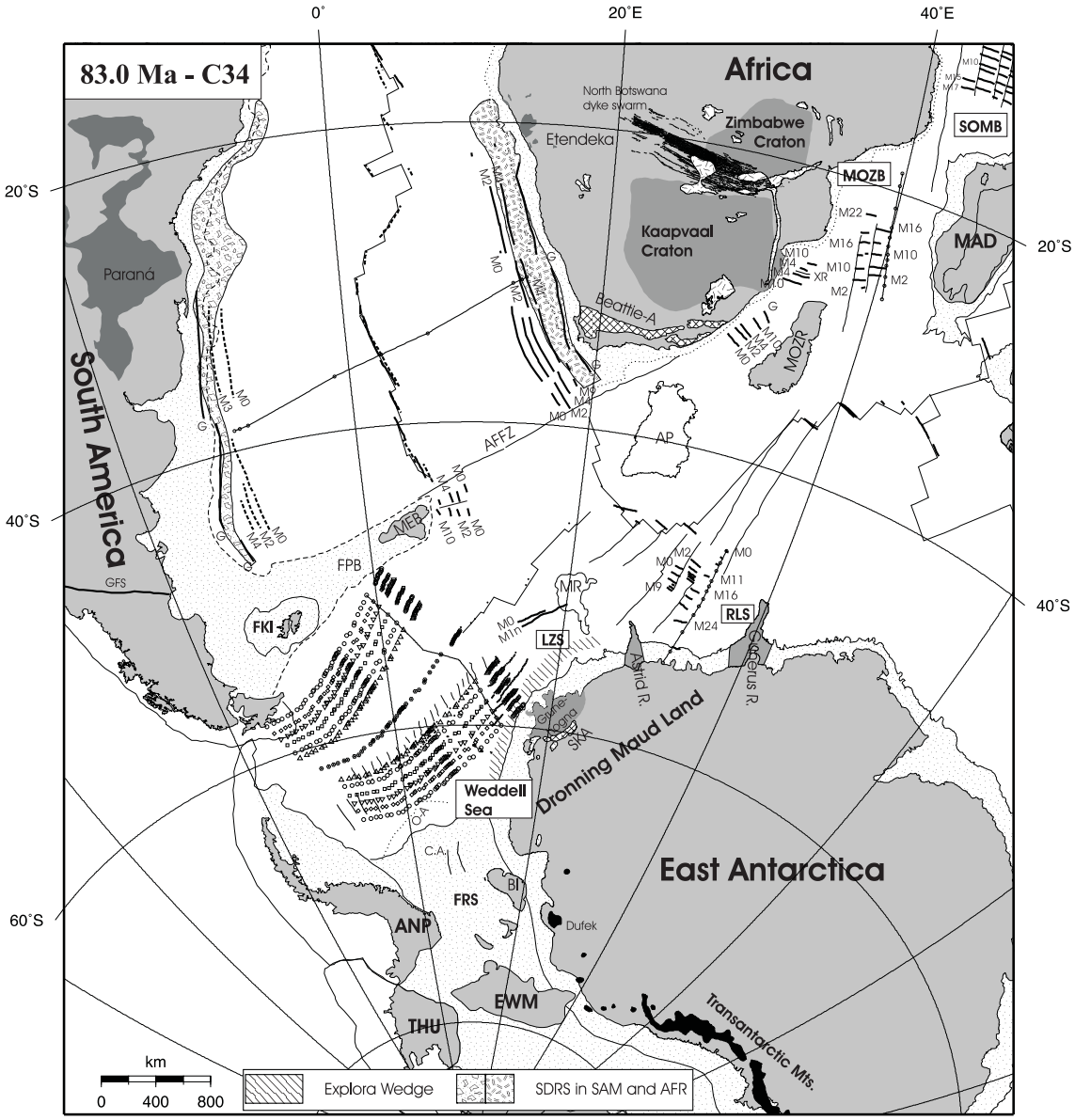

Figure 3.4-6: 83 Ma (C34y) reconstruction of the South Atlantic Ocean and Southwest Indian Ocean. The Falkland Plateau cleared the coast of southernmost Africa and gave way for a deep water connection between the Indian and South Atlantic Ocean. In the Weddell Sea a change in spreading direction occurred between 118 Ma (M0) and 83 Ma (C34) and initiated northwest-southeast directed spreading between South America and Antarctica. A Lambert azimuthal equal-area projection centered on 10°E and 45°S and a scale of 1:42000000 is used for this figure. The outline of the 83 Ma (C34) spreading ridges were deduced from the digital isochrons of the world's ocean floor presented by Müller et al. (1997).

The rotations for the 118.0 Ma and 83.0 Ma reconstructions are well constrained by magnetic anomalies in the Riiser-Larsen Sea and Mozambique Basin, the southern Natal Basin, Georgia, Cape, and Argentine basins. The reconstruction parameters of Martin et al. (1982) and Shaw and Cande (1990) are used to define the relative

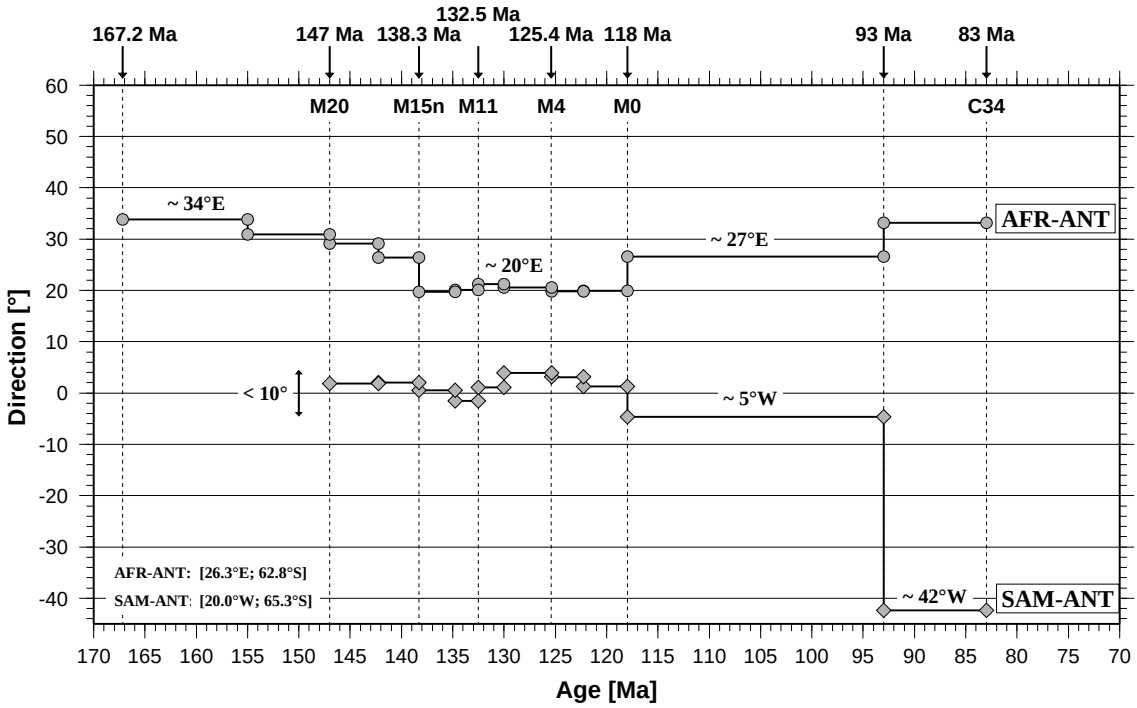

Figure 3.4-7: Spreading directions for the AFR-ANT and SAM-ANT spreading regimes (in an Antarctic reference frame) as calculated for a point on magnetic anomaly C34 that is successively rotated back in time until the closure of the corresponding ocean basin is reached. The almost constant spreading direction in the SAM-ANT spreading system, with a variation of less than 10° between 147 Ma and 93 Ma, is obvious. Spreading in the AFR-ANT spreading regime starts with a direction of about 34°W around 167.2 Ma and successively decreases to about 20°W until 118 Ma (M0). Whereas the SAM-ANT spreading system experiences a dramatic change in spreading direction during the pole change at 93 Ma (Livermore and Hunter, 1996) this change is not that prominent in the AFR-ANT spreading system.

position of SAM with respect to AFR for these ages (see Tables C-1 to C-12 for rotation parameters). These rotations are in good agreement with the constraints for the AFR-ANT and SAM-ANT spreading systems, as deduced from magnetic anomaly data.

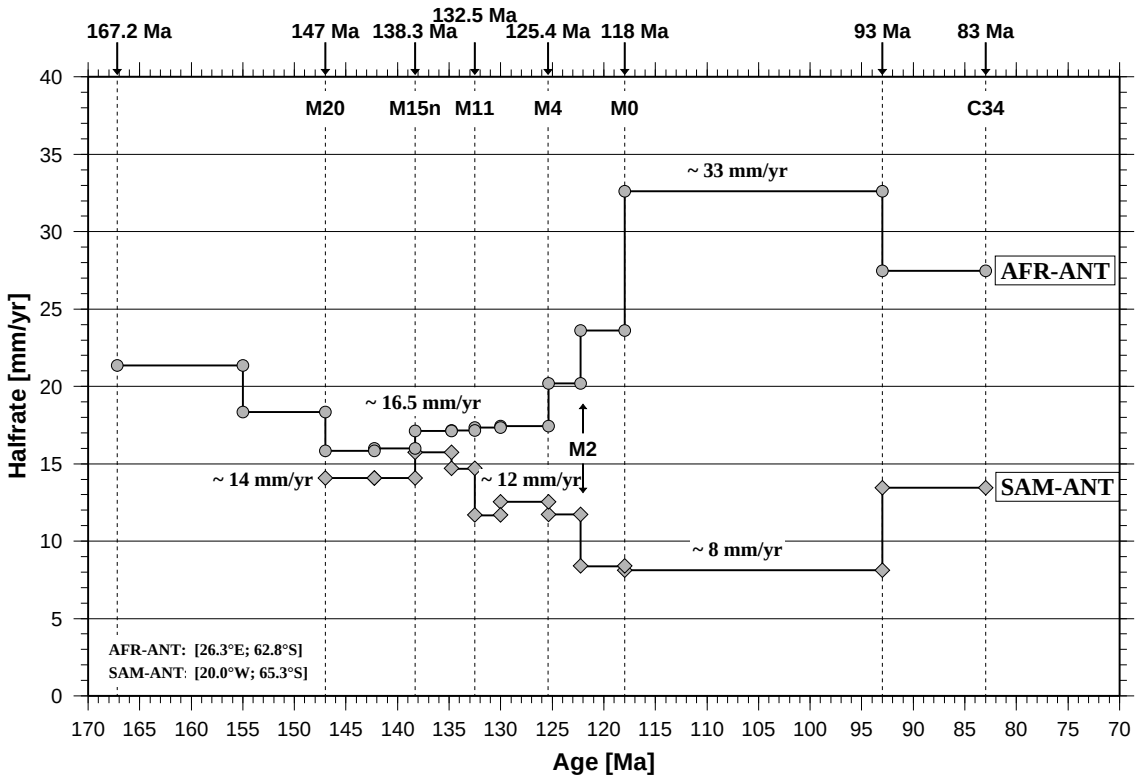

Figure 3.4-8: Spreading rates for the AFR-ANT and SAM-ANT spreading regimes (in an Antarctic reference frame). The calculations are the same as for the spreading directions in figure 3.4-7. Spreading rates in the SAM-ANT regime vary between 12 and 16 mm/yr in the time span from the beginning of seafloor spreading north of the Orion Anomaly until the drop in spreading rate to a value of about 8 mm/yr around chron M2 (122 Ma). This is the age determined for the magnetic expression of Anomaly-T. The 93 Ma change in the pole of rotation also has its expression in spreading rates, with an increase from 8 mm/yr to a value of 13.5 mm/yr. Spreading rates in the AFR-ANT spreading corridor start with a value of about 22 mm/yr, and decrease to about 16.5 mm/yr until M4 (125 Ma). From then on, the rate increases rapidly to about 33 mm/yr for the time span between M0 (118 Ma) and 93 Ma. It should be noted that spreading rates and spreading directions calculated for the time between M0 (118 Ma) and C34y (83 Ma) depend heavily on the time chosen for rotation E.

3.5 Consequences of the new model

The new model for the Mesozoic break-up of Gondwana, as introduced in the previous chapter, has significant consequences on the configuration and movement of the continents and continental fragments during the early stages of Gondwana break-up. In the following paragraph, the key features of this model and their implications on regional tectonics and geology will be discussed in greater detail.

Early movements in the Weddell Sea

Before rifting and seafloor spreading in the Weddell Sea area began (>167.2 Ma, Fig. 3.4-1), Patagonia, the ANP, East ANT and AFR enclosed a basin comprising continental crust of the Filchner-Ronne Shelf, the Falkland Plateau, the Falkland Islands block and the Maurice Ewing Bank. This basin was subject to intense stretching and crustal thinning contemporaneous with the initial stages of north-south oriented rifting between AFR and ANT in the conjugate Mozambique Basin and Riiser-Larsen Sea and between AFR and Madagascar in the Somali Basin. These three basins were developing independently since the early stages of Gondwana break-up and indicate the differential movements of the major continents AFR, ANT and SAM since that time (Jokat et al., 2003b).

Stretching in the Falkland Plateau Basin and the Filchner-Ronne Shelf resulted in an eastward motion of the ANP and southernmost SAM (Patagonia), including the Falkland Islands, away from AFR, the Maurice Ewing Bank and East ANT. Marshall (1994) proposed a continuous north-south striking spreading center being active in the Falkland Plateau Basin and Weddell Sea Basin between 175 - 155 Ma. Although I do not follow this interpretation exactly, a period of combined extension in these two basins during the initial phases of rifting in the Weddell Sea area is suggested. To a lesser degree, but oriented in a more northeast-southwest direction, this extension can be followed to the north where intra-continental deformation between the Colorado, Salado and Paraná sub-plates occurred. This tectonic activity resulted in extension between these blocks and AFR. It could be that the later opening of the South Atlantic Ocean between SAM and AFR was the final result of the same extensional forces that had started to act during the first stages of Gondwana break-up between 170 Ma and 160 Ma.
During this early phase of extension of the Filchner-Ronne Shelf and Falkland Plateau, relative southward motion of ANT was faster than the relative southwestward motion of Patagonia, resulting in dextral-transtensional shear between ANT (i.e. the Filchner Ronne Shelf) and the Falkland Plateau (Fig 3.4-1). In this way, a line of crustal weakness may have formed across the Weddell Sea that was later

reactivated as spreading center between SAM and ANT.
Extension between ANP and Patagonia resulted in rifting and separation of ANT and ANP from the SAM continent shortly before the creation of the first ocean floor in the southern Weddell Sea (Figs. 3.4-1 and 3.4-2). This early separation led to the formation of a non-volcanic rifted margin along the east coast of the ANP (Ghidella and LaBrecque, 1997). The conjugate side, along the west coast of Patagonia, may have been subducted beneath SAM during the Cretaceous as part of a long lasting and still continuing history of subduction along this continental margin. At the time of rifting between ANP and Patagonia (167.2 -140 Ma) the Rocas Verdes Basin had also formed in southernmost SAM (Dalziel and Elliot, 1982). The rotated synthetic 147 Ma (M20) isochron overlaps onto the SAM continent (Fig. 3.4-2), suggesting that this basin may have been the site were the Weddell Sea rift originated. The initial rift propagated eastwards resulting in the formation of the Orion magnetic anomaly (LaBrecque et al., 1986) along the northern limit of the COT in the southern Weddell Sea (Fig. 3.4-2). Further east, along the coast of western Dronning Maud Land, the further propagation of this rift between 150 Ma and 138 Ma led to the extrusion of large volumes of magma to form the Explora Wedge, which can be seen as a sequence of seaward dipping reflectors (SDRS) in seismic data (Hinz, 1981; Hinz and Krause, 1982). Extrusion would have occurred diachronously, from southwest to northeast along the coast of Dronning Maud Land, following the general direction of the opening of the Weddell Sea from southwest to northeast (Jokat et al., 2003b). The age of formation of the SDRS that this model suggests (150 - 138 Ma) conflicts with data published by other authors, and will be discussed in greater detail in the following paragraph.

Explora Wedge and the Karoo - Ferrar large igneous events

The plume-related Karoo and Ferrar volcanism in AFR and ANT is now commonly accepted to have occurred at around 183 Ma (Encarnacion et al., 1996; Duncan et al., 1997; Elliot and Fleming, 2000; Reeves and de Wit, 2000; Storey et al., 2001). Its exact relation, in time and space, to the break-up of Gondwana in the Weddell Sea and the Riiser-Larsen Sea, though, is still a point of discussion (Jokat et al., 2003b). According to Cox (1992) and Elliot and Fleming (2000) the Explora Wedge formed as the conjugate part of the Lebombo monocline that is part of the Karoo volcanics, and assign a similar age to it. This is confirmed by an analysis of regional aeromagnetic data in the southern Weddell Sea of Johnson et al. (1992) and Hunter et al. (1996). These authors estimated the age of the Explora Wedge from a southward continuation of the Explora Anomaly, which is in parts the magnetic expression of the Explora Wedge, across Berkner Island to the Dufek Massif. Using

the dates of intrusions in the Dufek Massif (185 ±2.4 Ma, after Brewer et al. (1996)) and a dolerite sill in Dronning Maud Land (182.1 ±1.9 Ma), Johnson et al. (1992) and Hunter et al. (1996) suggested an approximate age of 182 Ma for the formation of the Explora Wedge.
However, the volcanic sequences in the Weddell Sea have not yet been drilled, and so no definite age for their formation is known.
In this thesis another line of arguments is followed resulting in an approximate age of 150 - 138 Ma for the formation of the Explora Wedge. This is more than 30 million years younger than previously suggested.
According to Hinz (1981) and Mutter (1985), SDRS are formed as precursors to the development of a spreading ridge. A close relation in time between the emplacement of the SDRS and the onset of seafloor spreading has been found along many rifted margins (White and McKenzie, 1989; Courtillot et al., 1999). The best studied SDRS are those of the southeastern margin of Greenland and northwestern margin of Norway at the Vøring Plateau (ODP Legs 152 and 104, respectively). There, direct correlations between the age of drilled sections of SDRS and the estimated onset of seafloor spreading could be made, suggesting a time delay of only 2 to 5 million years (Courtillot et al., 1999). Inferring a similar genesis for the SDRS along the west coast of Dronning Maud Land, and using the magnetic anomaly identifications as presented in this thesis, an age range of 150 to 138 Ma is assumed for their emplacement. This timing post dates the 183 Ma Dufek Massif (Behrendt et al., 1981; Johnson et al., 1992; Hunter et al., 1996) and the emplacement of the Karoo and Ferrar volcanics by more than 30 million years. This leads to the conclusion that there is no direct link between the plume related volcanism in AFR and ANT and the opening of the Weddell Sea and the emplacement of the Explora Wedge, as already noted by Jokat et al. (2003b).

The Explora Escarpment

As the separation of SAM and ANT continues, the Explora Escarpment along the west coast of Dronning Maud Land (Fig. 3.2-1) forms at about 140 - 130 Ma. Lawver et al. (1992) interpret this steep bathymetric step as an expression of early (200-150 Ma) strike-slip movements between East- and West-Gondwana. This interpretation is not supported by the model presented here. From interpretations of seismic data, it is evident that the Explora Escarpment formed after the emplacement of the SDRS (Miller et al., 1990; Kaul, 1991). According to this and the age suggested above for the formation of the SDRS (155-147 Ma), the Explora Escarpment must be more than 10 million years younger than suggested by Lawver et al. (1992). One possible mechanism for the formation of the escarpment that does not

involve large strike-slip motions was put forward by Kaul (1991). In his work, the steep bathymetric step formed along a normal fault during Early Cretaceous times, which would correlate with the final separation of the Falkland Plateau from East ANT.

Anomaly-T

After the Falkland Plateau cleared the coast of Dronning Maud Land, spreading rates in the Weddell Sea dropped to less than 10 mm/yr around magnetic chron M2 (122.3 Ma) (Fig. 3.4-8). Anomaly-T occurs between the identification of magnetic anomalies M1n (118.7 Ma) and M3 (123.0 Ma) in the Weddell Sea (Chapter 3.3.2), suggesting it has an age of about 119 - 123 Ma. Rogenhagen and Jokat (2002) suggest that Anomaly-T may be the expression of the transition between oceanic lithosphere formed at fast and slow spreading rates, according to the interpretation of seismic data that show a smooth basement topography to the south of Anomaly-T and a rough basement topography to the north. Recent studies along the ultraslow Gakkel Ridge in the Arctic and comparative work on the Southwest Indian Ridge provide new interpretations of basement ridges in the vicinity of slow and ultra-slow spreading ridges (Jokat et al., 2003b; Dick et al., 2003). Jokat et al. (2003a) conclude that off-axis basement ridges are common for ocean floor formed at half spreading rates of less than 7 mm/yr. Such basement ridges are interpreted as a result of focused and increased melt supply in the ultraslow spreading regime. In the Weddell Sea, we encounter spreading velocities of 8 mm/yr north of Anomaly-T, which is within the range of ultra-slow rates (<20 mm/yr full rate). Thus, if the increased basement roughness north of Anomaly-T (Rogenhagen and Jokat, 2002) and the observed gravity anomalies are correlated with the existence of basement ridges like those along the Gakkel Ridge and the Southwest Indian Ridge, it could be concluded that Anomaly-T marks a transition between a slow spreading regime to the south and an ultraslow spreading regime to the north.

Mozambique Ridge

The role and position of the Mozambique Ridge during the break-up of Gondwana is of crucial importance for an understanding of how and when the deep water connection between the Southwest Indian Ocean and the South Atlantic Ocean first became established. The Mozambique Ridge forms a large submarine plateau and is composed in part of continental fragments embedded within oceanic crust (Mougenot et al., 1991; Ben-Avraham et al., 1995). However, its pre-break-up position and subsequent kinematic history is only sparsely known (Ben-Avraham et al., 1995; Tikku et al., 2002). From a detailed study of satellite-derived free-air gravity data and

shipborne magnetic data, Tikku et al. (2002) inferred an extinct spreading center in the northern Natal Valley, which was active in separating the Mozambique Ridge from AFR between M11 (133.0 Ma) and 125.3 Ma. The poles of rotation from this study and a pre-drift position of the Mozambique Ridge as presented by Marks and Tikku (2001) were combined with the model parameters presented in this thesis (Tables C-5) and correlated with the relative positions of AFR and ANT through time.

The possible position of the Mozambique Ridge shown in the pre-drift reconstruction (167.2 Ma, Fig. 3.4-1) is that proposed by Marks and Tikku (2001). For this and the following reconstructions, the outline of the maximum size of the continental core of the Mozambique Ridge, as inferred from free-air gravity data (Sandwell and Smith, 1997), is used. The configuration shown in figure 3.4-1 implies, on the one hand, that the Mozambique Ridge behaved as an independent microplate even prior to the existence of the extinct spreading ridge in the northern Natal Valley and, on the other hand, that a significant amount of extension in central Mozambique and onshore Dronning Maud Land occurred prior to the separation of AFR and ANT. Both these requirements were discussed by Marks and Tikku (2001), Cox (1992) and Tikku et al. (2002).

For the 147 Ma, 140 Ma, and 130 Ma reconstructions (Figs. 3.4-2, 3.4-3 and 3.4-4), the position of the Mozambique Ridge was interpolated and adjusted from the reconstructions of Marks and Tikku (2001), and Tikku et al. (2002). As shown in figures 3.4-2-3.4-4, the Mozambique Ridge fits almost exactly in the gap between the Maurice Ewing Bank to the west and the Astrid Ridge to the east. Both these features are assumed to consist, at least partially, of a continental core (Ludwig, 1983; Roeser et al., 1996) and hence would have formed, together with the Mozambique Ridge, a continuous barrier to deep water circulation between the Indian Ocean and the Weddell Sea at this time. Mutterlose and Wise (1990) presented evidence for anaerobic to dysaerobic bottom water conditions on the continental slope north of Dronning Maud Land during Valanginian-Hauterivian (138 - 124 Ma) times from analyses of Lower Cretaceous nannofossils in cores from ODP Leg 113. Accordingly, Jokat et al. (2003b) suggested the existence of a shallow water or even subaerial basin between AFR and ANT at about 145 Ma. The proposed position of the Mozambique Ridge at 147-130 Ma supports this interpretation, assuming rifting and seafloor spreading was active in the Mozambique plain and the northern Natal Valley at least since at about 147 Ma.

According to Tikku et al. (2002), seafloor spreading in the northern Natal Valley stopped at about 125.3 Ma. Thus, in the 118 Ma reconstruction (Fig. 3.4-5), the Mozambique Ridge is shown in its present day position with respect to AFR. By this time, the ridge had rifted of the coast of Dronning Maud Land and was mov-

ing away from it in a northeasterly direction. Although there is no direct evidence for the exact age when the Mozambique Ridge and ANT separated, indirect hints come from an interpretation of magnetic anomalies in the Lazarev Sea (Jokat et al. (2003b) and figure 3.3-4). If the lineated east-west striking magnetic anomalies in the Lazarev Sea are interpreted as anomaly M0 (118 Ma) and M1n (118.7-121.8 Ma), as suggested by Jokat et al. (2003b), the Mozambique Ridge must have cleared its position in the Lazarev Sea by 122.0 Ma, in agreement with the 118 Ma reconstruction shown in figure 3.4-5. However, some uncertainty still exists about the configuration of the ridge systems that were active in the Lazarev Sea at this time (area marked by "?" in figure 3.4-5). Based on the east-west strike of the magnetic anomalies in the Lazarev Sea, conjugate seafloor spreading anomalies would be expected south of the Maurice Ewing Bank, but this ocean floor no longer exists due to subduction at the South Sandwich trench. Rifting between the Mozambique Ridge and ANT should have formed seafloor spreading anomalies parallel to the ridge axis in a northeast-southwest direction. However, only sparse data exist in these regions, and no such seafloor spreading anomalies could so far be identified in the eastern Lazarev Sea, or south of the Mozambique Ridge. Maybe any mangetic anomalies in the eastern Lazarev Sea are overprinted by the large Maud Rise complex.

The new model compared to other published data

Compared to other published models, the model for the opening of the Weddell Sea, as presented in this thesis, is constrained by unequvocally dated mangetic anomaly identifications and puts strong constraints on the age of the oldest ocean floor in the southern Weddell Sea. The deduced Gondwana break-up model has major differences and improvements compared to the models introduced in chapter 3.1. An overview of the most significant differences and improvements is given below:

⇒ Lawver et al. (1992)
In the Gondwana break-up reconstructions of Lawver et al. (1992), the earliest movements in the Weddell Sea are described as a consequence of north-south oriented movements between rigid East- and West-Gondwana plates. This entails simple strike-slip motions along the western coast of Dronning Maud Land and in the southern Weddell Sea. Large strike-slip motions between rigid East- and West-Gondwana are not encountered in the new model presented in this thesis. Stretching and extension takes place in the Weddell Sea Basin and between SAM and AFR since the early stages of Gondwana break-up, which rules out the assumption of two rigid (East- and West-)Gondwana plates.

⇒ Ghidella et al. (2002)
Spreading directions proposed in the model of Ghidella et al. (2002) are very

similar to those presented in this model. However, Ghidella's 146 Ma and 160 Ma reconstructions were only tentatively dated due to weak constraints on the age of the oldest ocean floor. These dates are revised in the new model presented here by about 13 million years, suggesting an age of 147 Ma for the oldest ocean floor in the southern Weddell Sea.

⇒ Livermore and Hunter (1996)
In the same way, the age for the initiation of seafloor spreading, as presented by Livermore and Hunter (1996), differs by 18 Ma from the one presented here. Similarly to Lawver et al. (1992), these authors assume rigid East- and West-Gondwana motions for the early stages of Gondwana break-up, which is not supported by the new model.

⇒ Kovacs et al. (2002)
The timing and position of the initial phase of separation between SAM and ANT in the Weddell Sea, as presented by Kovacs et al. (2002), is similar to that presented here. However, no evidence can be found in the high resolution magnetic anomaly data along the coast of western Dronning Maud Land for the suggested subsequent phase of east-west oriented spreading. The constant spreading directions shown in figure 3.4-8 agree with the east-west directed strike of the magnetic anomalies shown in figure 3.3-4 and exclude a sudden change in spreading direction at any time during the opening of the Weddell Sea.

⇒ Jokat et al. (2003b)
While Jokat et al. (2003b) concentrate on the presentation and interpretation of the new magnetic anomaly data in the eastern Weddell Sea, Lazarev Sea and Riiser-Larsen Sea, in this thesis, the interpretation of magnetic anomalies in the Weddell Sea is extented further west by the correlation with other published data from the western and central Weddell Sea. In the paper of Jokat et al. (2003b), the newly derived model for the break-up of Gondwana describes any movements in the Weddell Sea area between SAM and ANT only as far as they can be directly deduced from the newly presented magnetic database. The model presented here is a continued and refined model of the one presented by Jokat et al. (2003b) including a detailed description of the early movements in the Weddell Sea area shortly before and during the inital stages of Gondwana break-up.

3.6 Summary

Precise knowledge about the plate tectonic processes involved in the opening of the Weddell Sea is crucial for any Gondwana break-up reconstruction dealing with the early separation between Africa, Antarctica, and South America. However, until recently, details about timing and geometry of rifting and early drifting in the Weddell Sea were still not known.

Significant contributions to unravel these open questions were provided by the East Antarctic Margin Aeromagnetic and Gravity Experiment (EMAGE), carried out by the Alfred-Wegener Institute between 1996 and 2002. Within this project, a high-resolution aeromagnetic dataset was acquired in the eastern Weddell Sea, the Lazarev Sea, and the Riiser-Larsen Sea. One of the results of this extensive aero-geophysical project is a detailed age model for the ocean floor north of western Dronning Maud Land, a region where the separation between South America and Antarctica occurred.

In this thesis, the compilation of a magnetic anomaly map based on the EMAGE dataset was presented. Together with additional profile data from the central and western Weddell Sea and the unequivocal age constraints for the ocean floor north of western Dronning Maud Land, magnetic anomaly identifications were made across the Weddell Sea as far west as 45°W. Assuming symmetric spreading between South America and Antarctica and using the ages and strike of the identified magnetic anomalies, a new set of rotation parameters describing the opening of the Weddell Sea was calculated. In contrast to other published models, the ages of the magnetic anomalies used for this model are much better constrained resulting in a more precise reconstruction of the opening between South America and Antarctica. Through the combination with further constraints from the other ocean basins in the region of the South Atlantic Ocean, a refined model for the Gondwana break-up was calculated with special emphasis on the processes being active in the southwestern corner of Gondwana.

In this, model parameters are provided already for the earliest movements taking place in the Weddell Sea region while Africa and Antarctica start to separate. This includes extensional movements between the Antarctic Peninsula and the east Antarctic craton between 167 Ma and 147 Ma, and within the Falkland Plateau, separating Patagonia from Africa and the Maurice Ewing Bank. Extensional forces between South America and Africa are already active in the Weddell Sea region at the same time when rifting in the conjugate Mozambique Basin and Riiser-Larsen Sea, and the Somali Basin occurred. Thus, there were three separate basins, the Weddell Sea, Mozambique Basin and Riiser-Larsen Sea, and the Somali Basin, developing independently at this time.

The continental margin along the east coast of the Antarctic Peninsula probably

formed during those initial stages of Gondwana break-up as a result of rifting between the Antarctic Peninsula and Patagonia. The opening of the Weddell Sea starts at around 147 Ma in the southernmost part of the Weddell Sea. This is 10 to 15 million years later than previously suggested by other published models. As a consequence of this revised age for the opening of the Weddell Sea, an age of about 150 Ma to 138 Ma is suggested for the formation of the seaward dipping reflector sequences, the Explora Wedge, along the west coast of Dronning Maud Land. This, in fact, excludes the previously suggested correlation of the volcanic sequences with the plume-related Karoo volcanism (large igneous event) that occurred at about 183 Ma. The gap of more than 30 million years between both events makes any direct link rather unlikely. After the formation of the Explora Wedge the initial opening in the southern Weddell Sea starts in a NNW direction at slow spreading rates (∼12-14 mm/yr) and drops down to ultra-slow spreading rates at about 122 Ma (M2). The transition from a slow to an ultra-slow spreading regime caused the formation of Anomaly-T, an east-west striking linear free-air gravity anomaly and is clearly expressed as a step in the spreading rates in the new model for the opening between South America and Antarctica.
In the Gondwana break-up model presented in this thesis, possible movements of the Mozambique Ridge are verified. The assumption that the Mozambique Ridge once acted as an independent continental fragment was used to infer its position throughout the complete Gondwana break-up process. Thereafter, the development of a deep water connection between the Indian and the South Atlantic Ocean occurced not before 122 Ma. Before this time the Mozambique Ridge, Astrid Ridge and the Maurice Ewing Bank formed a continental barrier between the oceans in the west and in the east. Uncertainties, however, exist about the origin and the initial position of the Mozambique Ridge within Gondwana and the precise date and geometry of its separation from the Antarctic continent.

For a further improvement of the refined Gondwana break-up model, investigations should be undertaken on- and offshore South America to get more precise information on the amount, direction and age of any possible intra-continental deformations related to the opening of the South Atlantic Ocean. This would put stronger constraints on the fit between South America and Africa and the early movements in the Weddell Sea area and thus significantly enhance the understanding of the processes being active during the initial stages of Gondwana break-up and the opening of the South Atlantic Ocean.

4 Outlook

In the first part of this thesis the ship-mounted magnetometer system onboard RV *Polarstern* was introduced. It was shown that at quiet sea conditions the raw magnetometer data can be corrected to an accuracy of 20 nT at a horizontal resolution of about 150 m. This is sufficient for the identification of magnetic seafloor spreading anomalies as present in the world's ocean basins.

From this, further applications arise for the usage of this magnetometer system. As an example a recently accomplished expedition to the Scotia Sea will be briefly introduced and possibilities for the extension of the existing EMAGE dataset in the Lazarev Sea will be shortly discussed.

At the end of the austral summer 2005 an expedition to the central Scotia Sea was carried out with RV *Polarstern*. The scientific program was aimed to investigate the ocean floor, its age and deeper crustal structure by the means of magnetic, gravimetric and bathymetric measurements. Magnetic measurements were carried out onboard the ship using the ship-mounted magnetometer system and by the application of helicopters. Since, in this region, seafloor spreading anomalies are expected to strike in north-south as well as in east-west direction flight lines and ship track lines were planned perpendicular to each other. After three weeks of intensive measurements on a 6×5 km network of profiles and a first processing onboard the ship, as described in chapter 2.4, a combined high-resolution helicopter- and shipborne magnetic anomaly map could be compiled for the region under investigation. The preliminary results from this expedition confirm the results of this thesis that the ship-mounted magnetometer system and the presented processing procedure can be used for the evaluation of magnetic anomaly data acquired even in rough seas and that this data can be used for geoscientific interpretations. Furthermore, this expedition demonstrates that helicopterborne measurements can be significantly enhanced by the application of a ship-mounted magnetometer system.

Another dataset that can be significantly extended by the repeated usage of the ship-mounted magnetometer system is the EMAGE dataset in the Lazarev Sea. As reported in chapter 3.5, there is still doubt about the precise age of the ocean floor in the Lazarev Sea. No continuous lines exist that connect, for example, the well known magnetic anomaly C34 further north with the lineated anomalies in the south. By

use of the ship-mounted magnetometer system, this data gap can be closed at a minimum of additional expedition time. On its way to the German overwintering station Neumayer, RV *Polarstern* crosses this region at least once a year on more or less north-south oriented profiles. Through the parallel adjustment of these crossings a set of profiles covering the desired region can be acquired within a relatively short period of time adding crucial information on the plate tectonic processes being active during the separation between Africa and Antarctica.

The above presented examples point out some of the possibilities and advantages of the ship-mounted magnetomer system and show that the system is a powerful tool that can be used in a wide area of geoscientific problems.

References

Adie, R. J. (1952). *The position of the Falkland Islands in a reconstruction of Gondwanaland*, Geological Magazine **89**: 401 – 410.

Anderson, D. Z. (1986). *Optische Gyroskope*, Spektrum der Wissenschaft **6**: 68 – 74.

Auster, H. U., A. Lichopoj, J. Rustenbach, H. Bitterlich, K. H. Fornacon, O. Hillenmaier, R. Krause, H. J. Schenk and V. Auster (1995). *Concept and first results of a digital fluxgate magnetometer*, Measurement Science and Technology **6**: 477 –481.

Auster, H. U., K. H. Fornacon, V. Auster, O. Hillenmaier, R. Kroth and A. Best (1998). *Progress in the development of digital fluxgate magnetometers*, Revista Geofisica **48**: 121 – 131.

Auster, V. (1961). *Vorschläge zur Bestimmung der Deviationskoeffizienten mit einem Drei-Komponenten-Meßgerät*, *Abhandlung Nr. 27 des Geomagnetischen Instituts Potsdam*, Geomagnetisches Observatorium Potsdam, Germany.

Auster, V. (1964). *Ein Drei-Komponenten-Meßgerät zur Bestimmung der Deviationskoeffizienten*, *Jahrbuch des Adolf-Schmidt-Observatoriums Niemegk*, Adolf-Schmidt-Observatorium, Berlin, Germany, pp. 102 – 109.

Auster, V. and K. Lengning (1963). *Einige Bemerkungen zur Deviationstheorie*, *Jahrbuch des Adolf-Schmidt-Observatoriums*, Adolf-Schmidt-Observatorium, Berlin, Germany.

Barker, P. F. (1979). *The history of ridge-crest offset at the Falkland-Agulhas Fracture Zone from a small-circle geophysical profile*, Geophysical Journal of the Royal Astronomical Society **59**: 131 – 145.

Barker, P. F. and R. A. Jahn (1980). *A marine geophysical reconnaissance of the Weddell Sea*, Geophysical Journal of the Royal Astronomical Society **63**: 271 – 283.

Bauer, K., S. Neben, B. Schreckenberger, R. Emmermann, K. Hinz, N. Fechner, K. Gohl, A. Schulze, R. B. Trumbull and K. Weber (2000). *Deep structure of the Namibia continental margin as derived from integrated geophysical studies*, Journal of Geophysical Research **105** (B11): 25829 – 25853.

Behrendt, J. C., D. J. Drewry, E. J. Jankowski and M. S. Grim (1981). *Aeromagnetic and radio echo ice-sounding measurements over the Dufek Intrusion, Antarctica*, Journal of Geophysical Research **86**: 3014 – 3020.

Bell, R. E., J. Brozena, W. Haxby and J. L. LaBrecque (1990). *Continental margins of the western Weddell Sea: Insights from airborne gravity and GEOSAT derived gravity*, in: Hayes, D. E. (ed.), *Contributions to Antarctic Research I*, Vol. 50 of *Antarctic Research Series*, American Geophysical Union, Washington, DC, USA, pp. 91 – 102.

Ben-Avraham, Z., C. J. H. Hartnady and A. P. le Roex (1995). *Neotectonic activity on continental fragments in the southwestern Indian Ocean: Agulhas Plateau and Mozambique Ridge*, Journal of Geophysical Research **100** (B4): 6199 – 6211.

Bergh, H. W. (1977). *Mesozoic seafloor off Dronnig Maud Land, Antarctica*, Nature **269**: 686 – 687.

Bidlingmaier, F. (1925). *Der Doppelkompaß, seine Theorie und Praxis*, Deutsche Südpolar-Expedition 1901-03, Bd. V, Teil I, Berlin, Germany.

Blakely, R. J., A. Cox and E. J. Iufer (1973). *Vector magnetic data for detecting short polarity intervals in marine magnetic profiles*, Journal of Geophysical Research **78**: 6977 – 6983.

Brewer, T. S., D. Rex, P. G. Guise and C. J. Hawkesworth (1996). *Geochronology of Mesozoic tholeiitic magmatism in Antarctica: Implications for the development of the failed Weddell Sea rift system*, in: Storey, B. C., E. C. King and R. A. Livermore (eds), *Weddell Sea tectonics and Gondwana break-up*, Special Publication 108, Geological Society London, pp. 45 – 61.

Brozena, J., J. L LaBrecque, M. Peters, R. Bell and C. Raymond (1990). *Airborne gravity measurements over the sea-ice: the western Weddell Sea*, Geophysical Research Letters **17**: 1941 – 1944.

Burk, K. and J. F. Dewey (1974). *Two plates in Africa during the Cretaceous?*, Nature **249**: 313 – 316.

Cande, S. C. and D. V. Kent (1995). *A revised calibration of the geomagnetic polarity timescale for the Late Cretaceous and Cenozoic*, JGR **100** (B4): 6093 – 6095.

Cande, S. C., J. L. LaBrecque, R. L. Larson, W. C. Pittman, X. Golovchenko and W. F. Haxby (compiler) (1989). *Magnetic lineations of the world's ocean basins*, The American Association of Petroleum Geologists, Tulsa, Okla., USA.

Cochran, J. R. (1988). *Somali basin, chain ridge and origin of the northern Somali basin gravity and geoid low*, Journal of Geophysical Research **93**: 11985 – 12008.

Corner, B. and P. B. Groenewald (1991). *Gondwana reunited*, S. Afr. Trans. Nav. Antarkt. **21** (2): 172 – 183.

Corner, B., J. C. D. Maccelari and S. Niccol (1991). *Major magnetic anomalies in western Dronning Maud Land: their possible origin and correlates in southern Africa*, International Symposium on Earth Sciences **6**: 113.

Courtillot, V., C. Jaupart, I. Manighetti, P. Tapponnier and J. Besse (1999). *On causal links between flood basalts and continental breakup*, Earth and Planetary Science Letters **166**: 177 – 195.

Cox, A. and R. B. Hart (1986). *Plate Tectonics: How it works*, Blackwell Scientific Publications, Oxford, Great Britain.

Cox, K. G. (1992). *Karoo igneous activity, and the early stages of the break-up of Gondwanaland*, in: Storey, B. C., T. Alabaster and R. J. Pankhurst (eds), *Magmatism and the Causes of Continental Break-up*, Special Publication 68, Geological Society London, pp. 137 – 148.

Dalziel, I. W. D. and D. H. Elliot (1982). *West antarctica: Problem child of Gondwanaland*, Tectonics **1** (1): 3 – 19.

Dick, H. J. B., J. Lin and H. Schouten (2003). *An ultraslow-spreading class of ocean ridge*, Nature **426**: 405 – 412.

Duncan, R. A, P. R. Hooper, J. S. Rehacek, J. S. Marsh and A. R. Duncan (1997). *The timing and duration of the Karoo igneous event, southern Gondwana*, Journal of Geophysical Research **102** (B8): 18127 – 18138.

Elliot, D. H. and T. H. Fleming (2000). *Weddell triple junction: The principal focus of Ferrar and Karoo magmatism during initial breakup of Gondwana*, Geology **28** (6): 539 – 542.

Encarnacion, J., T. H. Fleming, D. H. Elliot and H. V. Eales (1996). *Synchronous emplacement of Ferrar and Karoo dolerites and the early breakup of Gondwana*, Geology **24** (6): 535 – 538.

Fairhead, J. D. (1988). *Mesozoic plate tectonic reconstructions of the central South Atlantic Ocean: The role of the West and Central African rift system*, in: Scotese, C. R. and W. W. Sager (eds), *Mesozoic and Cenozoic Plate Reconstructions*, Vol. 155, Tectonophysics, pp. 181 – 191.

Ferris, J. K., A. P. M. Vaughan and B. C. Storey (2000). *Relics of a complex triple junction in the Weddell Sea embayment, Antarctica*, Earth and Planetary Science Letters **178**: 215 – 230.

Ghidella, M. E. and J. L. LaBrecque (1997). *The Jurassic conjugate margins of the Weddell Sea: Considerations based on magnetic, gravity and paleobathymetry data*, in: Ricci, C. A. (ed.), *The Antarctic Region: Geological Evolution and Processes*, Terra Antarctica Publication, Siena, Italy, pp. 441 – 451.

Ghidella, M. E., C. A. Raymond and J. L. LaBrecque (1991). *Verification of crustal sources for satellite elevation magnetic anomalies in West Antarctica and the Weddell Sea and their regional tectonic implications*, in: Thomson, M. R. A., J. A. Crame and J. W. Thomson (eds), *Geological evolution of Antarctica*, Cambridge University Press, Cambridge, Great Britain, pp. 243 – 250.

Ghidella, M. E., G. Yáñez and J. L. LaBrecque (2002). *Revised tectonic implications for the magnetic anomalies of the western Weddell Sea*, Tectonophysics **347**: 65 – 86.

Gladczenko, T. P., K. Hinz, O. Eldholm, H. Meyer, S. Neben and J. Skogseid (1997). *South Atlantic volcanic margins*, Journal of Geological Society, London **154**: 465 – 470.

Golynsky, A. V. and N. D. Aleshkova (2000). *New aspects of crustal structure in the Weddell Sea region from aeromagnetic studies*, Polarforschung **67** (3): 133 – 141.

Golynsky, A. V., M. Chiappini, D. Damaske, F. Ferraccioli, J. Ferris, C. Finn, M. Ghidella, T. Isihara, A. Johnson, H. R. Kim, L. Kovacs, J. L. LaBrecque, V. N. Masolov, Y. Nogi, M. Purucker, P. Taylor and M. Torta (2001). *ADMAP - Magnetic anomaly map of the Antarctic, 1:10000000 scale map*, in: Morris, P. and R. von Frese (eds), *BAS (Misc.) 10*, British Antarctic Survey.

Golynsky, A. V., P. Morris, L. C. Kovacs and J. Ferris (2002a). *A new magnetic anomaly map of the Weddell Sea and Antarctic Peninsula*, Tectonophysics **347**: 3–11.

Golynsky, A. V., S.V. Alyavadi, V.N. Masolov, A.S. Tscherinov and V.S. Volnukhin (2002b). *The composite magnetic anomaly map of the East Antarctic*, Tectonophysics **347**: 109–120.

Goodlad, S. W., A. K. Martin and C. J. H. Hartnady (1982). *Mesozoic magnetic anomalies in the southern Natal Valley*, Nature **295**: 686 – 688.

Gradstein, F. M., F. P. Agterberg, J. G. Ogg, J. Hardenbohl, P. van Veen, J. Thierry and Z. Huang (1994). *A Mezozoic time scale*, Journal of Geophysical Research **99**: 24051–24074.

Greiner, B. (1999). *Euler rotations in plate-tectonic reconstructions*, Computers & Geosciences **25**: 209–216.

Grikurov, G. E., V. L. Ivanov, G. L. Leitchenkov, N. D. Aleshkova, A. V. Golynsky and R. G. Kurinin (1991). *Structure and evolution of the sedimentary basin in the Weddell Sea province, in: Abstracts - Sixth International Symposium on Antarctic Earth Science*, Tokyo, Japan, pp. 185 – 190.

Groenewald, P.B., G.G. Grantham and M.K. Watkeys (1991). *Geological evidence for a Proterozoic to Mesozoic link between southeastern Africa and Dronning Maud Land, Antarctica*, Journal of Geological Society, London **148**: 1115 – 1123.

Grunow, A. M. (1993). *Creation and destruction of Weddell Sea floor in the Jurassic*, Geology **21**: 647 – 650.

Hansen, R. Q. and Y. Miyazaki (1984). *Continuation of potential fields between arbitrary surfaces*, Geophysics **49** (6): 787–795.

Haugland, K., Y. Kristoffersen and A. Velde (1985). *Seismic investigations in the Weddell Sea embayment*, Tectonophysics **114**: 293 – 313.

Haxby, W. F. (1988). *Organization of oblique sea floor spreading into discrete, uniformly spaced ridge segments: evidence from GEOSAT altimeter data in the Weddell Sea (abstract)*, EOS Transactions, American Geophysical Union **69**: 1155.

Hinz, K. (1981). *A hypothesis of terrestrial catastrophes - wedges of very thick oceanward dipping layers beneath passive continental margins - their origin and paleoenvironmental significance*, Geologisches Jahrbuch **E 22**: 3 – 28.

Hinz, K. and W. Krause (1982). *The continental margin of Queen Maud Land, Antarctica: Seismic sequences, structural elements and geological development*, Geologisches Jahrbuch **E 23**: 17 – 41.

Hinz, K. and Y. Kristoffersen (1987). *Antarctica, recent advances in the understanding of the continental shelf*, Geologisches Jahrbuch **E 37**: 3 – 54.

Hinz, K., S. Neben, B. Schreckenberger, H. A. Roeser, M Block, K. Goncalves de Souza and H. Meyer (1999). *The Argentine continental margin north of 48°S: sedimentary successions, volcanic activity during breakup*, Marine and Petroleum Geology **16**: 1 – 25.

Hübscher, C., W. Jokat and H. Miller (1996). *Structure and origin of southern Weddell Sea crust: results and implications*, in: Storey, B. C., E. C. King and R. A. Livermore (eds), *Weddell Sea Tectonics and Gondwana Break-up*, Special Publication 108, Geological Society London, pp. 201 – 211.

Hunter, R. J., A. C. Johnson and N. D. Aleshkova (1996). *Aeromagnetic data from the southern Weddell Sea embayment and adjacent areas: synthesis and interpretation*, in: Storey, B. C., E. C. King and R. A. Livermore (eds), *Weddell Sea Tectonics and Gondwana Break-up*, Special Publication 108, Geological Society London, pp. 143 – 154.

IAGA, Division V, Working Group 8 (1996). *International geomagnetic reference field, 1995 revision*, Geophysical Journal International **125**: 318 – 321.

Isezaki, N. (1986). *A new shipboard three-component magnetometer*, Geophysics **51** (10): 1992 – 1998.

Isezaki, N., J. Matsuda, H. Inokuchi and K. Yaskawa (1981). *Shipboard measurements of three components of geomagnetic field*, Journal of Geomagnetism and Geoelectricity **33**: 329 – 333.

Jacobs, J. and R.J. Thomas (2004). *Himalayan-type indenter-escape tectonics model for the southern part of the late Neoproterozoic-early paleozoic East African-Antarctic orogen*, Geology **32** (8): 721 – 724.

Jacobs, J., C.M. Fanning and W. Bauer (2003). *Timing of Grenville-age vs. Pan-African medium- to high grade metamorphism in western Dronning Maud Land (East Antarctica) and significance for correlations in rodinia and gondwana*, Precambrian Research **125**: 1 – 20.

Johnson, A. C., N. D. Aleshkova, P. F. Barker, A. V. Golynsky, V. N. Masolov and A. M. Smith (1992). *A preliminary aeromagnetic anomaly compilation map for the Weddell province of Antarctica*, in: Yoshida, Y., K. Kaminuma and K. Shiraishi (eds), *Recent Progress in Antarctic Earth Science*, Terra Scientific Publishing Company, Tokyo, Japan, pp. 545 – 553.

Jokat, W., C. Hübscher, U. Meyer, L. Oszko, T. Schöne, W. Versteeg and H. Miller (1996). *The continental margin off East Antarctica between 10° W and 30° W*, in: Storey, B. C., E. C. King and R. A. Livermore (eds), *Weddell Sea Tectonics and Gondwana Break-up*, Special Publication 108, Geological Society London, pp. 129 – 141.

Jokat, W., O. Ritzmann, M. C. Schmidt-Aursch, S. Drachev, S. Gauger and J. Snow (2003a). *Geophysical evidence for reduced melt production on the Arctic ultraslow Gakkel mid-ocean ridge*, Nature **423**: 962 – 965.

Jokat, W., T. Boebel, M. König and U. Meyer (2003b). *Timing and geometry of the early Gondwana breakup*, Journal of Geophysical Research **108** (B9): 2428, doi:10.1029/2002JB001802.

Kaul, N. (1991). *Detaillierte seismische Untersuchungen am östlichen Kontinentalrand des Weddell-Meeres vor Kapp Norvegia, Antarktis*, Vol. 89 of *Berichte zur Polarforschung (Reports on Polar Research)*, Alfred-Wegener-Institut für Polar- und Meeresforschung, Bremerhaven, Germany.

Kent, D. V. and F. M. Gradstein (1986). *A Jurassic to recent chronology*, in: Tucholke, B. E. and P. R. Vogt (eds), *The Geology of North America: The Western Atlantic Region*, Vol. 1 of *DNAG Series*, Geological Society of America, pp. 45 – 50.

Kopsch, C. and R. Kroth (2003). *Geomagnetic measurements*, in: Jokat, W. and G. Krause (eds), *The Expedition Antarktis XIX of RV Polarstern in 2001/2002, reports of legs 1 and 2*, Vol. 448 of *Berichte zur Polarforschung (Reports on Polar Research)*, Alfred-Wegener-Institut für Polar- und Meeresforschung, Bremerhaven, Germany, pp. 53–56.

Kopsch, C., T. Ebel and R. Kroth (2000). *Geomagnetische Messungen auf PS von Punta Arenas nach Bremerhaven*, unpublished.

Korenaga, J. (1995). *Comprehensive analysis of marine magnetic vector anomalies*, Journal of Geophysical Research **100** (B1): 365 – 378.

Kovacs, L. C., P. Morris, J. Brozena and A. Tikku (2002). *Seafloor spreading in the Weddell Seas from magnetic and gravity data*, Tectonophysics **347**: 43 – 64.

Kristoffersen, Y. and K. Haugland (1986). *Geophysical evidence for the East Antarctic plate boundary in the Weddell Sea*, Nature **322**: 538 – 541.

Kristoffersen, Y. and K. Hinz (1991). *Evolution of the Gondwana plate boundary in the Weddell Sea area*, in: Thomson, M. R. A. and J. A. Crame (eds), *Geological evolution of Antarctica*, Cambridge University Press, Cambridge, Great Britain, pp. 225 – 230.

LaBrecque, J. L. (1987). *The USAC program: magnetic anomalies of the western Weddell Basin*, EOS Transactions, American Geophysical Union **68**: 1459.

LaBrecque, J. L. and D. E. Hayes (1979). *Seafloor spreading history of the Agulhas Basin*, Earth and Planetary Science Letters **45**: 411 – 428.

LaBrecque, J. L. and M. E. Ghidella (1997). *Bathymetry, depth to magnetic basement, and sediment thickness estimates from aerogeophysical data over the western Weddell Sea*, Journal of Geophysical Research **102** (B4): 7929 – 7945.

LaBrecque, J. L. and P. Barker (1981). *The age of the Weddell Basin*, Nature **290**: 489 – 492.

LaBrecque, J. L., J. Brozena, J. C. Parra, M. A. Keller, W. Haxby, C. A. Raymond, L. Kovacs, R. Bell, G. Yáñez, M. Peters, S. Cande and J. Valldares (1989). *USAC aerosurvey results for the Weddell Basin: Part I, 28th International Geological Congress*, Washington, DC, USA.

LaBrecque, J. L., S. Cande, R. Bell, C. Raymond, J. Brozena, M. Keller, J. C. Parra and G. Yáñez (1986). *Aerogeophysical survey yields new data in the Weddell Sea*, Antarctic Journal of the United States **5**: 69 – 71.

Lawver, L. A., J. G. Sclater and L. Meinke (1985). *Mesozoic and Cenozoic reconstructions of the South Atlantic*, Tectonophysics **114**: 233 – 254.

Lawver, L. A., L. M. Gahagan and I. W. D. Dalziel (1998). *A tight fit - early Mesozoic Gondwana, a plate reconstruction perspective*, *Origin and Evolution of Continents*, Vol. 53 of *Memorials of National Institute of Polar Research, Special Issue*, National Institute of Polar Research, pp. 203 – 213.

Lawver, L. A., L. M. Gahagan and M. F. Coffin (1992). *The development of paleo-seaways around Antarctica*, Antarctic Research Series **56**: 7 – 30.

Leitchenkov, G. L. and G. A. Kudryavtzev (2000). *Structure and origin of the earth's crust in the Weddell Sea embayment (beneath the front of the Filchner and Ronne Ice Shelves) from deep seismic sounding*, Polarforschung **67** (3): 143 – 154.

Lengning, K. (1961). *Messungen mit dem Bidlingmaierschen Doppelkompaß während der Nordmeerreise des MS METEOR, Abhandlung Nr. 27 des Geomagnetischen Instituts Potsdam*, Geomagnetisches Observatorium Potsdam, Germany.

Livermore, R. A. and J. Hunter (1996). *Mesozoic seafloor spreading in the southern Weddell Sea*, in: Storey, B. C., E. C. King and R. A. Livermore (eds), *Weddell Sea Tectonics and Gondwana Break-up*, Special Publication 108, Geological Society London, pp. 227 – 241.

Livermore, R. A. and R. W. Woollett (1993). *Seafloor spreading in the Weddell Sea and southwest Atlantic since the Late Cretaceous*, Earth and Planetary Science Letters **117**: 475 – 495.

Livermore, R., A. Nankivell, G. Eagles and P. Morris (2005). *Paleogene opening of Drake Passage*, Earth and Planetary Science Letters. in press.

Lorenzo, J. M. and J. C. Mutter (1988). *Seismic stratigraphy and tectonic evolution of the Falkland/Malvinas Plateau*, Revista Brasileira de Geociências **18** (2): 191 – 200.

Ludwig, W. J. (1983). *Geological framework of the Falkland Plateau*, in: Blakeslee, J. H. and M. Lee (eds), *Initial Reports of the Deep Sea Drilling Project*, Vol. 71, Part 2, Scripps Institution of Oceanography, University of California, USA, pp. 281 – 293.

Macdonald, D., I. Gomez-Perez, J. Franzese, L. Spalletti, L. A. Lawver, L. M. Gahagan, I. W. D. Dalziel, I. Thomas, T. Nigel, M. Hole and D. Paton (2003). *Mesozoic break-up of SW Gondwana: implications for regional hydrocarbon potential of the southern South Atlantic*, Marine and Petroleum Geology **20**: 287 – 308.

Marks, K. M. and A. A. Tikku (2001). *Cretaceous reconstructions of East Antarctica, Africa and Madagascar*, Earth and Planetary Science Letters **186**: 479 – 495.

Marshall, J. E. A. (1994). *The Falkland Islands: A key element in Gondwana paleogeography*, Tectonics **13** (2): 499 – 514.

Martin, A. K. and C. J. H. Hartnady (1986). *Plate tectonic development of the South West Indian Ocean: A revised reconstruction of East Antarctica and Africa*, Journal of Geophysical Research **91** (B5): 4767 – 4786.

Martin, A. K., S. W. Goodlad, C. J. H. Hartnady and A. du Plessis (1982). *Cretaceous palaeopositions of the Falkland Plateau relative to southern Africa using Mesozoic seafloor spreading anomalies*, Geophysical Journal of the Royal Astronomical Society **71**: 567 – 579.

Masolov, V. N. (1980). *Structure of the magnetic basement in the south-eastern part of the Weddell Sea basin, in: Geofizicheskie Issledovania v Antarctide*, Research Institute of Arctic Geology, Leningrad, Russia, pp. 14 – 28. (in Russian).

Max, M. D., M. Ghidella, L. Kovacs, M. Paterlini and J. A. Valladares (1999). *Geology of the Argentine continental shelf and margin from aeromagnetic survey*, Marine and Petroleum Geology **16**: 41 – 64.

McAdoo, D. C. and K. M. Marks (1992a). *Gravity fields of the Southern Ocean from GEOSAT data*, Journal of Geophysical Research **97** (B3): 3247 – 3260.

McAdoo, D. C. and K. M. Marks (1992b). *Resolving marine gravity with ERS-1 satellite altimetry*, Geophysical Research Letters **19** (22): 2271 – 2274.

McAdoo, D. C. and S. W. Laxon (1996). *Marine gravity from GEOSAT and ERS-1 altimetry in the Weddell Sea*, in: Storey, B. C., E. C. King and R. A. Livermore (eds), *Weddell Sea Tectonics and Gondwana Break-up*, Special Publication 108, Geological Society London, pp. 155 – 164.

McAdoo, D. C. and S. W. Laxon (1997). *Antarctic tectonics: constraints from an ERS-1 satellite marine gravity field*, Science **276**: 556 – 560.

Miller, H., E. Lippmann and W. Kallerhoff (1984). *Marine geophysical work during Antarctic II/4*, in: Kohnen, H. (ed.), *Die Expedition ANTARKTIS II mit FS 'Polarstern' 1983/84, Bericht vom Fahrtabschnitt 4 (ANT-II/4)*, Vol. 19 of *Berichte zur Polarforschung (Reports on Polar Research)*, Alfred-Wegener-Institut für Polar- und Meeresforschung, Bremerhaven, Germany, pp. 116 – 128.

Miller, H., M. De Batist, W. Jokat, N. Kaul, S. Steinmetz, G. Uenzelmann-Neben and W. Versteeg (1990). *Revised interpretation of tectonic features in the southern Weddell Sea, Antarctica, from new seismic data*, Polarforschung **60**: 33 – 38.

Mougenot, D., M. Gennesseaux, J. Hernandez, C. Lepvrier, J.-A. Malod, S. Raillard, J. R. Vanney and M. Villeneuve (1991). *La ride du Mozambique (Océan Indien): un fragment continental individualisé lors du coulissement de l'Amérique et de l'Antarctique de long de l'Afrique de l'Est ?*, C. R. Acad. Sci. **312** (II): 655 – 662.

Müller, R. D., W. Roest, J. Y. Royer, L. M. Gahagan and J. L. Sclater (1997). *Digital isochrons of the world's ocean floor*, Journal of Geophysical Research **102** (B2): 3211 – 3214.

Mutter, J. C. (1985). *Seaward dipping reflectors and the continent-ocean boundary at passive continental margins*, Tectonophysics **114**: 117 – 131.

Mutterlose, J. and S. W. Jr. Wise (1990). *Lower Cretaceous nannofossil biostratigraphy of ODP leg 113 holes 692b and 693a, continental slope off East Antarctica, Weddell Sea*, in: Barker, P. F. and J. P. Kennett (eds), *Proceedings of the Ocean Drilling Program, Scientific Results*, Vol. 113, College Station, TX (Ocean Drilling Program), pp. 325 – 352.

Nankivell, A. (1997). *Tectonic evolution of the Southern Ocean between Antarctica, South America and Africa over the past 84 Ma*, PhD thesis, University of Oxford, Oxford, Great Britain.

Nogi, Y. and K. Kaminuma (1999a). *Measurements of vector anomalies on board the icebreaker Shirase and the magnetization of the ship*, Annali di Geofisica **42** (2): 161 – 170.

Nogi, Y. and K. Kaminuma (1999b). *Vector magnetic anomalies in the West Enderby Basin*, Korean Journal of Polar Research **10** (2): 117 – 124.

Nogi, Y. and N. Seama (2002). *Basement orientation on the East Enderby Basin, southern Indian Ocean*, in: Gamble, J. A., D. N. B. Skinner and S. Henrys (eds), *Antarctica at the close of a millennium, Proceedings of the 8th International Symposium on Antarctic Earth Sciences*, Royal Society of New Zealand, pp. 539 – 547.

Nogi, Y., N. Seama and N. Isezaki (1990a). *Preliminary report of the three components of geomagnetic field measured on board the icebreaker Shirase during JARE-30, 1988-1989*, *Proceedings of Symposium on Antarctic Geosciences*, National Institute of Polar Research, Tokyo, Japan, pp. 191 – 200.

Nogi, Y., N. Seama, N. Isezaki and Y. Fukuda (1996). *Magnetic anomaly lineations and fracture zones deduced from vector magnetic anomalies in the West Enderby Basin*, in: Storey, B. C., E. C. King and R. A. . Livermore (eds), *Weddell Sea tectonics and Gondwana break-up*, Special Publication 108, Geological Society London, pp. 265 – 273.

Nogi, Y., N. Seama, N. Isezaki, M. Funaki and K. Kaminuma (1990b). *Measurements of geomagnetic field at sea during JARE-30, 1988-1989*, The Antarctic Record **34** (3): 346 – 356.

Norton, I. O. and J. G. Sclater (1979). *A model for the evolution of the Indian Ocean and the breakup of Gondwanaland*, Journal of Geophysical Research **84** (B12): 6803 – 6830.

Nürnberg, D. and R. D. Müller (1991). *The tectonic evolution of the South Atlantic from Late Jurassic to present*, Tectonophysics **191**: 27 – 33.

Peters, K. (2000). *Erkennung von Unregelmäßigkeiten des Erdmagnetfeldes von einem unkompensierten Schiff aus*, PhD thesis, TU Hamburg-Harburg, Hamburg, Germany.

Peters, M., B. Haverkamp, R. Emmermann, H. Kohnen and K. Weber (1991). *Palaeomagnetism, K-Ar dating and geodynamic setting of igneous rocks in western and central Neuschwabenland, Antarctica*, in: Thomson, M. R. A., J.A. Crame and J. W. Thomson (eds), *Geological evolution of Antarctica*, Cambridge University Press, Cambridge, Great Britain, pp. 549 – 555.

Platt, N. H. and P. R. Philip (1995). *Structure of the southern Falkland Islands continental shelf: initial results from new seismic data*, Marine and Petroleum Geology **12** (7): 759 – 771.

Rabinowitz, P. D. and J. L. LaBrecque (1979). *The Mesozoic South Atlantic Ocean and evolution of its continental margins*, Journal of Geophysical Research **84** (B11): 5973 – 6002.

Rabinowitz, P. D., M. F. Coffin and D. Falvey (1983). *The separation of Madagascar and Africa*, Science **220**: 67 – 69.

Rapela, C. W. and R. J. Pankhurst (1992). *The granites of northern Patagonia and the Gastre Faults System in relation to the break-up of Gondwana*, in: Storey, B. C., T. Alabaster and R. J. Pankhurst (eds), *Magmatism and the Causes of Continental Break-up*, Special Publication 68, Geological Society London, pp. 209 – 220.

Reeves, C. and M. de Wit (2000). *Making ends meet in Gondwana: retracing the transforms of the Indian Ocean and reconnecting continental shear zones*, Terra Nova **12**: 272 – 280.

Roeser, H. A., J. Fritsch and K. Hinz (1996). *The development of the crust off Dronning Maud Land, East Antarctica*, in: Storey, B. C., E. C. King and R. A. Livermore (eds), *Weddell Sea Tectonics and Gondwana Break-up*, Special Publication 108, Geological Society London, pp. 243 – 264.

Rogenhagen, J. and W. Jokat (2000). *The sedimentary structure in the Western Weddell Sea*, Marine Geology **168**: 45 – 60.

Rogenhagen, J. and W. Jokat (2002). *Origin of the gravity ridges and Anomaly-T in the southern Weddell Sea*, in: Gamble, J. A., D. N. B. Skinner and S. Henrys (eds), *Antarctica at the close of a millennium, Proceedings of the 8th International Symposium on Antarctic Earth Sciences*, Royal Society of New Zealand, pp. 227 – 231.

Royer, J. Y., P. Patriat, H. W. Bergh and C. Scotese (1988). *Evolution of the Southwest Indian Ridge from the Late Cretaceous (anomaly 34) to the middle Eocene (anomaly 20)*, Tectonophysics **155**: 235 – 260.

Rustenbach, J., H. U. Auster, A. Lichopoj, H. Bitterlich, K. H. Fornacon, O. Hillenmaier, R. Krause and H. J. Schenk (1998). *Magnetic field measurements in orbit and on planetary surfaces using a digital fluxgate magnetometer*, in: Pfaff, R. F., Borovsky, J. E., Young, D. T. (ed.), *Measurement techniques in space plasmas fields*, Vol. 103 of *Geophysical Monograph*, American Geophysical Union, Washington, DC, pp. 115 – 120.

Sandwell, D. T. and W. H. F. Smith (1997). *Marine gravity anomaly from GEOSAT, ERS-1 satellite altimetry*, Journal of Geophysical Research **102** (B5): 10039 – 10054.

Schreckenberger, B. and S. Neben (2003). *Research Cruise BGR03, BOSA, Breakup of the South Atlantic, Cruise report and preliminary results*, Federal Institute of Geosciences and Natural Resources, Hannover, Germany.

Scotese, C.R. and W.W Sager (eds) (1989). *mesozoic and cenozoic plate reconstructions*, Elsevier.

Seama, N. and N. Isezaki (1990). *Sea-floor magnetization in the eastern part of the Japan Basin and its tectonic implications*, Tectonophysics **181**: 285 – 297.

Seama, N., Y. Nogi and N. Isezaki (1993). *A new method for precise determination of the position and strike of magnetic boundaries using vector data of the geomagnetic anomaly field*, Geophysical Journal International **113**: 155 – 164.

Segoufin, J. and P. Patriat (1980). *Existence d'anomalies mésozoiques dans le basin de Somalie. implication pour les relations Afrique-Antarctique-Madagascar*, C. R. Acad. Sci. **291**: 85 – 88.

Shaw, P. R. and S. C. Cande (1990). *High-resolution inversion for South Atlantic plate kinematics using joint altimeter and magnetic anomaly data*, Journal of Geophysical Research **95** (B3): 2625 – 2644.

Sibuet, J. C., W. W. Hay, A. Prunier, L. Montadert, K. Hinz and J. Fritsch (1984). *Early evolution of the South Atlantic Ocean: role of the rifting episode*, Initial Reports of DSDP **75**: 496 – 481.

Smith, W. H. F. and P. Wessel (1990). *Gridding with continuous curvature splines in tension*, Geophysics **55**: 293–305.

Storey, B. C., E. C. King and R. A. Livermore (eds) (1996). *Weddell Sea Tectonics and Gondwana Break-up*, Special Publication 108, Geological Society London.

Storey, B. C., M. L. Curtis, J. K. Ferris, M. A. Hunter and R. A. Livermore (1999). *Reconstructions and break-out model for the Falkland Islands within Gondwana*, Journal of African Earth Sciences **29** (1): 153 – 163.

Storey, B. C., P. T. Leat and J. K. Ferris (2001). *The location of mantle-plume centers during the initial stages of Gondwana breakup*, in: Ernst, R. E. and K. L. Buchan (eds), *Mantle Plumes: Their Identification through Time*, Special Paper 352, Geological Society of America, Boulder, Colorado, USA, pp. 71 – 80.

Studinger, M. (1998). *Compilation and analysis of potential field data from the Weddell Sea, Antarctica: implications for the break-up of Gondwana*, Vol. 276 of *Berichte zur Polarforschung (Reports on Polar Research)*, Alfred-Wegener-Institut für Polar- und Meeresforschung, Bremerhaven, Germany.

Taylor, G. K. and J. Shaw (1989). *The Falkalnd Islands: New palaeomagnetic data and their origin as a displaced terrane from Southern Africa*, in: Hillhouse, J. W. (ed.), *Deep Structure and Past Kinematics of Accreted Terranes*, Vol. 50 of *Geophysical Monograph*, American Geophysical Union, Washington, DC, USA, pp. 59 – 72.

Tikku, A. A., K. Marks and L. C. Kovacs (2002). *An Early Cretaceous extinct spreading center in the northern Natal Valley*, Tectonophysics **347**: 87 – 108.

Unternehr, P., D. Curie, J. L. Olivet, J. Goslin and P. Beuzart (1988). *South Atlantic fits and intraplate boundaries in Africa and South America*, in: Scotese, C. R. and W. W. Sager (eds), *Mesozoic and Cenozoic Plate Reconstructions*, Vol. 155, Tectonophysics, pp. 169 – 179.

Verhoef, J., W. R. Roest, R. Macnab, J. Arkani-Hamed and Members of Project Team (1996). *Magnetic anomalies of the Arctic and North Atlantic Oceans and adjacent land areas*, Technical report, Geological Survey Canada, Dartmouth, NS, Canada. GSC Open File, Part a and b (CD-ROM and project report).

Wessel, P. and W. H. F. Smith (1998). *New improved version of generic mapping tools released*, EOS Transactions, American Geophysical Union **79**: 579.

White, R. and D. McKenzie (1989). *Magmatism at rift zones: The generation of volcanic continental margins and flood basalts*, Journal of Geophysical Research **94** (B6): 7685 – 7729.

Acknowledgements

I sincerely thank Prof. Dr. Heinrich Miller who offered me the possibility to carry out this work at the Alfred-Wegener-Institute. His special interest in shipborne magnetics made me aware of the importance of, and possibilities arising from, a magnetometer system fixed to a ship.

In addition, Prof. Dr. Tilo von Dobeneck deserves many thanks for his readiness to act as the second referee and for his interest, especially, in the shipborne magnetics, carried out in this thesis.

Dr. Wilfried Jokat awakened my interest in the field of ships' magnetism during my first *Polarstern* cruise in 1998, long before I actually started my doctoral thesis. His never-ending willingness to solve all the greater and smaller problems in the Weddell Sea using *the geophysical approach* helped me to familiarize myself with all the plates and boundaries acting, occasionally at the same time, in the Weddell Sea. Thanks for encouraging!

Dr. Graeme Eagles did a lot of work filling all the gaps in this thesis with *commas* and turning sentences from backwards to forwards, but also helped me whenever I got lost in rotations.

Dr. Andreas Läufer reviewed the manuscript of this thesis from a geological point of view, and Dr. Joachim Jacobs gave me several introductions into the *really old* geological history of Dronning Maud Land, and taught me about what a geologist can see in a magnetic anomaly map.

Many thanks go to Conny Kopsch, Ronald Kroth and Volker & Uli Auster who set up the magnetometer system onboard RV *Polarstern* and gave me a speedy introduction into shipborne magnetics. Additionally, the crew of RV *Polarstern* deserves special thanks for performing all those calibration loops in the last couple of years.

I thank the marine geophysics working group for discussions, not only about geophysics and Sven Riedel for all the discussions about potential fields and potential errors.

To my parents, who always supported the things I did and probably will never give up to believe in the things I do: Thanks for all the years.

After all, I will thank Astrid for her tremendous patience and endurance during the last days, ... weeks, ... and years.

List of Figures

Appendix

A Coefficients for the induced and permanent ship's field

ID	Date	a_{11}	a_{12}	a_{13}	K_1
1a	28.08.2002	-0.0583	0.0718	0.1565	-4950.4
1b	28.08.2002	-0.0592	0.0718	0.1392	-4080.9
2	08.09.2002	-0.0605	0.0870	-0.1274	9887.5
3a	21.09.2002	-0.0633	0.0810	-0.0069	3344.0
3b	21.09.2002	-0.0669	0.0779	0.0536	92.0
4a	30.09.2002	-0.0579	0.0753	0.2953	-12778.0
4b	30.09.2002	-0.0467	0.0800	0.3880	-17685.0
5	09.10.2002	-0.0706	0.1120	0.3298	-14639.1
mean value		-0.0604	0.0821	0.1535	-5101.2
standard dev.		0.0067	0.0122	0.1662	8890.1

ID	Date	a_{21}	a_{22}	a_{23}	K_2
1a	28.08.2002	0.0512	-0.1154	-0.0387	8604.5
1b	28.08.2002	0.0520	-0.1129	-0.1200	12753.1
2	08.09.2002	0.0390	-0.1147	0.1033	1113.8
3a	21.09.2002	0.0439	-0.1181	-0.0283	8222.9
3b	21.09.2002	0.0474	-0.1204	0.3116	-9991.3
4a	30.09.2002	0.0519	-0.1170	-0.2334	19155.8
4b	30.09.2002	0.0466	-0.1110	0.3230	-10537.1
5	09.10.2002	0.0114	-0.1150	0.2893	-8734.2
mean value		0.0429	-0.1156	0.0759	2573.4
standard dev.		0.0126	0.0028	0.2003	10645.7

ID	Date	a_{31}	a_{32}	a_{33}	K_3
1a	28.08.2002	0.0052	0.0410	0.0175	16481.5
1b	28.08.2002	0.0043	0.0388	0.0758	13514.2
2	08.09.2002	0.0007	0.0391	0.0411	15737.2
3a	21.09.2002	0.0032	0.0380	0.0633	14488.1
3b	21.09.2002	0.0018	0.0364	0.0295	16305.5
4a	30.09.2002	0.0065	0.0389	0.0148	17238.1
4b	30.09.2002	0.0013	0.0406	0.1792	8388.8
5	09.10.2002	-0.0114	0.0390	0.2604	3933.9
mean value		0.0015	0.0390	0.0852	13260.9
standard dev.		0.0052	0.0013	0.0827	4385.9

Table A-1 : Coefficients for the induced and permanent ship's field for all calibration loops for the port sensor.

ID	Date	a_{11}	a_{12}	a_{13}	K_1
1a	28.08.2002	-0.0652	-0.1187	0.1430	-2620.7
1b	28.08.2002	-0.0663	-0.1171	0.0909	24.7
2	08.09.2002	-0.0673	-0.1046	0.0176	3714.9
3a	21.09.2002	-0.0677	-0.1055	-0.1497	12679.6
3b	21.09.2002	-0.0697	-0.1112	-0.1712	13831.5
4a	30.09.2002	-0.0647	-0.1131	0.3289	-12916.4
4b	30.09.2002	-0.0524	-0.1096	0.3199	-12395.4
5	09.10.2002	-0.0659	-0.0769	0.2022	-6177.6
mean value		-0.0649	-0.1071	0.0977	-482.4
standard dev.		0.0049	0.0123	0.1788	9549.4

ID	Date	a_{21}	a_{22}	a_{23}	K_2
1a	28.08.2002	-0.0066	-0.1172	-0.0308	-6787.2
1b	28.08.2002	-0.0073	-0.1172	-0.0818	-4179.3
2	08.09.2002	-0.0172	-0.1162	0.1103	-14380.3
3a	21.09.2002	-0.0092	-0.1217	0.1469	-16288.7
3b	21.09.2002	-0.0089	-0.1248	0.3315	-26177.3
4a	30.09.2002	-0.0031	-0.1189	-0.2469	4750.5
4b	30.09.2002	-0.0090	-0.1141	0.2909	-23950.1
5	09.10.2002	-0.0430	-0.1216	0.3021	-24533.7
mean value		-0.0130	-0.1190	0.1028	-13943.3
standard dev.		0.0119	0.0033	0.1948	10390.3

ID	Date	a_{31}	a_{32}	a_{33}	K_3
1a	28.08.2002	-0.0023	-0.0334	0.0183	9210.5
1b	28.08.2002	-0.0035	-0.0346	0.0419	8023.9
2	08.09.2002	-0.0054	-0.0342	0.0785	6510.4
3a	21.09.2002	-0.0022	-0.0341	0.0698	6948.3
3b	21.09.2002	-0.0003	-0.0360	0.0584	7562.9
4a	30.09.2002	0.0005	-0.0327	-0.0072	11211.8
4b	30.09.2002	-0.0043	-0.0321	0.1386	3348.0
5	09.10.2002	-0.0097	-0.0348	0.2164	-913.4
mean value		-0.0034	-0.0340	0.0768	6487.8
standard dev.		0.0030	0.0012	0.0665	3501.7

Table A-2 : Coefficients for the induced and permanent ship's field for all calibration loops for the starboard sensor.

B Geomagnetic Polarity Time Scale

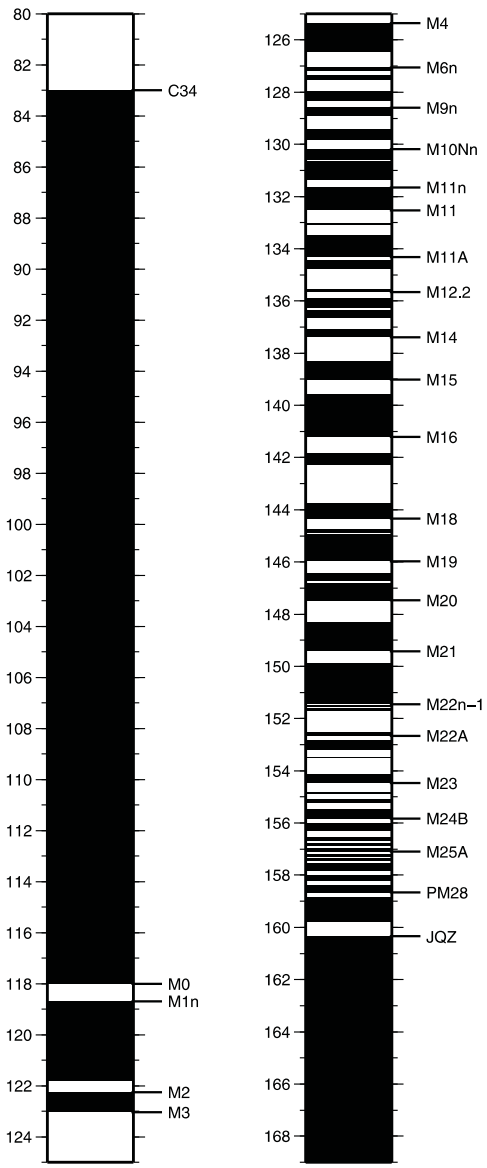

Geomagnetic Polarity Time Scale

after Kent & Gradstein (1985)

33	73.619	79.075	N	M19n-1	144.88	144.96	R
	79.075	83.000	R		144.96	145.98	N
34	83.000	118.00	N	M19	145.98	146.44	R
M0	118.00	118.70	R		146.44	146.75	N
M1n	118.70	121.81	N	M20n-1	146.75	146.81	R
M1	121.81	122.25	R		146.81	147.47	N
M2	122.25	123.03	N	M20	147.47	148.33	R
M3	123.03	125.36	R		148.33	149.42	N
M4	125.36	126.46	N	M21	149.42	149.89	R
M5	126.46	127.05	R		149.89	151.46	N
M6n	127.05	127.21	N	M22n-1	151.46	151.51	R
M6	127.21	127.34	R		151.51	151.56	N
M7n	127.34	127.52	N	M22n-2	151.56	151.61	R
M7	127.52	127.97	R		151.61	151.69	N
M8n	127.97	128.33	N	M22	151.69	152.53	R
M8	128.33	128.60	R		152.53	152.66	N
M9n	128.60	128.91	N	M22A	152.66	152.84	R
M9	128.91	129.43	R		152.84	153.21	N
M10n	129.43	129.82	N	M22A	153.21	153.49	R
M10	129.82	130.19	R		153.49	153.52	N
M10Nn	130.19	130.57	N	M23	153.52	154.15	R
M10Nn-1	130.57	130.63	R		154.15	154.48	N
M10Nn	130.63	131.00	N	M23	154.48	154.85	R
M10Nn-2	131.00	131.02	R		154.85	154.88	N
M10Nn	131.02	131.36	N	M24	154.88	155.08	R
M10N	131.36	131.65	R		155.08	155.21	N
M11n	131.65	132.53	N	M24A	155.21	155.48	R
M11	132.53	133.03	R		155.48	155.84	N
M11-1	133.03	133.08	N	M24B	155.84	156.00	R
M11	133.08	133.50	R		156.00	156.29	N
	133.50	134.31	N	M25	156.29	156.55	R
M11A	134.31	134.42	R		156.55	156.70	N
	134.42	134.75	N	M25An-1	156.70	156.78	R
M12.1	134.75	135.56	R		156.78	156.88	N
	135.56	135.66	N	M25An-2	156.88	156.96	R
M12.2	135.66	135.88	R		156.96	157.10	N
	135.88	136.24	N	M25A	157.10	157.20	R
M12A	136.24	136.37	R		157.20	157.30	N
	136.37	136.64	N	M26n-1	157.30	157.38	R
M13	136.64	137.10	R		157.38	157.46	N
	137.10	137.39	N	M26n-2	157.46	157.53	R
M14	137.39	138.30	R		157.53	157.61	N
	138.30	139.01	N	M26n-3	157.61	157.66	R
M15	139.01	139.58	R		157.66	157.85	N
	139.58	141.20	N	PM26	157.85	158.01	R
M16	141.20	141.85	R		158.01	158.21	N
	141.85	142.27	N	PM27	158.21	158.37	R
M17	142.27	143.76	R		158.37	158.66	N
	143.76	144.33	N	PM28	158.66	158.87	R
M18	144.33	144.75	R		158.87	159.80	N
	144.75	144.88	N	PM29	159.80	160.33	R
				JQZ	160.33	169.00	N

Ages in Ma

Figure B-1 : Geomagnetic Polarity Time Scale after Kent & Gradstein (1985).

C Finite rotations for the Gondwana break-up model

Angles are conventionally measured counterclockwise.

Table C-1 : **Falkland Plateau - Antarctica** (Weddell Sea opening)

Age [Ma]	Chron	Pole of rotation lat[°]	lon [°]	Angle [°]	Source
83.00	C34	-77.92	246.51	-30.08	after Shaw and Cande (1990) [SAM-AFR] and Royer et al. (1988) [AFR-ANT]
93.00	E	-75.90	241.00	-33.02	Livermore and Hunter (1996)
118.00	M0	-72.96	263.97	-45.17	this study
122.25	M2	-72.40	265.30	-46.80	this study
125.36	M4	-71.75	264.10	-47.10	this study
130.00	M10	-70.74	262.89	-47.87	this study
132.53	M11	-70.26	262.30	-48.30	this study
134.75	M12	-69.67	260.65	-48.20	this study
138.30	M15n	-69.08	262.53	-50.85	this study
142.27	M17	-68.07	260.04	-50.64	this study
147.00	M20	-66.81	257.33	-50.42	this study

Table C-2 : **Antarctica - Africa**

Age [Ma]	Chron	Pole of rotation lat[°]	lon [°]	Angle [°]	Source
83.00	C34	-2.00	320.80	17.98	after Royer et al. (1988)
93.00	E	2.90	321.70	22.60	Livermore and Hunter (1996)
118.00	M0	-6.00	330.50	39.60	this study
122.25	M2	-8.07	331.89	42.20	this study
125.36	M4	-8.49	331.89	43.50	this study
130.00	M10	-8.31	331.21	44.86	this study
132.53	M11	-8.21	330.86	45.60	this study
134.75	M12	-8.16	330.57	46.25	this study
138.30	M15n	-8.13	330.14	47.30	this study
142.27	M17	-7.80	329.62	48.33	this study
147.00	M20	-7.33	329.02	49.53	this study
155.00	M24	-6.52	328.00	51.93	this study
167.20	JQZ	-5.20	326.34	56.22	this study

Table C-3 : **South America (northern part) - Africa** (central South Atlantic opening)

Age [Ma]	Chron	Pole of rotation		Angle [°]	Source
		lat[°]	lon [°]		
83.00	C34	61.59	325.85	33.50	Shaw and Cande (1990)
93.00	E	58.96	325.91	40.02	Livermore and Hunter (1996)
118.00	M0	51.78	325.26	52.51	Martin et al. (1982)
122.25	M2	50.07	326.00	53.66	this study
125.36	M4	48.99	326.36	54.37	Martin et al. (1982)
130.00	M10	50.12	327.21	55.20	after Nürnberg and Müller (1991)

Table C-4 : **Madagascar- Africa**

Age [Ma]	Chron	Pole of rotation		Angle [°]	Source
		lat[°]	lon [°]		
118.00	M0	90.00	0.00	0.00	Reeves and de Wit (2000); MAD fixed to AFR
136.00	M12	2.00	115.00	-6.80	after Reeves and de Wit (2000)
148.00	M20	2.00	115.00	-10.30	after Reeves and de Wit (2000)
155.00	M24	2.00	115.00	-12.50	intperpolated after Reeves and de Wit (2000)
167.20	JQZ	5.16	109.24	-16.12	intperpolated after Reeves and de Wit (2000)

Table C-5 : **Mozambique Ridge - Africa**

Age [Ma]	Chron	Pole of rotation		Angle [°]	Source
		lat[°]	lon [°]		
125.31	M3	90.00	0.00	0.00	Tikku et al. (2002), MOZR fixed to AFR
131.36	M10	-6.00	-50.00	1.45	Tikku et al. (2002)
134.75	M12	-8.01	310.24	2.48	this study
138.30	M15n	-8.87	310.35	3.56	this study
142.27	M17	-8.03	309.42	4.72	this study
147.00	M20	-6.49	-51.91	6.07	this study
167.20	JQZ	7.00	-77.00	10.50	extrapolated from Marks and Tikku (2001)

Table C-6 : **Paraná - South America**

Age [Ma]	Chron	Pole of rotation		Angle [°]	Source
		lat[°]	lon [°]		
125.36	M4	90.00	0.00	0.00	Paraná fixed to South America
130.00	M10	-10.22	288.54	1.70	this study
132.53	M11	-10.22	288.54	1.96	this study
134.75	M12	-6.82	289.69	2.19	this study
138.30	M15n	-2.69	291.07	2.58	this study
142.27	M17	-8.20	291.01	3.00	this study

Table C-7 : **Salado - Paraná**

Age [Ma]	Chron	Pole of rotation		Angle [°]	Source
		lat[°]	lon [°]		
125.36	M4	90.00	0.00	0.00	Salado fixed to Paraná
130.00	M10	20.92	321.51	0.30	this study
132.53	M11	20.92	321.51	1.00	this study
134.75	M12	19.64	315.41	1.10	this study
138.30	M15n	33.77	310.52	1.40	this study
142.27	M17	5.02	301.02	1.92	this study
147.00	M20	5.02	301.02	1.92	this study
167.20	JQZ	-16.22	294.79	4.17	this study

Table C-8 : **Colorado - Salado**

Age [Ma]	Chron	Pole of rotation		Angle [°]	Source
		lat[°]	lon [°]		
132.53	M11	90.00	0.00	0.00	Colorado fixed to Salado
134.75	M12	-10.12	310.15	0.83	this study
138.30	M15n	74.48	62.85	1.77	this study
142.27	M17	16.97	307.36	1.45	this study
147.00	M20	16.97	307.36	1.45	this study
167.20	JQZ	-20.26	294.89	3.98	this study

Table C-9 : **Patagonia - Colorado**

Age [Ma]	Chron	Pole of rotation lat[°]	lon [°]	Angle [°]	Source
138.30	M15n	90.00	0.00	0.00	Patagonia fixed to Colorado
142.27	M17	50.62	87.37	2.89	this study
147.00	M20	56.87	34.01	2.85	this study
167.20	JQZ	25.16	347.96	3.08	this study

Table C-10 : **Falkland Plateau - Patagonia**

Age [Ma]	Chron	Pole of rotation lat[°]	lon [°]	Angle [°]	Source
125.36	M4	90.00	0.00	0.00	Falkland Plateau fixed to Patagonia
130.00	M10	-4.29	153.20	0.71	this study
132.53	M11	11.63	147.21	1.09	this study
134.75	M12	8.76	133.31	1.39	this study

Table C-11 : **Falkland Islands - Patagonia**

Age [Ma]	Chron	Pole of rotation lat[°]	lon [°]	Angle [°]	Source
125.36	M4	90.00	0.00	0.00	Falkland Islands fixed to Patagonia
130.00	M10	39.20	-30.00	-1.00	this study
167.20	JQZ	39.20	-45.00	-2.00	this study

Table C-12 : **Antarctic Peninsula - Antarctica**

Age [Ma]	Chron	Pole of rotation lat[°]	lon [°]	Angle [°]	Source
147.00	M20	90.00	0.00	0.00	Antarctic Peninsula fixed to Antarctica
167.20	JQZ	-73.74	310.51	23.13	this study